Polarizing a Stored Proton Beam by Spin-Flip?

Inaugural-Dissertation
zur
Erlangung des Doktorgrades
der Mathematisch-Naturwissenschaftlichen Fakultät
der Universität zu Köln

vorgelegt von
Dieter Gerd Christian Oellers
aus Jülich

Jülich, 2010

für Silvia

Abstract

The present thesis discusses the extraction of the electron-proton spin-flip cross-section. The experimental setup, the data analysis and the results are pictured in detail.

The proton is described by a QCD-based parton model. In *leading twist* three functions are needed. The quark distribution, the helicity distribution and the transversity distribution. While the first two are well-known, the transversity distribution is largely unknown. A self-sufficient measurement of the transversity is possible in double polarized proton-antiproton scattering. This rises the need of a polarized antiproton beam.

So far spin filtering is the only tested method to produce a polarized proton beam, which may be capable to hold also for antiprotons. *In-situ* polarization build-up of a stored beam either by selective removal or by spin-flip of a spin-$\frac{1}{2}$ beam is mathematically described. A high spin-flip cross-section would create an effective method to produce a polarized antiproton beam by polarized positrons. Prompted by conflicting calculations, a measurement of the spin-flip cross-section in low-energy electron-proton scattering was carried out.

This experiment uses the electron beam of the electron cooler at COSY as an electron target. The depolarization of the stored proton beam is detected. An overview of the experiment is followed by detailed descriptions of the cycle setup, of the electron target and the ANKE silicon tracking telescopes acting as a beam polarimeter. Elastic proton-deuteron scattering is the anaylzing reaction. The event selection is depicted and the beam polarization is calculated. Upper limits of the two electron-proton spin-flip cross-sections $\sigma_\parallel$ and $\sigma_\perp$ are deduced using the likelihood method.

Zusammenfassung

In der vorliegenden Arbeit wird die Messung und Bestimmung des Elektron-Proton Spinflip Wirkungsquerschnittes vorgestellt. Der experimentelle Aufbau, die Datenanalyse und die Ergebnisse sind im Detail beschrieben.

Das Proton wird durch ein QCD-basiertes Parton Modell beschrieben. In *leading twist* werden drei Funktionen benötigt. Es sind die Quarkdistribution, die Helizitätsdistribution und die Transversitydistribution. Obwohl die ersten beiden präzise gemessen sind, ist über die Transversitydistribution wenig bekannt. Eine von weiteren Messungen unabhängige Bestimmung der Transversitydistribution ist in doppelpolarisierten Proton-Antiproton Streuexperimenten möglich. Daraus erwächst der Wunsch, einen polarisierten Antiprotonenstrahl zu erzeugen.

Bislang ist Spinfiltern die einzige an Protonen getestete Methode, die auch für Antiproton funktionieren kann. *In-situ* Polarisationsaufbau eines gespeicherten Spin-$\frac{1}{2}$ Strahls durch selektiven Verlust und selektiven Spinflip wird beschrieben. Ein großer Spinflip Wirkungsquerschnitt eröffnet eine effektive Methode, einen Antiprotonenstrahl zu polarisieren. Angetrieben durch sich wiedersprechende Berechnungen, wurde eine Messung des Spinflip Wirkungsquerschnittes in niederenergetischer Eletron-Proton Streuung durchgeführt.

In diesem Experiment wird der Elektronenstrahl des Elektronenkühlers an COSY als freies Elektronentarget benutzt und die Depolarisation des gespeicherten Protonen Strahls gemessen. Einem Überblick über dem Experiment folgt eine detaillierte Beschreibung der COSY Beschleunigerzyklen, des Elektronen Targets und der Silizium Tracking Teleskope, die als Polarimeter betrieben wurden. Elastische Proton-Deuteron Streuung ist als Analysereaktion verwendet. Die Eventselektion ist beschrieben und die Polarisation des Protonenstrahls wurde berechnet. Obere Grenzen der zwei Elektron-Proton Spinflip Wirkungsquerschnitte $\sigma_{\parallel}$ und $\sigma_{\perp}$ konnten mittels der Likelihood-Methode bestimmt werden.

Contents

List of Figures

Chapter 1

PAX Physics Motivation

In a QCD[1] parton model the proton is described in *leading twist* by three functions: The quark distribution $q(x, Q^2)$, the helicity distribution $\Delta q(x, Q^2)$ and the transversity distribution $\delta q(x, Q^2)$. While the first two of them are well known the transversity distribution is largely unknown. A direct measurement of the transversity is possible in double polarized proton-antiproton scattering.

Sec. 1.1 describes, how scattering experiments lead to the present proton structure description. In sec. 1.2 the ways to measure the transversity distribution are described and it is shown, why a polarized antiproton beam is the favorable tool for this measurement. The PAX[2] collaboration is aiming to perform this experiment and in sec. 1.3 one additional physics case for a polarized antiproton beam is briefly introduced.

1.1 Proton Structure

1.1.1 Scattering Experiments

Scattering experiments have proved to be a powerful tool to probe the inner structure of the proton. Along with the enormous increase of the kinetic energy of particles in an accelerator, more information about the proton structure becomes accessible. In a descriptive picture the spacial resolution of an experiment is in the order of the de Broglie wavelength $\lambda = h/p$ of the testing probe. Here h is the Planck constant and p the momentum of the probe. Scattering experiments led to the discovery of the proton in 1919 by Rutherford and 45 years later it became clear, that this particle possesses a substructure. Inclusive Deep Inelastic Scattering experiments showed that the structure functions of the proton were to a large extent independent on the squared momentum transfer Q^2. Bjørken and Feynman interpreted this scaling behavior as an evidence of point-like sub-proton particles [Bjo69a, Bjo69b, Fey69]. Later these objects were identified with the quarks, predicted by Gell-Mann and Zweig [Gel64, Zwe64].

---

[1]**Q**uantum **C**hromo **D**ynamics
[2]**P**olarized **A**ntiproton e**X**periments

Ernest Rutherford and Ernest Marsden studied α-particle scattering by light elements using a cloud chamber between 1910 and 1914. Additionally to the short range tracks from the α in hydrogen gas, they occasionally observed tracks up to 4 times longer. They speculated that these long range particles were hydrogen nuclei knocked out by the α and called them H-particles. After the first world war, Rutherford continued this work with different gases including boron, fluorine, sodium, aluminum, phosphor and nitrogen [Ruth19]. From all these gases the H-particles showed up and Rutherford concluded that the H-particles, today known as protons, must be constituents of all elements. This conclusion from 1919 may be considered the discovery of a new elementary particle, the proton.

Elastic Scattering   Elastic scattering of electrons off protons is a simple process to extract information on the properties of the proton. Elastic scattering is assumed to be dominated by the single-photon exchange mechanism (fig. 1.1). Here k and P are the
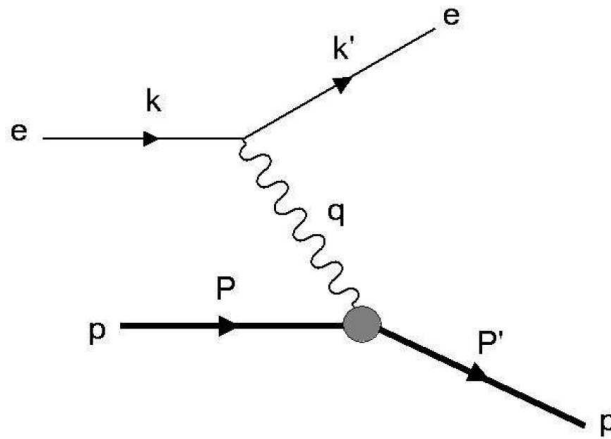
Figure 1.1: Feynman graph of elastic electron proton scattering.

four-momenta of the incoming electron and proton, respectively, and k' and P' those of the scattered particles. The four-momentum q of the exchanged virtual photon is given by the difference between the initial and final state four-momenta:

$$q = k - k' = P' - P \tag{1.1}$$

Averaging over all mutual spin states and using the Feynman rules for QED[3], the squared amplitude of this process can be written in the following compact form:

$$\langle |A|^2 \rangle = \frac{\alpha^2}{q^4} L_{\mu\nu} K_{\mu\nu}, \tag{1.2}$$

where $\alpha = \frac{e^2}{4\pi}$ is the electromagnetic coupling and $L_{\mu\nu}$ and $K_{\mu\nu}$ are the leptonic and the hadronic tensors describing the interaction at the leptonic and hadronic vertices. While

---

[3]**Q**uantum **E**lectro **D**ynamics

$L_{\mu\nu}$ can be derived from QED, $K_{\mu\nu}$ is parametrized in terms of the so-called elastic proton from factors K_1 and K_2.

These form factors, which only depend on q^2, can be redefined in terms of the electric (G_E) and magnetic (G_M) proton form factors, which are associated with the charge distribution and current distribution of the proton. The elastic electron-proton scattering cross section can be written in the form:

$$\frac{d\sigma}{d\Omega} = \frac{4\alpha^2 E^2 \cos^2(\Theta/2)}{q^4[1 + (2E/M)\sin^2(\Theta/2)]} \left(\frac{G_E^2 + \tau G_M^2}{1 + \tau} + 2\tau G_M^2 \tan^2(\Theta/2) \right), \qquad (1.3)$$

known as the Rosenbluth formula [Ros50], where Θ is the scattering angle and $\tau = -q^4/(4M^2)$, with the proton mass M.

The measurement of the cross section and the subsequent extraction of G_E through the Rosenbluth formula allowed to extract the root-mean-square charge radius r_E of the proton [Mur74]:

$$r_E^2 = \int d^3x \, r^2 \rho(r) = -6 \left. \frac{dG_E(q^2)}{dq^2} \right|_{q^2=0} = (0.81 \pm 0.04) \times 10^{-13} cm^2. \qquad (1.4)$$

The same radius of about 0.8 fm was also obtained for the current distribution. The complete world data on $\frac{\mu G_E}{G_M}$ extracted using the Rosenbluth separation is a momentum transfer Q^2 independent value (fig 1.2). New measurements of the formfactors via polarization observables, however, indicate that this is not the case.

Deep Inelastic Scattering With increasing beam energy higher momentum transfers are possible and in the descriptive picture this leads to a higher spacial resolution. The proton breaks up and forms a hadronic final state X. This is called deep inelastic scattering (DIS).

$$l + p \to l' + X \qquad (1.5)$$

In the cross section of DIS a spin independent part and a spin dependent cross section can be separated. Averaging over all spins in the initial state of the scattering process and summing over the spins in the final state leads to the spin-independent part of the cross-section:

$$\frac{d^2\sigma^{unpol}}{dE'd\Omega} = \left(\frac{d^2\sigma}{dE'd\Omega} \right)_{Mott} \cdot \left[\frac{2}{M} F_1(x, Q^2) \tan^2(\Theta/2) + \frac{1}{\nu} F_2(x, Q^2) \right], \qquad (1.6)$$

where

$$\left(\frac{d^2\sigma}{dE'd\Omega} \right)_{Mott} = \frac{4\alpha^2 E'^2}{Q^4} \cos^2(\Theta/2), \qquad (1.7)$$

with $E(E')$ is the energy of the incoming (outgoing) electron, M is the proton mass, $Q^2 = -q^2$ is the negative squared 4-momentum transfer, $\nu = \frac{P \cdot q}{M} \overset{lab}{=} E - E'$ is the energy transfer from the incoming electron to the proton in laboratory frame, $x = \frac{Q^2}{2P \cdot q} \overset{lab}{=} \frac{Q^2}{2M\nu}$.
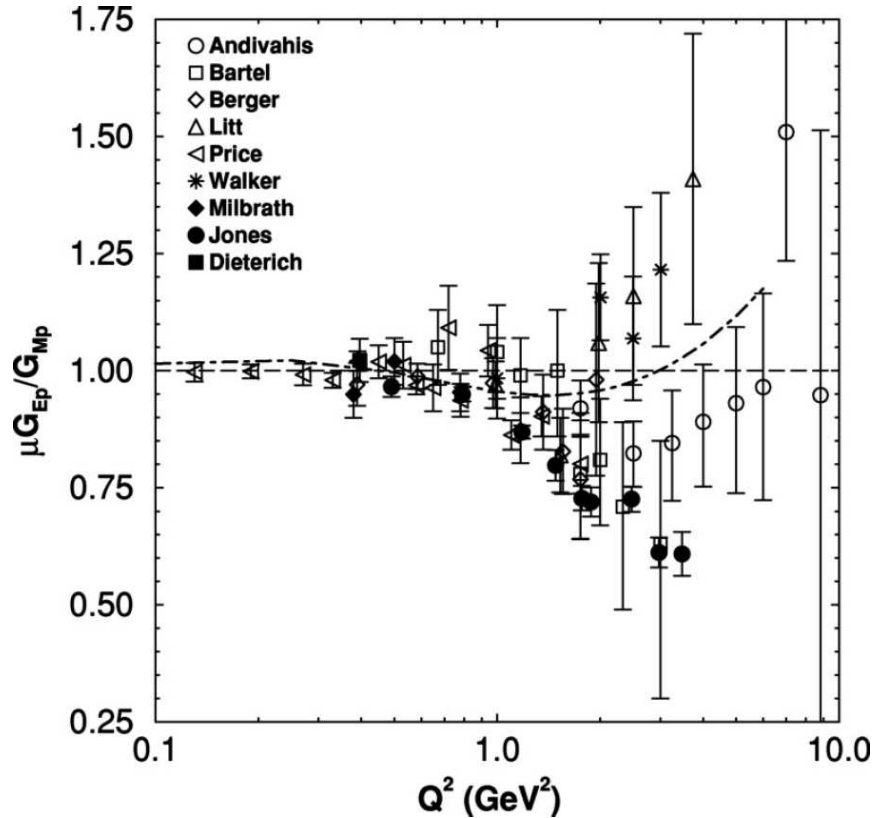
Figure 1.2: World data for $r = \mu G_E/G_M$; open symbols indicate results of the Rosenbluth separation [Mil98, Die01, Jon00] and give a constant ratio. [Gay01]

$\left(\frac{d^2\sigma}{dE'd\Omega}\right)_{Mott}$ is the Mott cross section, which describes the elastic scattering of a relativistic spin-$\frac{1}{2}$ particle off a spin-0 point-like particle. The second term of eqn. 1.6 contains the unpolarized structure functions, represents the deviation of the observed DIS cross section from the Mott cross section. This deviation is due to the composite nature of the proton. A selection of the world data for the structure function F_2 as a function of Q^2 for different x is given in fig. 1.4.

The cross section for the case when both colliding electron and proton are longitudinally polarized has a spin-dependent and a spin-independent part. In order to isolate the spin-dependent part of the cross section the difference of the cross sections obtained with two opposite target spin states is measured. The spin-independent part cancels and one obtains the bare spin-dependent cross section:

$$\frac{d^3\sigma^{\overrightarrow{\Leftarrow}}}{dxdy} - \frac{d^3\sigma^{\overrightarrow{\Rightarrow}}}{dxdy} = \frac{r\alpha^2}{sxy}\left[\left(2 - y - \frac{\gamma^2y^2}{2}\right)g_1(x,Q^2) - \gamma^2yg_2(x,Q^2)\right], \qquad (1.8)$$

where $\rightarrow$ indicates the spin orientation of the incoming electron and $\Leftarrow, \Rightarrow$ the two different spin states of the target proton. $\gamma = \frac{2Mx}{Q}$, $s = (k+P)^2$ is the center-of-mass energy squared
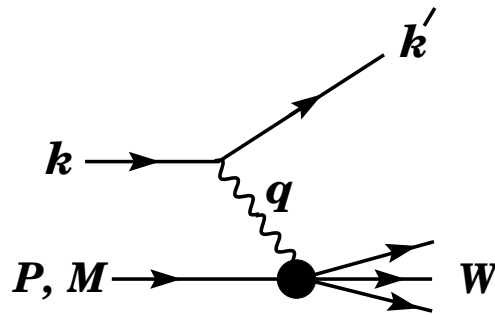
Figure 1.3: Feynman graph of deep inelastic electron proton scattering. The exchanged particle is a $\gamma, W^{\pm}$ or Z. [pdg08]

and $y = \frac{P \cdot q}{p \cdot k} \overset{\text{lab}}{=} \frac{\nu}{E}$ is the fractional energy of the virtual photon.

In fig. 1.5 the g_1 structure function for protons is given as a function of the Bjørken x.

The Bjørken scaling Fig. 1.4 shows that the unpolarized structure function F_2 is approximately Q^2-independent in the large momentum transfer region:

$$F_2(x, Q^2) \approx F_2(x) \qquad (Q^2 \gg M^2). \tag{1.9}$$

According to the Callan-Gross relation [Cal69] the two spin-independent structure functions F_1 and F_2 are related to each other by

$$F_2(x) = 2x F_1(x) \tag{1.10}$$

and thus F_1 shows the same approximate Q^2-independence.

This phenomenon, predicted by the Quark Parton Model (QPM), is known as *Bjørken scaling* or *scale invariance* because in the so-called Bjørken limit

$$\lim_{Bj} = \begin{cases} Q^2 \to \infty \\ \nu \to \infty \\ x \text{ fixed} \end{cases}, \tag{1.11}$$

the structure functions are left unchanged by a scale transformation, i.e. by a transformation in which Q^2 and ν are multiplied by an arbitrary scale factor k, so that x remains unchanged. A Q^2-independence of the structure functions would imply that the electron "sees" the same proton structure no matter how big the spatial resolution is. The observed scaling behavior could be successfully accounted for by considering scattering off point-like constituents within the proton. This was historically the first dynamical evidence of the quarks, whose existence had been previously inferred on the basis of static quantities, like the masses and quantum numbers of the hadrons.

Still the structure functions show a deviation from the described scale invariance. With increasing momentum transfer the structure functions show a strong increase for low x and
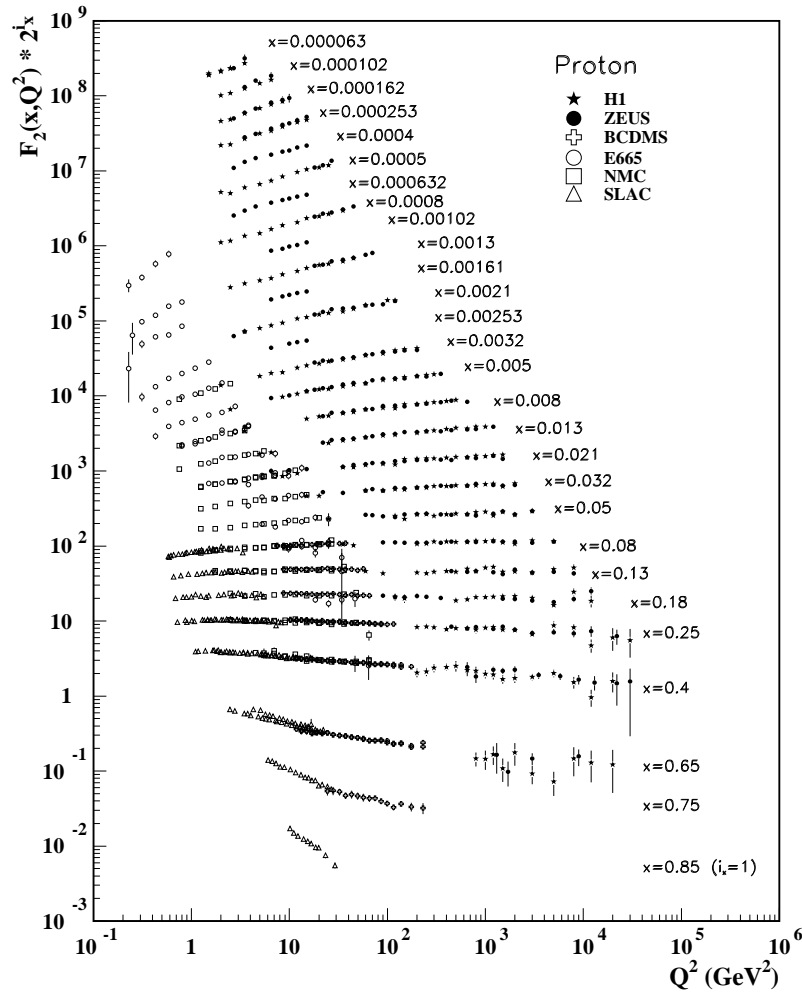
Figure 1.4: The proton structure function F_2^p measured in electromagnetic scattering of positrons on protons (collider experiments ZEUS and H1), in the kinematic domain of the HERA data, for x > 0.00006, and for electrons (SLAC) and muons (BCDMS, E665, NMC) on a fixed target [pdg08].

a decrease for high x. This is an evidence of the dynamical structure of the proton (virtual sea quarks and gluons) and represented one of the earliest triumphs of QCD. The sea quark contribution increases with increasing momentum transfer and each quark carries less fractional momentum.
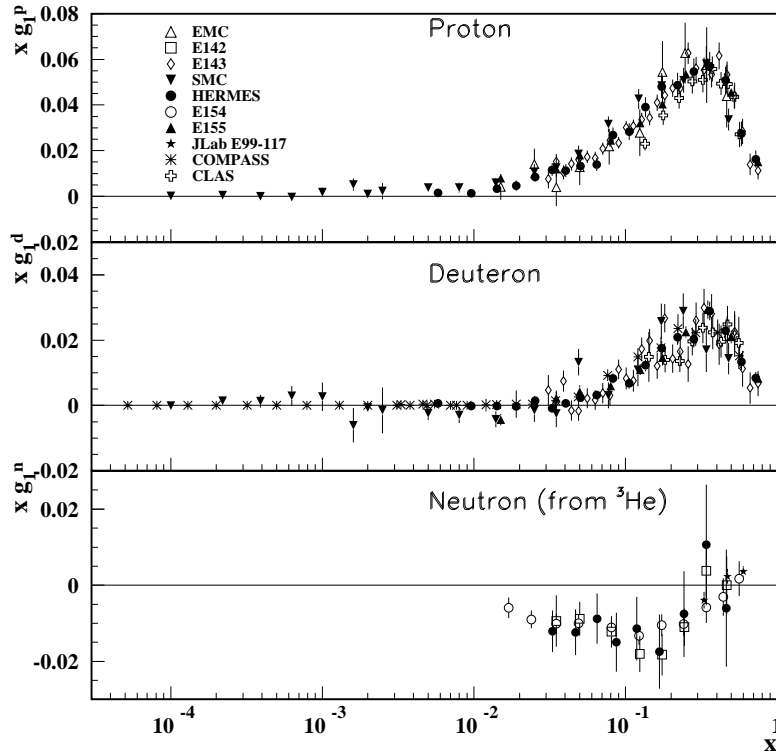
Figure 1.5: World results for the spin-dependent structure function $g_1(x)$ of the proton measured in deep-inelastic scattering of polarized electrons/protons [pdg08].

1.1.2 Quark Parton Model

With the knowledge from scattering experiments the Quark Parton Model was developed. Three valence quarks are dressed with a cloud of gluons and virtual quark-antiquark pairs. In this framework the proton is described in *leading twist* by three functions. Namely the quark distribution $q(x, Q^2)$, the helicity distribution $\Delta q(x, Q^2)$ and the transversity distribution $\delta q(x, Q^2)$. It is:

$$q_f(x) = q_f^{\vec{\Rightarrow}}(x) + q_f^{\vec{\Leftarrow}}(x), \qquad (1.12)$$

$$\Delta q_f(x) = q_f^{\vec{\Rightarrow}}(x) - q_f^{\vec{\Leftarrow}}(x) \text{ and} \qquad (1.13)$$

$$\delta q(x) = q^{\Uparrow\uparrow}(x) - q^{\Uparrow\downarrow}(x), \qquad (1.14)$$

where $q_f^{\vec{\Rightarrow}}(x)$ and $q_f^{\vec{\Leftarrow}}(x)$ are the probability densities to find a quark of flavor f with momentum fraction x and spin parallel or anti-parallel to the proton spin. $q^{\Uparrow\uparrow}(x)$ and $q^{\Uparrow\downarrow}(x)$ are the probability densities to find any quark with their spin aligned or anti-aligned to the spin of a transversly polarized proton.

The first two of these parton distributions are correlated to the structure functions, which can be measured in DIS. It is:

$$F_1(x) = \frac{1}{2} \sum_f e_f^2 q_f(x), \tag{1.15}$$

$$g_1(x) = \frac{1}{2} \sum_f e_f^2 \Delta q_f(x). \tag{1.16}$$

As a result the first two are well known, while the transversity is only little-known. A direct measurement could be realized by Drell-Yan production $q\,\overline{q} \rightarrow (\gamma,\, Z) \rightarrow l^+ l^-$ in double polarized $p\overline{p}$ collisions.

1.2   Transversity Distribution

The third *leading twist* parton distribution function of the quark parton model ($\delta q(x)$), the so-called *transversity*, has been only recently measured. Due to its chiral-odd nature it is not accessible in DIS, where helicity is conserved. Ralston and Soper considered the double transverse spin asymmetry in the Drell-Yan process. Three references with more detail are given: [Art90, Jaf92, Cor92]. The Drell-Yan process is a lepton pair production in the collision of two hadrons, and the asymmetry A_{TT} is to be measured in the cross-section:

$$A_{TT} = \frac{\sigma(p^{\uparrow}p^{\uparrow} \rightarrow l\bar{l}X) - \sigma(p^{\uparrow}p^{\downarrow} \rightarrow l\bar{l}X)}{\sigma(p^{\uparrow}p^{\uparrow} \rightarrow l\bar{l}X) + \sigma(p^{\uparrow}p^{\downarrow} \rightarrow l\bar{l}X)} \propto \sum_q e_q^2\, \delta q^q(x_1)\, \delta q^{\overline{q}}(x_2) \tag{1.17}$$

RHIC at BNL is at present the only place that could take data on this asymmetry. But
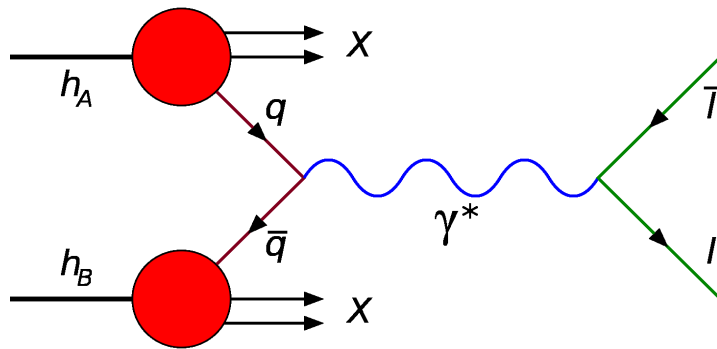
Figure 1.6: Feynman graph of the Drell-Yan process. Additionally to the indicated virtual photon, a Z-boson could be exchanged. [Wiki]

for the RHIC energy range A_{TT} is expected to be small. An upper bound in the percent level is predicted [Mar99] and the required accuracy is not achievable.

An alternative way to measure the transversity is to measure the product of transversity with another chiral odd function. The first suggestion was made by Collins [Col93] who introduced a chiral odd fragmentation function. In semi-inclusive DIS experiments the product of the Collins function with the transversity distribution becomes accessible by detecting an azimuthal asymmetry of the produced hadron. A π^+ e.g. contains information about the spin of a struck u quark from the proton, as the π^+ contains the valence quarks u and $\overline{d}$. The HERMES experiment at DESY was the first to measure a nonzero, Collins asymmetry[Air05, Die]. These measurements allow for an extraction of transversity once the Collins function is known. A measurement of the Collins function was carried out at KEK using BELLE data [Sei06, Sei]. A first extraction of $\delta q(x)$, based on a global fit of the data from HERMES, COMPASS [Age07] and BELLE, has been reported by [Ans07] (see fig. 1.7).
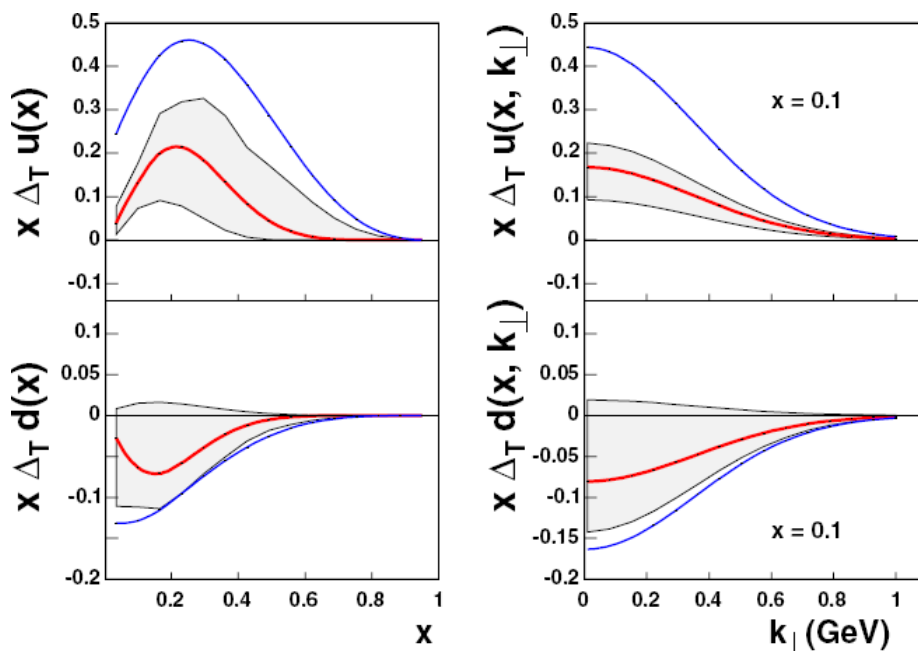
Figure 1.7: First extraction of transversity by Anselmino et al. [Ans07]. Left: $x\delta q(x)$ for u and d quarks, the red curves are the best fits, the blue curves the Soffer bounds. Right: $k_T - dependence$ using a Gaussian Ansatz.

The BELLE and semi-inclusive DIS data are obtained at different scales: $Q^2 = 110\,\text{GeV}^2$ and $\langle Q^2 \rangle = 2.4\,\text{GeV}^2$. The extraction of the transversity uses the projection of the measured BELLE Collins asymmetries to HERMES energies. In this extraction, the theoretical uncertainties are rather big.

So a self-sufficient measurement of the transversity function is of great importance. The golden channel to perform a self-sufficient measurement is the lepton pair production in

double polarized Drell-Yan collisions of proton-antiproton.

$$\overline{p}^{\uparrow} p^{\uparrow} \rightarrow l\bar{l}X \tag{1.18}$$

It is ideally suited for δq extraction, because $\delta q^{\overline{q}/\overline{p}} = \delta q^{q/p}$, leading to:

$$A_{TT} = \frac{\sigma(\overline{p}^{\uparrow} p^{\uparrow} \rightarrow l\bar{l}X) - \sigma(\overline{p}^{\uparrow} p^{\downarrow} \rightarrow l\bar{l}X)}{\sigma(\overline{p}^{\uparrow} p^{\uparrow} \rightarrow l\bar{l}X) + \sigma(\overline{p}^{\uparrow} p^{\downarrow} \rightarrow l\bar{l}X)} = a_{TT} \frac{\sum_q e_q^2 \, \delta q(x_1, Q^2) \, \delta q(x_2, Q^2)}{\sum_q e_q^2 \, q(x_1, Q^2) \, q(x_2, Q^2)}. \tag{1.19}$$

Here only $q = u$ and $q = d$ contribute, and a_{TT} is the double spin asymmetry of the QED elementary process: $q + \overline{q} \rightarrow l\bar{l}$.

As only sea quarks contribute it is $\tau = x_1 \cdot x_2 = Q^2/s \approx 0.2 - 0.3$ and in this kinematic region is accessible with a fixed target mode with $s = 30\,\mathrm{GeV}^2$. In this region A_{TT}/a_{TT} is expected to be as large as 30 %. The **P**olarized **A**ntiproton EX**p**eriments - Collaboration is aiming to perform this direct measurement of the transversity. The (x_1, x_2) kinematic regions covered by the PAX measurements, both in the fixed target and collider mode[4] are shown in fig. 1.8, left side. The plot on the right side shows the expected values of the asymmetry A_{TT} as a function of the Feynman $x_F = x_1 - x_2$ for $Q^2 = 16\,\mathrm{GeV}^2$ and different values for the squared total energy s.
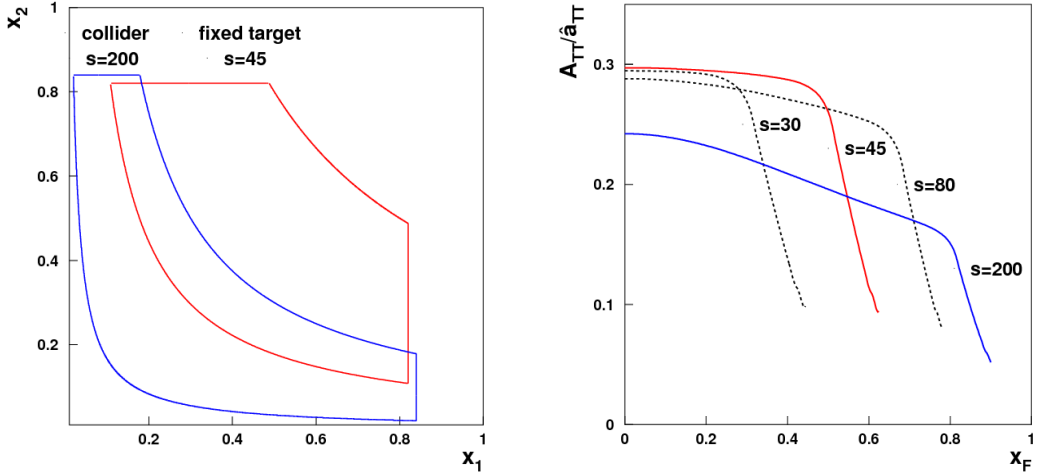
Figure 1.8: Left: The kinematic region covered by the δq measurement at PAX. In the asymmetric collider scenario (blue) antiprotons of 3.5 GeV/c impinge on protons of 15 GeV/c at c.m. energies of $s \approx 200\,\mathrm{GeV}^2$ and $Q^2 > 4\,\mathrm{GeV}^2$. The fixed target case (red) represents antiprotons of 22 GeV/c colliding with a fixed polarized target ($\sqrt{s} \approx \sqrt{45}\,\mathrm{GeV}$). Right: The expected asymmetry as a function of Feynman x_F for different values of s, but fixed $Q = 16\,\mathrm{GeV}^2$. [PAX05]

---

[4]The PAX-collaboration proposed experiments at FAIR. A dedicated Antiproton Polarizer Ring (APR) would fill a Cooler Syncrotron Ring (CSR), where the polarized antiprotons are stored with a momentum up to 3.5 GeV/c. Here, fixed target experiments can be carried out. By adding two beam lines collisions with the polarized protons from the High Energy Storage Ring (HESR) are possible.

1.3 Electromagnetic Form Factors of the Proton

Recently, data with a new method, called recoil polarization technique, to extract the ratio G_E/G_M were published [Jon00, Gay01, Gay02]. A longitudinally polarized electron beam transfers its polarization to the recoil proton in electron-proton elastic scattering. Assuming one-photon exchange it is [Akh74]

$$\frac{G_E}{G_M} \propto -\frac{P_t}{P_l} \tan \frac{\theta_e}{2}, \tag{1.20}$$

with P_t (P_l) the component of the recoil proton polarization perpendicular to (parallel to) the proton momentum in the scattering plane. These data were taken in the space-like regime and the measured Q^2-dependence was unexpected (fig. 1.9).
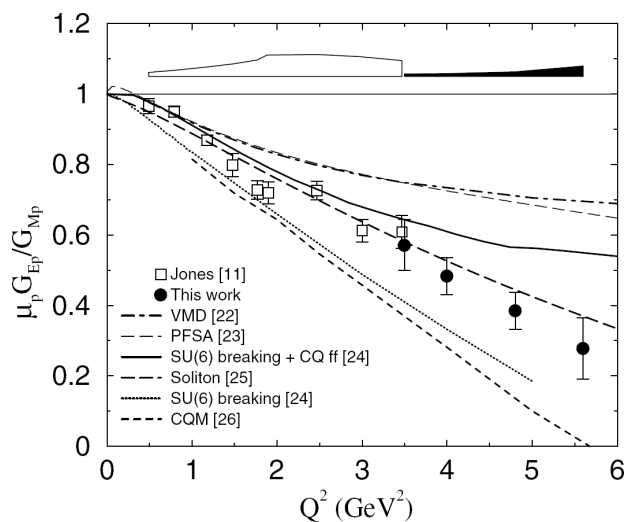
Figure 1.9: The ratio G_E/G_M extracted using the recoil polarization method.

The two proton from factors G_E and G_M measured in the space-like and time-like domains are connected to each other by dispersion relations. As a result, it follows:

$$\lim_{Q^2 \to \infty} G_E, G_M \text{ (space} - \text{like)} = \lim_{Q^2 \to -\infty} G_E, G_M \text{ (time} - \text{like)}. \tag{1.21}$$

Experiments in the time-like regime are not sensitive to G_E. In fact, the extractions assuming $G_E = G_M$ and $G_E = 0$ show no difference in the time-like regime. There are two ways to clarify the role of G_E in the time-like regime. Either perform experiments with high angular resolution, or to use double polarized proton-antiproton annihilation: $\vec{p}\,\vec{\bar{p}} \to e^+ e^-$.

With this short introduction the high impact of polarized anti-proton beams on new physics should have become obvious. The next chapter will deal with various ideas, how a polarized anti-proton beam might be produced.

Chapter 2

Methods to Produce Polarized Antiproton Beams

As described in sec. 1, polarized antiproton beams with high intensity constitute a missing tool to several untouched physics problems. Up to now, a convenient method to produce polarized antiproton beams is not available. Workshops in Bodega Bay 1985 [Bod85] and in Daresbury 2007 [Bar07] were carried out on the topic of polarized antiproton beams. Several ideas towards polarized antiproton beams from these workshops are discussed in the following section. Spin filtering is emphasized as this thesis clarifies the mechanism of this method.

Polarization

The dipol-magnets of a cyclotron fix the stable polarization axis parallel or antiparallel to the magnetic fields. A spin-$\frac{1}{2}$ particle, like a proton or antiproton, two spin states "up" $\uparrow$ and "down" $\downarrow$ are possible. $N_\uparrow$ ($N_\downarrow$) is the number of particles with spin states "up" ("down") and the beam polarization P is then defined by:

$$P = \frac{N_\uparrow - N_\downarrow}{N_\uparrow + N_\downarrow}. \tag{2.1}$$

2.1 Spin Filtering

Csonka proposed in 1968 spin-selective attenuation of the particles circulating in a storage ring as a method to polarize a stored beam [Cso68]. Particles stored in the ring pass through a polarized target and a fraction of the beam is lost by nuclear scattering in the target. Since the strong interaction cross section is different for beam and target spins parallel ($\uparrow\uparrow$) and anti-parallel ($\uparrow\downarrow$), one spin direction of the circulating beam is depleted more than the other. As a result the circulating beam becomes increasingly polarized. This method has been referred to as "spin filtering". A sketch of the principle is given by fig. 2.1.

In principle three different scattering reactions can contribute to the effect. They are
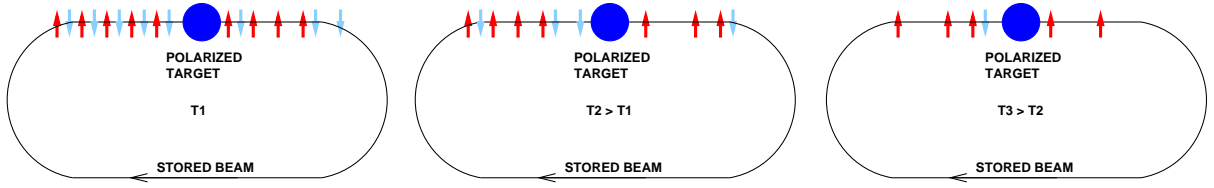
Figure 2.1: The three sketches clarifies the method of spin filtering. The arrows indicate particles with spin up (down). After some time of filtering (T2 and T3) the beam current is reduced and the beam is polarized.

- scattering at the hydrogen nucleus within the acceptance angle,

- scattering at the hydrogen nucleus out off the acceptance angle and

- scattering at the target electrons within the acceptance angle.

Scattering at the target electrons out off the ring acceptance does not occur as the maximum scattering angle is always smaller than the machine acceptance due to the smallness of the mass ratio $\frac{m_e}{m_p}$.

In order to calculate the polarization buildup during filtering, the more general polarization evolution of a stored beam is given for a beam consisting of spin-$\frac{1}{2}$ particles. The following cross sections are used:

- $\sigma_R = \frac{1}{2} \left(\sigma_{\uparrow\uparrow}^R + \sigma_{\uparrow\downarrow}^R \right)$ and $\Delta\sigma_R = \frac{1}{2} \left(\sigma_{\uparrow\downarrow}^R - \sigma_{\uparrow\uparrow}^R \right)$,

- $\sigma_S = \frac{1}{2} \left(\sigma_{\uparrow\uparrow}^{SF} + \sigma_{\uparrow\downarrow}^{SF} \right)$ and $\Delta\sigma_S = \frac{1}{2} \left(\sigma_{\uparrow\downarrow}^{SF} - \sigma_{\uparrow\uparrow}^{SF} \right)$.

The index R stands for scattering outside of the ring acceptance, while SF indicates scattering with spin flip inside of the ring acceptance. The arrows indicate the spin direction of the two particles involved in the scattering event. After a short calculation (app. A) one concludes:

$$\left. \frac{dP}{dt} \right|_{P=0} = f_{rev} \cdot d_t \cdot Q \left[2 \cdot \Delta\sigma_S + \Delta\sigma_R \right]. \tag{2.2}$$

It describes the polarization evolution dP/dt of an initially unpolarized beam and is valid for small beam polarizations. The target density is given by d_t and the target polarization is Q. The "polarizing cross section", σ_{pol} is defined as the sum of the two terms in the bracket:

$$\sigma_{\mathrm{pol}} = 2 \cdot \Delta\sigma_S + \Delta\sigma_R \tag{2.3}$$

The polarization evolution for an unpolarized target ($Q = 0$) is given by:

$$\frac{dP}{dt} = -2 f_{rev} \cdot d_t \sigma_S P \tag{2.4}$$

It shows that the "depolarizing cross section" is directly proportional to the spin flip cross section σ_S. Since the sum of two positive values is always bigger than the norm of their difference, it is $\sigma_S \geq \Delta\sigma_S$ and it follows from eqn. 2.2 and 2.4 that

if a polarized target is capable of polarizing an unpolarized beam by spin flip, an unpolarized target will depolarize an already polarized beam.

2.1.1 Concept

Assuming, that spin-flip is negligible, only the loss cross section σ_T has an impact on the beam polarization. σ_T is the integral of the strong interaction cross section in the range $\Theta_{\text{acc}} < \Theta < \pi$. It can be expressed as a sum of an spin-independent and spin-dependent part:

$$\sigma_T = \sigma_0 \pm \sigma_1 \cdot Q, \tag{2.5}$$

where the positive and negative sign applies to the fraction of the beam whose spin is parallel or anti-parallel to the spin of the target. σ_0 is the spin-independent part of the cross section, σ_1 the spin-dependent part of the cross section and Q the target polarization. The time constant τ_1, which characterizes the rate of the polarization buildup, is

$$\tau_1 = \frac{1}{\sigma_1 \, Q \, d_t \, f_{\text{rev}}}, \tag{2.6}$$

where d_t is the target density and f_{rev} is the revolution frequency of the beam. In order to build up significant polarization, the beam has to pass through the target for times t of the order τ_1.

The goal while performing a spin-filtering is to reach as small as possible filter times and highest possible beam polarization. In order to reach the first goal especially the target density d_t has to be maximized and the experiment has to be carried out at an energy, where the spin-dependent cross section σ_1 is maximized. Figure 2.2 shows the dependence of σ_1 of the beam kinetic energy T and it is obvious, that beam energies below $T = 100\,\text{MeV}$ are essential. Conflicting with the aim to maximize the spin-dependent cross section σ_1 is the goal to minimize the Coulomb beam losses, which increase with $\frac{1}{T^2}$.

Additionally, a high density polarized target at an internal target point of a synchrotron is necessary. Polarized gaseous targets can be produced using an atomic beam source followed by a magnetic system in Stern-Gerlach configuration. However, the target thickness provided by such a jet is only about $2 \cdot 10^{11} \, \overrightarrow{H}$ atoms/cm^2. To increase the target density the polarized $\overrightarrow{H}$ beam is filled in a windowless T-shaped storage cell [Hae85], through which the circulating beam passes. In this way the target thickness can be increased and some 10^{13}/cm^2 up to 10^{14}/cm^2 becomes available.

By using phase space cooling of the stored beam, beam losses due to multiple scattering can be minimized and thus the beam lifetime maximized. Additionally the ring vacuum should be optimized in order to minimize the scattering with the unpolarized residual gas.

Finally, a detection system is needed to measure both beam and target polarization independently.
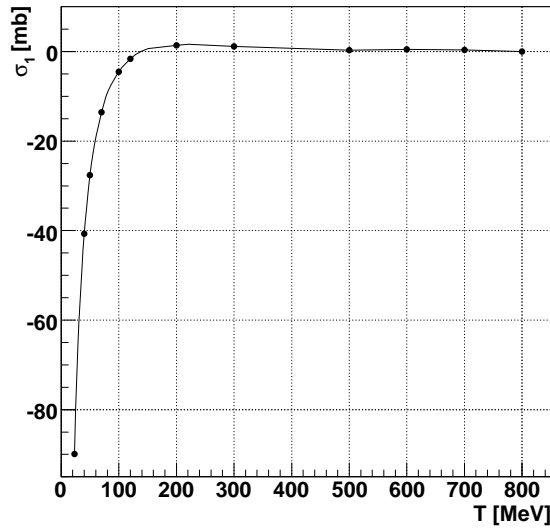
Figure 2.2: Spin dependent beam loss cross section by strong interaction σ_1 *vs* beam kinetic energy T. The strong increase at energies below $100\,\text{MeV}$ makes beam energies $T < 100\,\text{MeV}$ essential.

2.1.2   The FILTEX Experiment

In 1992 at the Test Storage Ring (TSR) in Heidelberg [Kra89] this method to polarize a stored beam was tested with a proton beam. The experimental setup of the spin filter experiment is displayed in fig. 2.3. A beam lifetime of roughly $30\,\text{minutes}$ of an electron cooled beam was achieved with the beam energy of $T = 23\,\text{MeV}$ used during filtering. Low-β quadrupoles have been installed in the target section in order to increase the acceptance angle.

The target polarization was deduced by measurements at the beginning and the end of the experiments. A $27\,\text{MeV}$ beam of α particles was stored in the ring and the target polarization measured from the left-right asymmetry of recoil protons at $\Theta_{\text{lab}} = 21°$. The magnitude of the target polarization was found to be $Q = 0.83 \pm 0.03$.

After the filtering time between 30 and 90 minutes, the beam polarization was measured by making use of the large spin correlation coefficient $A_{xx} = -0.93$ in proton-proton elastic scattering. For this purpose the direction of the $5\,\text{G}$ guide field, which determines the direction of the target polarization (up or down), was reversed periodically. The pp elastic count rates were measured with scintillation counter telescopes [Dür92] located at $\Theta_{\text{lab}} = 33°$ above and below the plane of the storage ring.

The result is shown in fig. 2.4. The rate of polarization buildup of

$$\frac{\Delta P_B}{\Delta t} = \pm(1.24 \pm 0.06) \times 10^{-2}\,\text{h}^{-1},$$

implies $\tau_1 = 80\,\text{h}$.
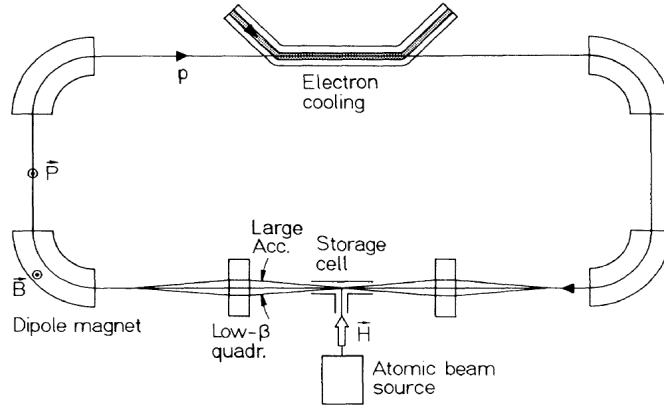
Figure 2.3: Principle of the spin filter experiment with storage ring, low-β section, storage cell, and electron cooler [RAT93].
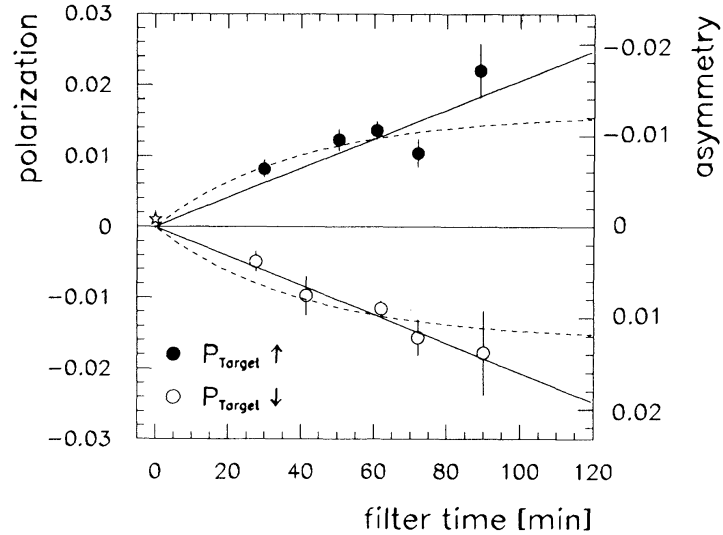
Figure 2.4: Asymmetry (right-hand scale) and polarization (left-hand scale) measured after filtering the beam in the storage ring for different times t. The solid lines are based on an assumed rate of polarization buildup of $1.24 \times 10^{-2} h^{-1}$, which corresponds to $\tau_1 = 80\,\mathrm{h}$. [RAT93]

2.1.3 Interpretation

In the FILTEX experiment, the target density was $d_t = (5.3 \pm 0.3) \cdot 10^{13} \mathrm{cm}^2$ and the target polarization was $Q = 0.795 \pm 0.024$. Together with the measured polarization buildup of $1.24 \times 10^{-2} h^{-1}$ it leads to:

$$\sigma_{\mathrm{pol}} = (76 \pm 6)\,\mathrm{mb}. [\mathrm{Rat05,\ Rat94}] \tag{2.7}$$

First theoretical calculations, using the TSR acceptance angle $\Theta_{\mathrm{acc}} = (4.4 \pm 0.)$ mrad leads to

$$\sigma_{\mathrm{pol,theo}} = (86 \pm 2)\,\mathrm{mb}. \tag{2.8}$$

The fact that experiment and theory disagree by two standard deviations has been the original motivation to investigate the role of spin flip.

Evaluating the spin-transfer cross section at small angles between 10 and 100 MeV, sizable effects were predicted [Mey94]. The spin-transfer cross section, as defined e.g. in [Bys78], refers to producing a spin-up beam particle (rather than a spin down) when an unpolarized beam interacts with a polarized target. A decade later, Milstein and co-workers [Mil05] showed that the spin-flip cross section (the cross section that the spin of a beam particle is reversed), which is different from, and much smaller than the spin-transfer cross section and is in fact negligible for the proton energy used in the FILTEX experiment.

More recently, Arenhövel [Are07] predicted that the spin-flip cross section in electron-proton scattering at low energy (a few eV in the center-of-mass system) is very large because of the mutual attraction of the two oppositely charged particles. This effect could be used to produce a polarized antiproton beam as shown in sec. 2.3.

2.2   Other Ideas

As polarized proton beams with high intensity are available, the question arises, why the procedures used for protons are not applicable for antiprotons. There are three prominent ways for protons. Polarization of a scattered beam was used for the first polarized proton experiments. A secondary polarized antiproton beam from Λ^--decay with low intensity has been produced. This and other ideas have been proposed at the Bodega Bay workshop [Bod85] and are described in this section.

Atomic Beam Source

Atomic beam sources are widely used to produce polarized proton beams [Nas05]. Laser based sources for polarized protons [Zel85] are also available. Here the atomic beam source will be discussed in some detail (left fig. 2.5). Molecular hydrogen from a bottle is dissociated by a radio frequency field in a plasma. From here a beam of thermic hydrogen atoms is leaving a nozzle at low temperature ($T < 100$ K). This beam is formed by a skimmer and collimator. In a sextupole magnet setup one of the two electron spin states is focused, while the other is deflected. In a magnetic field the degeneracy of the hyperfine states with F = 1 is removed (right fig. 2.5). Transitions are induced by a radio frequency between different hyperfine states and a second sextupole magnet setup separates one single state. The additional radio frequency unit can be used to allow all different spin states. After ionization this polarized hydrogen beam can be used to fill a cyclotron, or the polarized atom beam could fill a storage cell in order to provide high target densities. An overview of the polarized gas targets can be found in [Ste03]. With a thermic anti-hydrogen beam it should work identically. Up to day the maximum number of thermic anti-hydrogen atoms
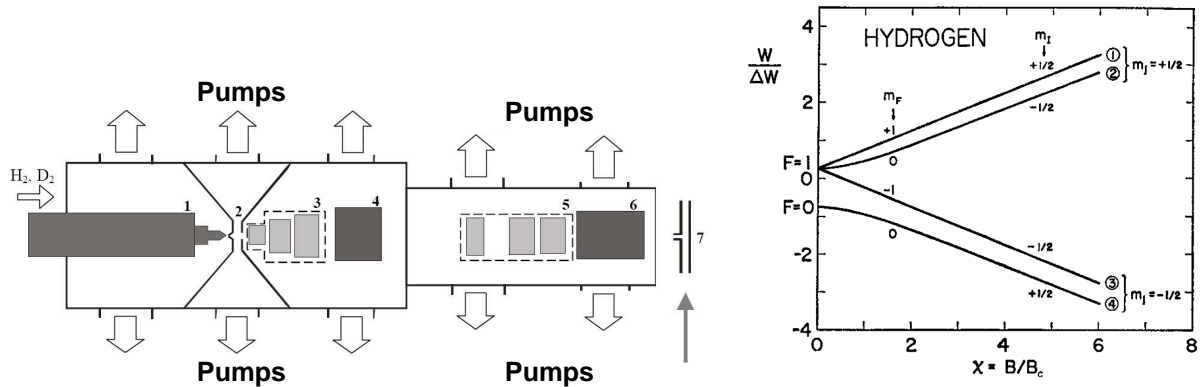
Figure 2.5: Left: Sketch of an ABS. 1 is the dissociator, 2 the nozzle with skimmer and collimator, 3 + 5 the sextupoles, 4 + 6 are radio-frequency transition units and 7 is the storage cell. Right: Energy of the four hyperfine states of hydrogen as a function of $\chi = B/B_C$ with $B_C = 50.7$ mT [Hae67].

is many orders too low ($\approx 10^3 - 10^4$/trial anti-hydrogen are produced by the ATRAP-collaboration [Gab08].), in order to feed an atomic beam source.

Dynamic Nuclear Polarization in Flight

Dynamic nuclear polarization in flight is a technique where the polarization of electrons is transferred to nearby protons [Bod85]. For antiprotons the idea is to inject unpolarized antiprotons into an interaction region with a high longitudinal magnetic field along with polarized electrons moving at the same velocity. Microwave radiation could then induce hyperfine interactions with spin transfer. With electron densities in the order of $10^{10}/\text{cm}^3$, the polarization transfer rate to each antiproton would be about 10^{-5}/s, which is too long.

Stern-Gerlach Separation

Roughly twenty-three years ago at the workshop in Bodega Bay, it was suggested that Stern-Gerlach forces could be used to separate ensembles of antiprotons with opposite spin states into sub-ensembles with non-zero polarization [Bod85]. Meanwhile, two basic approaches are under consideration. One uses the transverse Stern-Gerlach forces, while the other uses longitudinal ones. The first one leads to a spacial separation and the second one to different beam energies. Even though this idea is rather old, no detailed simulation has shown its effectiveness. An experimental test of this method would need a large effort. Up to now, a feasibility study has not been carried out, thus this effort seems to be not justified.

For a more detailed summary about this way to produce a stored polarized antiproton beam see [Bar07].

Antiprotons from Hyperon Decay

Polarized protons (antiprotons) from the decay of polarized hyperons (anti-hyperons) produced on one side of the collisions between $400\,\text{GeV}$ protons at FermiLab and a fixed target; and then focusing them into a $200\,\text{GeV}$ polarized proton (antiproton) beam. The achieved polarization was in the order of $50\,\%$. Though, the intensity and large phase space make it difficult to store and accelerate these polarized antiprotons in a storage ring. The expected intensities are too low for experiments in high energy accelerator experiments.

Stochastic Techniques

Similar to stochastic cooling, where the positions of the beam particles are measured and corrected at a second point of the accelerator, a stochastic enhancement of the beam polarization was thought of. By a polarization sensitive detector an appropriate signal could be transmitted to another part of the ring and kick out one polarization state more than the other. The difficulty is the small size of the electrical signals available from the protons magnetic moment in comparison to the signals due to the protons charge. Simon Van der Meer showed that the signal to background ratio is in the order of 10^{-42} and thus this idea is not feasible.

Polarization Buildup by Synchrotron Radiation

In synchrotrons charged particles are forced in a closed orbit by magnetic fields. In the bending regions synchrotron radiation is emitted. The radiation power P is given by [Lee04]

$$p = \frac{e^2 c \gamma^4 \beta^4}{3\pi \epsilon_0 \rho^2}, \tag{2.9}$$

with the electron charge e, speed of light c, bending radius ρ, permittivity of free space ϵ_0 and the relativistic variables γ and β. The amount of spin-flip radiation is extremely small compared to the ordinary (non-flip) synchrotron radiation. The ratio of the powers radiated is:

$$\frac{P_{\text{(spin-flip)}}}{P_{\text{(non-flip)}}} = 3 \left(\frac{\hbar \gamma^2}{mc\rho} \right)^2 \left(1 \pm \frac{35\sqrt{3}}{64} \right), \tag{2.10}$$

where the choice of sign depends on the initial spin state of the particle. For an electron cyclotron with a bending radius $\rho \approx 13\,\text{m}$ and $\gamma < 10^4$ the ratio 2.10 is of the order of 10^{-11}. So for electrons the polarization build-up time is rather long and for HERA in the order of $40\,\text{minutes}$ [Dur95]. The used formulas are to be changed for protons. In a naive description the characteristic polarization build-up time is [Jac76]:

$$\tau_{\text{naive}} = \left[\frac{2}{3} \left| \frac{g}{2} \right|^5 \frac{e\hbar \gamma^5}{m^2 c^2 \rho^3} \right]^{-1} \tag{2.11}$$

For the LHC with $\rho = 2803.95\,\text{m}$ and $\gamma = 7461$ at the highest beam energy, the polarization build-up time is $\tau_{\text{naive}}^{\text{LHC}} \approx 7.8 \cdot 10^{23}\,\text{s}$ or $2 \cdot 10^{16}$ years. Thus it is obvious, that this method is not suitable for antiproton polarization build-up.

Channeling through a Bent Crystal

Channeling is a well established phenomenon which is studied since decades and has many applications at low and high energy physics [Lin65, Lin64, Gem74, Bir97]. Channeling in a bent crystal can be considered as scattering on both sides of a channel. If the crystal and its channels are bent, then scattering to the outer side of the channel must prevail (in strength and/or in number) on the scatterings on the inner side of the channel. If the single scattering process has an analyzing power, then the channeled beam will gain polarization in a bent crystal. The final beam polarization P is calculated by [Ukh08]:

$$p = \frac{(1 + A_y)^N - (1 - A_y)^N}{(1 + A_y)^N + (1 - A_y)^N}, \tag{2.12}$$

with N scatterings with the analyzing power of A_y in each of them. With an analyzing power of $A_y = 10^{-4}$ and $N = 5000$ scatterings the overall polarization P would be $P = 46\,\%$. Assuming an analyzing power A_y of 0.5% leads to a beam polarization of more than $50\,\%$ after extraction of the primary beam from a bent crystal [Ukh08]. So even without knowledge of the actual analyzing powers involved in channeling - they could be 0, it might be worth to test the channeled beam for polarization. Such an investigation could be carried out at the extraction beam of COSY.

2.3   Buildup by Polarized Positrons

Meanwhile, the Mainz group proposed a new method for polarizing antiprotons by electron proton spin-flip [Wal07] based on a QED calculation of the triple spin cross-sections by H. Arenhövel [Are07]. They claim that with a polarized positron beam moving parallel to the antiprotons at relative velocity of $v/c \approx 0.002$ the cross-section for spin-flip is as large as about $2 \cdot 10^{13}\,\mathrm{b}$. The predicted electron proton spin-flip cross-section as a function of the proton kinetic energy in the electron rest frame is plotted in fig. 2.6.

With this high cross-section a significant effect is experimentally reachable even with a low target density, which can be achieved by the free electrons in an electron cooler. Making use of the statement from sec. 2.1 (page 15) all necessary technical tools to measure the electron proton spin-flip cross-section are available at COSY.
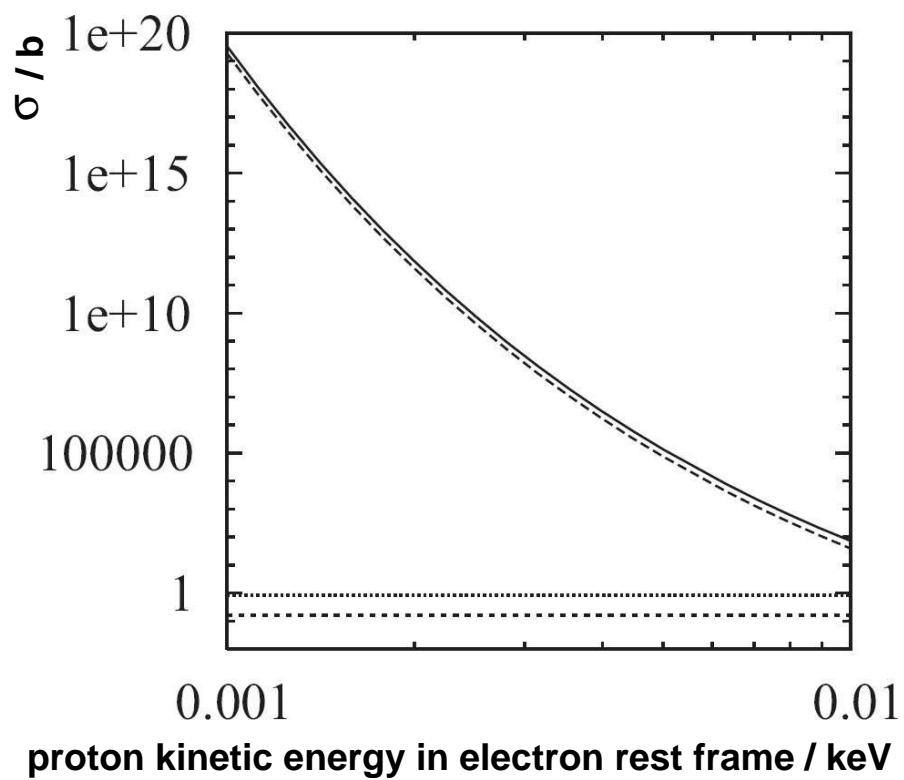
Figure 2.6: The electron proton spin-flip cross-section as a function of the kinetic proton energy in the electron rest frame. A prediction from Arenhövel [Wal07] is shown. Special emphasize is on the strong energy dependence, which makes very low relative velocities necessary.

Chapter 3

Do Electrons Affect the Beam Polarization?

The experiment is driven by the idea of polarizing a stored, initially unpolarized anti-proton beam by interacting with a polarized positron beam [Wal07]. The positron antiproton spin transfer cross section was calculated to be about $2 \cdot 10^{13}$ barn at a relative velocity of $v/c \approx 0.002$. The authors claimed that with a polarized positron beam with a polarization of 0.70 and a flux density of approximately $1.5 \cdot 10^{10}/(\text{mm}^2\text{s})$ from a radioactive ^{11}C dc-source, a beam of about 10^{10} antiprotons can be polarized within one hour to a polarization of about 0.18.

The goal of the experiment is to measure the electron proton spin transfer at relative energies in the order of a few $10^{-3}\,c$. In sec. 3.1 the synchrotron COSY is described. Section 3.2 explains the measurement principle before the individual parts of the experimental setup are described in detail: The cycle structure is depicted in sec. 3.3. In sec. 3.4 it is described, how the electron cooler is used as an electron target while still providing a well-cooled beam. Finally, in sec. 3.5 the deuterium cluster target is described and in sec. 3.6 the detection system is depicted.

3.1   COSY

At the Research Center Jülich (FZJ) the Institute for Nuclear Physics (IKP) operates the **CO**oler **SY**nchrotron (COSY). At this accelerator (fig. 3.1) the experiment on the electron-proton spin-transfer cross-section was carried out. It provides proton or deuteron beams in the momentum range between 300 (550 for deuterons) and 3700 MeV/c. COSY is a ring with 183 m circumference including two 40 m straight sections inserted at opposite locations. A 100 keV electron cooler and stochastic cooling above 1.5 GeV/c provide phase space cooling of the stored beam. Unpolarized and polarized beams are provided for external or internal experiments. Transversely polarized proton beams are available with intensities up to $1 \cdot 10^{10}$ particles with a typical polarization of 70 %. For deuterons an intensity of $3 \cdot 10^{10}$ with vector and tensor polarization of more than 70 % and 50 % were
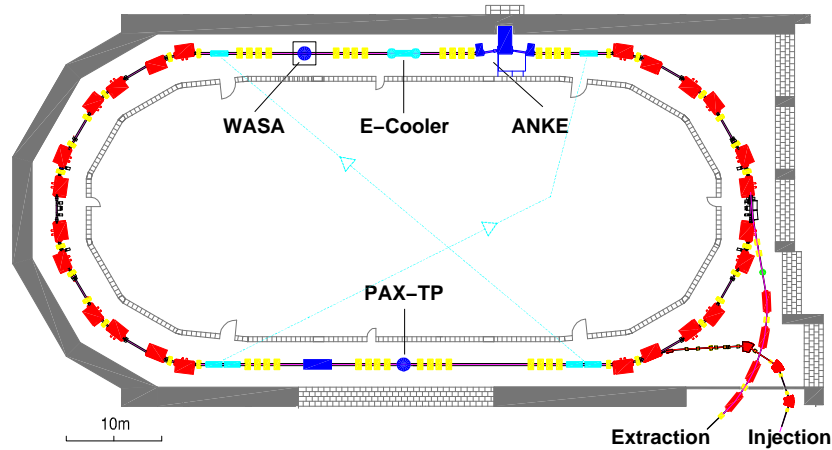
Figure 3.1: Floor plan of COSY including the injection and extraction beam line. The internal experiments ANKE and WASA are as well indicated as the positions of the electron cooler and the target place for future spin filtering studies planned by the PAX collaboration.

achieved, respectively.

The three main experimental setups at COSY are the **T**ime **O**f **F**light (TOF) spectrometer, the **W**ide **A**ngle **S**hower **A**pparatus (WASA) detector, a large-acceptance detector for charged and neutral particles and the **A**pparatus for studies of **N**ucleon and **K**aon **E**jectiles the ANKE magnetic spectrometer. Additionally, a new target point for the **P**olarized **A**ntiproton E**X**periments (PAX) is under construction. Here a new low beta-section is build to increase the acceptance angle at this target point. As a first step, additional quadrupole magnets were installed and commissioned. The first collisions are planned for summer 2010.

3.2 Measurement Principle

An ideal test of the prediction [Wal07] would use polarized electrons to polarize an initially unpolarized proton beam. As at the Jülich synchrotron, COSY [COS], no polarized electrons are available, a depolarization experiment was carried out. As shown in sec. 2.1 and in more detail in app.A the depolarization cross section is an upper limit for the polarization build-up: If a polarized target is capable of polarizing an unpolarized beam by spin flip, an unpolarized target will depolarize an already polarized beam.

A polarized proton beam was stored in COSY. Electrons in the electron-cooler have been used as a free electron target. This electrons induce the depolarization of the beam and the beam polarization was measured using proton-deuteron elastic scattering events at a deuteron-cluster target installed at the ANKE [ANK] target position (fig 3.2).
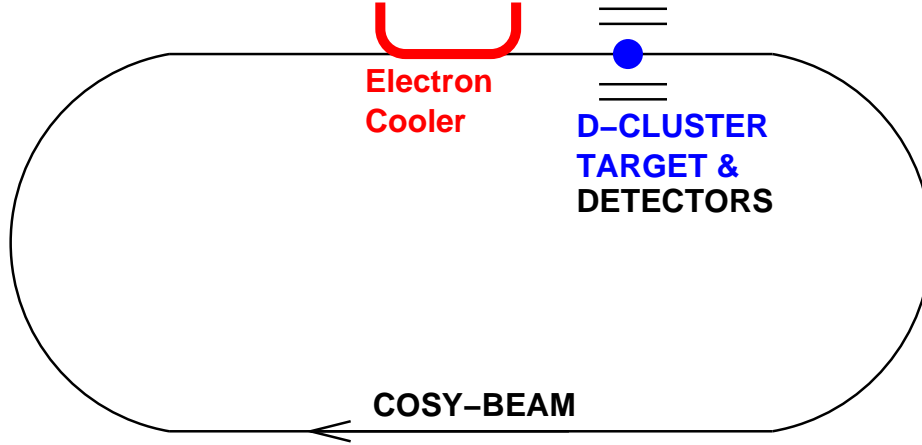
Figure 3.2: Schematic of the experiment indicating the main installations used in the experiment: The synchrotron COSY, the electron cooler, the deuteron cluster target and the detection setup.

3.3   COSY Setup

A polarized beam was injected into COSY and accelerated to a kinetic energy of $T_p = (49.3 \pm 0.1)$ MeV. This beam energy was chosen to fulfill several tasks.

- The investigated effect is predicted to be large at relative velocities in the order of $10^{-3} c$ (fig. 3.3). Therefore the experiment is carried out with a beam energy, where the electron cooler can provide a free electron target.

- In order to measure the beam polarization, analyzing powers of the used polarimeter reaction are to be known. For $T_p = 49.3$ MeV the analyzing powers are precisely known from [Kin77].

From eqn. 3.2 the characteristic polarization lifetime τ_{pol} is calculated by

$$\tau_{pol} = \frac{1}{2 \cdot \sigma \cdot d_t \cdot f_{rev}}. \tag{3.1}$$

Taking the predicted depolarization cross section from Arenhövel [Are07] and the electron target density ($d_t = 2 \cdot 10^7/\text{cm}^2$ at 1 keV beam kinetic energy see fig. 3.6) the expected beam polarization lifetime is calculated. The result is given in fig. 3.3 and shows a strong energy dependence. This makes a kinetic energy in the order of a few keV in the electron rest frame necessary. To give two numbers, the predicted beam polarization lifetime increases from roughly 3 ms for a proton kinetic energy of 1 keV to ≈ 10000 s at 6 keV.
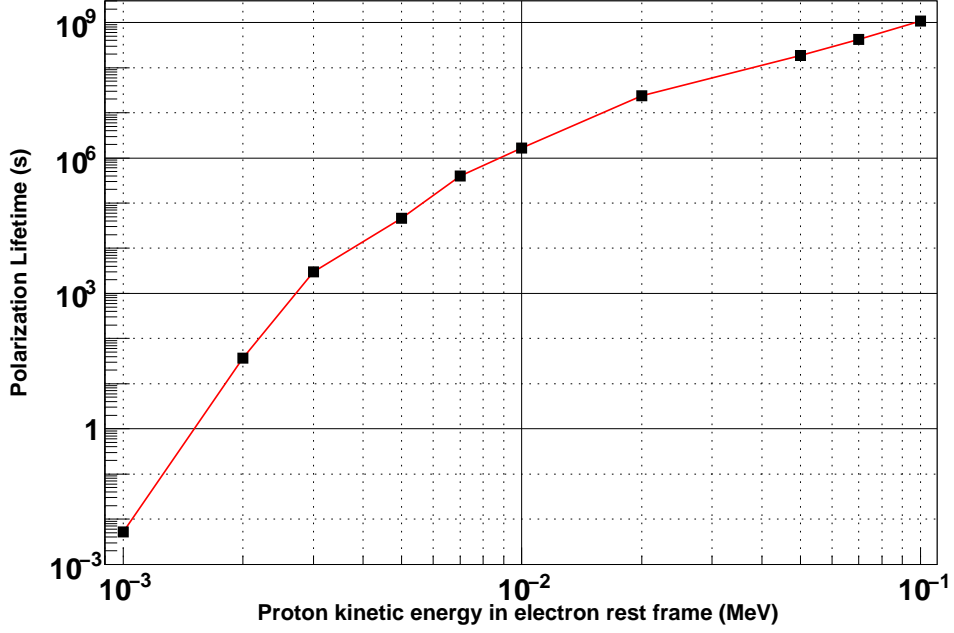
Figure 3.3: Polarization lifetime calculated using the predicted spin-flip cross section from [Wal07] as a function of the proton kinetic energy in the electron rest frame.

The spin flip cross section σ_S leads to a depolarization rate given by (sec. A)

$$\frac{P_B}{dt} = -2 \cdot f_{\mathrm{rev}} \; d_t \; \sigma_S P_B \tag{3.2}$$

where the beam polarization is P_B, the target density d_t and the beam revolution frequency f_{rev}. Using this equation, the spin-flip cross section is extracted by:

$$\sigma_S = \frac{-\ln\left(\frac{P_E}{P_0}\right)}{2 \cdot d_t \cdot \Delta t \cdot f_{\mathrm{rev}}}, \tag{3.3}$$

where the two polarizations P_E and P_0 are measured after two different times of depolarization. This time difference is Δt. After measuring the beam polarization, the beam intensity is too low for a second measurement later in the same cycle. Instead two cycles where the electron target was switched on for two different times have been used. In fact, in the "0"-cycle there were 0 s with electron target and in the "E"-cycle there were 245 s with electron target. These two cycles are designed to be as similar as possible. The only difference between the cycles is the electron target. During one it is switched on, while during the second one no electron target is utilized. It is assumed that the beam polarization at the time of injection into COSY is identical and effects from the synchrotron will develop the beam polarization in the same way during the two different cycles. The fraction of the beam polarizations at the end of the two different cycles provides a measurement of the

depolarization rate due to the electrons. If done ideally, all systematic effects on the beam polarization occur in the same way in both cycles and cancel. A table showing the time sequence is given in tab. 3.1 and a schematic of the cycle setup is shown in fig. 3.4.

Time in cycle /s	"E"-CYCLE	"0"-CYCLE
0	Injection and Acceleration	
1	Switching Electron Cooling on	
$14 + 2n \cdot 5$	Switch to Target Mode	Switch Electron Beam off
$14 + (2n+1) \cdot 5$	Switching to Cooling Mode	
505	Electron Cooling and Deuterium Cluster Target	
	Measure Beam Polarization	
1060	Beam is Dumped	

Table 3.1: This table shows the timing settings of the two different cycles. n is an integer from 0 to 48, indicating the total 49 sub-cycles.
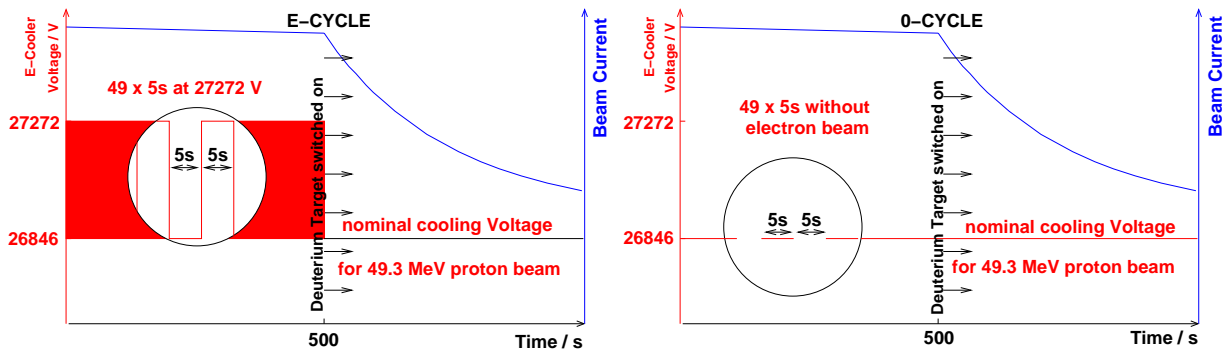
Figure 3.4: The first 505 s after injection a cooled proton beam was cycling in COSY. During this time the electron cooler was switched each 5 s. While in "E"-cycle the electron cooler was switched between cooling and target, in "0"-cycle it alternated between cooling and no electrons. In the second 550 s long part the deuterium cluster target was switched on and the polarizations of the now steadily electron cooled beam was measured with proton-deuteron elastic scattering events.

Both "E"-cycle and "0"-cycle consist of two parts. In the first part - 505 s long - the beam is injected and accelerated to $T_p = 49.3$ MeV before it is electron-cooled for 14 s. This is followed by 49 sub-cycles, which are different for the two cycles. Each sub-cycle is composed of 5 s where the electron velocity is changed for cycle "E" or the electron current switched off for cycle "0" and additional 5 s with nominal cooling for both cycles.

The second part - 555 s long - is identical in both cycles. During this time the electron-cooled polarized proton beam hits the ANKE deuterium cluster target. The proton-deuteron elastic scattering events are detected. The data analysis of this data will determine the beam polarization.

3.4   Electron Target

Co-moving electrons in the electron cooler are used to produce an electron target at relative velocities in the order of $0.002\,c$ or $2\,keV$ proton kinetic energy in the electron rest frame. Non-moving electrons could not be used for the target as the beam lifetime is dominated by Coulomb scattering and drops with $1/T_B^2$, where T_B is the kinetic energy of the beam.

A detailed description on how the electron target is realized and what effects have to be taken into account is given.

3.4.1   Electron Cooler Voltage

The electrons of the electron cooler beam are produced by a cathode. Successive there is a grid at positive potential. By switching on (off) the potential of this grid the electron beam is switched on (off). An additional plate at high potential allows to accelerate the electron beam. By changing this voltage, it is possible to adjust the electron velocity. As the electron space charge partially screens this acceleration voltage, the acceleration voltage has to be increased depending on the electron beam current. With an electron current of $170\,mA$, a voltage of $26849\,V$ is needed to reach a velocity of $0.312\,c$ corresponding to the cooling mode for a proton beam at $49.3\,MeV$ kinetic energy. In target mode the
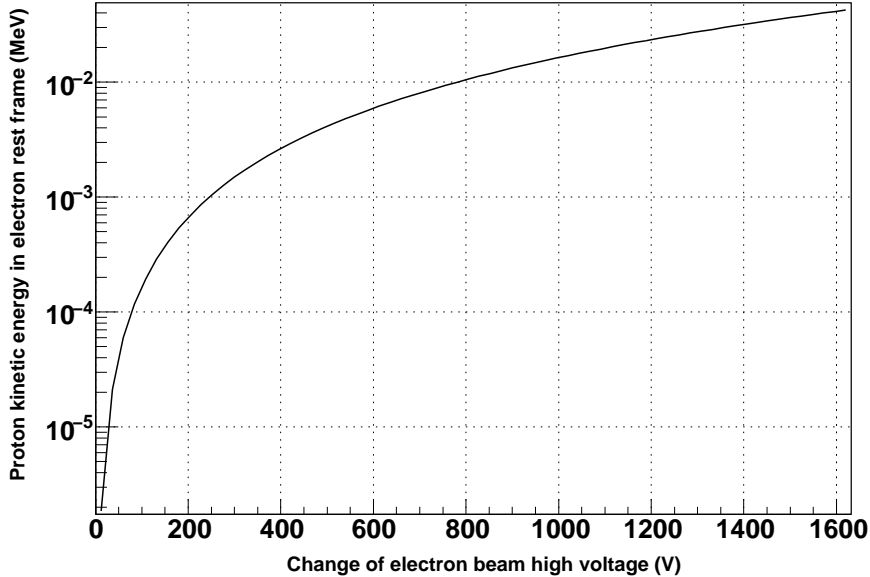
Figure 3.5: Proton kinetic energy in the electron rest frame *vs* shift of acceleration voltage for electrons.

acceleration voltage has to be changed. This change has to be known as a function of the

proton kinetic energy in the electron rest frame. It is:

$$\beta_p^e = \frac{\sqrt{T_p^{e2} + 2T_p^e m}}{T_p^e + m}, \quad \beta_e = \frac{\beta_{\text{Beam}} - \beta_p^e}{1 - \beta_{\text{Beam}} \cdot \beta_p^e} \quad \text{and} \quad \beta_{\text{rel}} = \beta_{\text{Beam}} - \beta_e, \tag{3.4}$$

with T_p^e and β_p^e the kinetic energy and the velocity of the proton in the electron rest frame and the proton velocity $v_{\text{Beam}} = \beta_{\text{beam}} \cdot c$, the electron velocity β_e and the relative velocity of electrons and protons β_{rel}. If nothing is indicated, all values are given in the laboratory frame.

The voltage jump is then

$$\Delta V = m_e \cdot (\gamma_e - 1) - V_0, \tag{3.5}$$

with the relativistic γ_e of the electrons in the laboratory frame and the nominal cooler voltage of $V_0 = 26849\,\text{V}$. The shift due to the space charge does cancel, as it does not depend on the electron energy.

As a result a short table showing the voltage jump for some energies is given (tab. 3.2).

T_p^e/keV	β_e^p	β_{rel}	β_e	V_{det}/V	$\frac{\Delta V}{V}$
0.001	0.00145999	0.00131726	0.313325	27095.3	245.6
0.0015	0.00178812	0.00161315	0.313621	27150.6	300.9
0.002	0.00206474	0.00186254	0.31387	27197.3	347.6
0.0025	0.00230845	0.00208222	0.31409	27238.5	388.8
0.003	0.00252878	0.0022808	0.314288	27275.8	426.1
0.005	0.00326463	0.00294382	0.314951	27400.4	550.7

Table 3.2: For several proton kinetic energies T_p^e in the electron rest frame, the values for the electron velocity in the proton frame β_e^p, the relative electron proton velocity in the laboratory frame β_{rel}, the electron velocity in the laboratory frame β_e, the electron acceleration voltage V_{det} and the change of the electron acceleration voltage compared to nominal cooling mode ΔV are given.

3.4.2 Target Density

Only the fraction of electrons, which are traversed by the protons, contribute to the target density. This effect leads to a dependency of the target density on the relative velocity between electrons and protons. The target density is calculated for the following parameters of the electron cooler:

- The electron current of $I_e = 170\,\text{mA}$, which was used during the experiment.

- The geometrical length of electron cooler is $L_{\text{Cooler}} = 2\,\text{m}$. In this region, the electrons move parallel to the proton beam.

- The cross section of the electron beam is $A_{\text{Cooler}} = 5\,\text{cm}^2$.

A homogeneous distribution of the electrons over the cross section is assumed. The target density of the electrons in the cooler with $\beta_{\text{Beam}} \gg \beta_e$ is d_{t0}. The electrons stay for a time $t = \frac{L_{\text{Cooler}}}{\beta_e \cdot c}$ in the cooler, so the number of electrons in the cooler is $\frac{I_e}{e} \cdot \frac{L_{\text{Cooler}}}{\beta_e \cdot c}$, where e denotes the elementary charge e. The target density is:

$$d_{t0} = \frac{I_e}{e} \cdot \frac{L_{\text{Cooler}}}{\beta_e \cdot c \cdot A_{\text{Cooler}}} \tag{3.6}$$

But the real target density d_t is reduced, because the electrons possess a finite velocity and only the part of electrons contribute, which have been passed by the protons. While the protons are in the electron cooler $t_{p\text{EC}} = \frac{L_{\text{Cooler}}}{\beta_{\text{Beam}} \cdot c}$ the relative distance between electrons and protons is $\Delta l = v_e \cdot c \cdot t_{p\text{EC}}$. As a result the target density is calculated by:

$$dt = d_{t0} \cdot \frac{\Delta l}{L_{\text{Cooler}}} = \frac{I_e}{e} \cdot \frac{L_{\text{Cooler}}}{\beta_e \cdot c \cdot A_{\text{Cooler}}} \cdot \frac{\beta_{\text{rel}}}{\beta_{\text{Beam}}} \tag{3.7}$$
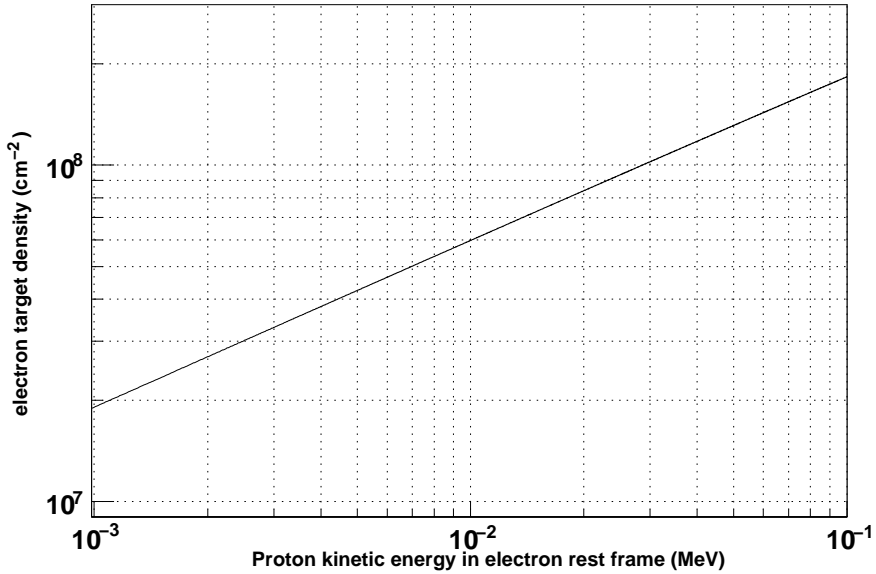
Figure 3.6: Target density as a function of proton kinetic energy in the electron rest frame.

3.4.3   Thermal Motion of the Electrons

Additionally to the electron motion due to the acceleration voltage a thermal motion is superimposed. This leads to a distribution of the electron velocities $\overrightarrow{v_e}$. Therefore, the

expression, eqn. 3.2, for the beam depolarization then becomes

$$\frac{dP}{dt} = -2\frac{L_{\text{Cooler}}}{L_{\text{R}}}n_e\langle v\sigma_S(v)\rangle P. \tag{3.8}$$

From now on, P signifies the beam polarization, L_{Cooler} is the active length of the cooler, L_{R} the ring circumference, n_e the electron number density, and the angular bracket represents an average over the velocity distribution. Equation 3.8 is evaluated in the proton rest frame, however the product $n_e dt$ is Lorentz-invariant, allowing the use of laboratory values for time and electron density. The latter is given by

$$n_e = I_e/(eA_e v_e c). \tag{3.9}$$

The next step is to evaluate the average over the distribution of relative velocities.

Relative velocity distribution in the proton rest frame

The calculations are performed in the frame $\{R\}$ where the beam protons are at rest. The beam magnitudes (in units of c) are β_p and γ_p. The relative velocity is abbreviated with v. With the z-axis along the cooler axis, v has the components v_z, $v_\rho sin\phi$ and $v_\rho cos\phi$ in a cylindrical coordinate system. In this coordinate system all velocities are small and a non-relativistic description is appropriate.

The electron velocity distribution is assumed to have two contributions. The first one, v_z^0, is along the cooler axis, and is caused by detuning the electron acceleration voltage by ΔU

$$v_z^0 = \gamma_p^2(\beta_e(\Delta U) - \beta_p), \tag{3.10}$$

where $\beta_e(\Delta U)$ and β_p are the electron and proton laboratory velocities, and $\beta_e(0) = \beta_p$. The γ_p^2 factor transforms the laboratory velocity in brackets into the $\{R\}$ frame. The second component appears due to a random sideways motion. This is described by a Maxwell distribution with an effective temperature of $kT_e = 0.2\,\text{eV}$ (in the laboratory) [Ste]. The characteristic velocity ξ is defined by

$$\xi = \gamma_p\sqrt{\frac{kT_e}{m}} = 0.659 \cdot 10^{-3}(\text{units of c}) \tag{3.11}$$

where m is the electron mass. The γ_p factor transforms a sideways velocity in the laboratory into the $\{R\}$ frame. The velocity distribution is then written as

$$g(\vec{v})d^3\vec{v} = \frac{1}{2\pi\xi^2}e^{-\frac{v_\rho^2}{2\xi^2}}\delta(v_z - v_z^0)v_\rho dv_\rho d\phi dv_z, \tag{3.12}$$

with the normalization

$$\int g(\vec{v})d^3\vec{v} = 1\,. \tag{3.13}$$

The longitudinal random component is neglected. Assuming again a Maxwell distribution, for the corresponding temperature an upper limit of $kT_\parallel < 0.015\,\text{eV}$ has been

determined experimentally [Ste]. This number reflects the limitations of the method, and the actual value could be much smaller. The characteristic velocity at this temperature is $\xi_\parallel = 1.8 \cdot 10^{-4}\,\mathrm{c}$. This value is about 25 % of its sideways counterpart (eqn. 3.11). Since in all expressions only the square of ξ appears, it occurs at most a $0.25^2 = 7\%$ effect.

The electron acceleration voltage is $U = 26.849\,\mathrm{keV}$ in cooling mode. At this voltage the oscillation is about $10^{-4} \cdot U \approx 3\,\mathrm{V}$. In $\{R\}$, this corresponds to a velocity change of $0.02 \cdot 10^{-3}\,\mathrm{c}$, which is completely negligible compared to the *ep* relative velocity of $v_z^0 = 1.46 \cdot 10^{-3}\,\mathrm{c}$ ($\Delta U = 245\,\mathrm{V}$ was the lowest value used).

Averaging over the velocity distribution

There are two *different* interaction cross sections, namely $\sigma_\perp$ when $\overrightarrow{v_e}$ and $\overrightarrow{P_B}$ are orthogonal or $\sigma_\parallel$ when $\overrightarrow{v_e}$ and $\overrightarrow{P_B}$ are parallel. As a result the average $\langle v\sigma_S(v)\rangle$ in eqn. 3.8 should be replaced by:

$$\overline{v_e}\left[\alpha\sigma_\perp\left(\overline{v_e}\right) + (1-\alpha)\,\sigma_\parallel\left(\overline{v_e}\right)\right],\tag{3.14}$$

where $\overline{v_e}$ is the relative velocity, averaged over the distribution, and α is the weight with which the two cross sections contribute to the measurement.

The weighted average over $v \cdot \sigma(v)$ is now given by

$$\langle v \cdot \sigma(v)\rangle = \int v \left[\sigma_\perp \cdot \frac{v_\rho^2 cos^2\phi + v_z^2}{v^2} + \sigma_\parallel \cdot \frac{v_\rho^2 sin^2\phi}{v^2}\right] \cdot g(\vec{v})d^3\vec{v}.\tag{3.15}$$

The weights are chosen quadratically with the velocity, as the cross section $\sigma_{\perp,\parallel}$ is inversely proportional to the v^2

$$\sigma_{\perp,\parallel}(v) = \sigma_{\perp,\parallel}(v^\star)\frac{v^{\star2}}{v^2}.\tag{3.16}$$

Here, $v^\star$ is some arbitrarily chosen reference velocity and $\sigma_{\perp,\parallel}(v^\star)$ are the depolarization cross sections at that velocity. Equation 3.16 is not a model assumption, but much more fundamental. This velocity dependence is discussed by Milstein et al. [Mil08], and follows from their equation 20, when neglecting the logarithmic term (which amounts to only a few percent). It is also in agreement with the errata by Arenhövel and Walcher [Are09].

Inserting $g(\vec{v})$ into eqn. 3.15, carrying out the integration for ϕ from 0 to 2π, eliminate the δ-function, and substituting $v_\rho^2 = v^2 - (v_z^0)^2$ (it is $v_\rho dv_\rho = vdv$), one obtains

$$\langle v \cdot \sigma(v)\rangle = \frac{1}{2\xi^2}\int_{v_z^0}^\infty \left[\sigma_\perp(v)\left(1 + \frac{v_z^{02}}{v^2}\right) + \sigma_\parallel(v)\left(1 - \frac{v_z^{02}}{v^2}\right)\right] e^{-\frac{v^2 - v_z^{02}}{2\xi^2}} v^2 dv\,.\tag{3.17}$$

Using once again the velocity dependence of the cross section (eqn. 3.16) yields

$$\langle v \cdot \sigma(v)\rangle = v^{\star2}\sigma_\perp(v^\star)\cdot I_\perp(v_z^0) + v^{\star2}\sigma_\parallel(v^\star)\cdot I_\parallel(v_z^0),\tag{3.18}$$

with

$$I_\perp(v_z^0) = \int_{v_z^0}^\infty \frac{1}{2\xi^2}\left(1 + \frac{v_z^{02}}{v^2}\right) e^{-\frac{v^2 - v_z^{02}}{2\xi^2}}dv\,,\text{ and}\tag{3.19}$$

$$I_\parallel(v_z^0) \quad = \quad \int_{v_z^0}^{\infty} \frac{1}{2\xi^2}\left(1 - \frac{v_z^{0^2}}{v^2}\right) e^{-\frac{v^2 - v_z^{0^2}}{2\xi^2}}\, dv \;. \tag{3.20}$$

The contribution between 0.004 and ∞ is completely negligible so the non-relativistic calculation is valid. The integrands of eqs. 3.19 and 3.20 are called $h_\perp(v)$ and $h_\parallel(v)$. These functions, shown in fig. 3.7, tell (for a given ΔU) what relative velocities contribute. The
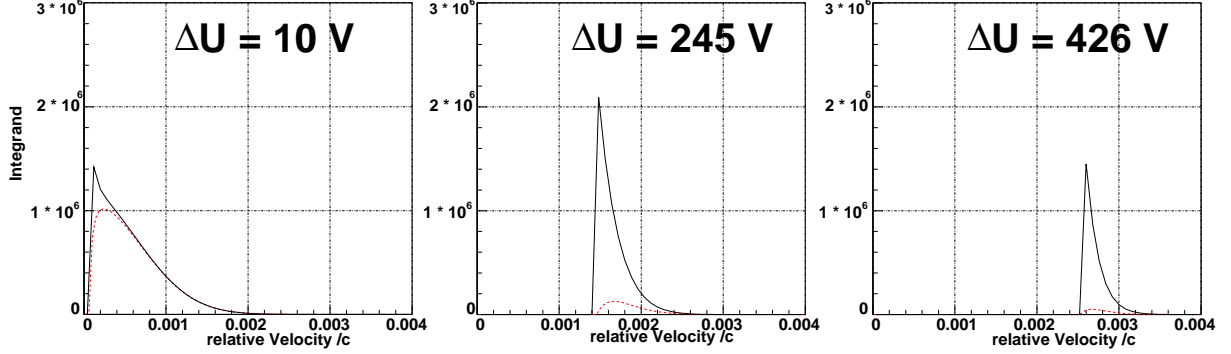
Figure 3.7: The integrands $h_\perp$(solid line) and $h_\parallel$(dashed line) *vs* the relative velocity v (in units of c) for three different detune voltages. Instead of no detune voltage, a small voltage (10V) is used so that the difference between the two weights becomes visible.

average velocity and its rms value are calculated as

$$\overline{v_j} \quad \equiv \quad \int v \cdot h_j\; dv / I_j \quad and \tag{3.21}$$

$$\Delta\overline{v_j} \quad \equiv \quad \left(\int (v - \overline{v_j})^2 \cdot h_j dv / I_j\right)^{\frac{1}{2}}. \tag{3.22}$$

It turns out that $\overline{v_\perp} \approx \overline{v_\parallel}$ and $\delta\overline{v_\perp} \approx \delta\overline{v_\parallel}$, therefore mean values are used:

$$\overline{v} \quad \equiv \quad \frac{1}{2}(\overline{v_\perp} + \overline{v_\parallel}) \quad and \tag{3.23}$$

$$\Delta\overline{v} \quad \equiv \quad \frac{1}{2}(\delta\overline{v_\perp} + \delta\overline{v_\parallel}) \tag{3.24}$$

For the five used detune voltages these values are given in tab. 3.3.

3.4.4 Electron Drag Force

When the electron velocity is increased a so-called drag force pulls the proton beam to the new electron velocity. To evaluate this effect the proton orbit frequency is measured. Figure 3.8 shows Schottky spectra of the proton orbit frequency for different times after the start of the detuning interval. The detuning voltage was $\Delta U = 245\,\text{V}$, which is the lowest detuning voltage, so that the effect of the drag force is largest. The centroid of the distribution shifts proportionally with time by about $80\,\text{Hz}$ in $10\,\text{s}$. The width jumps to about $60\,\text{Hz}$ (FWHM) as soon as the electron beam is accelerated. The velocity change in the $\{R\}$ frame is given by

$$\Delta\beta_p = \frac{\beta_p}{\eta}\frac{\Delta f_R}{f_R} = \Delta f_R \cdot 8.7 \cdot 10^{-7}\,\text{s}. \tag{3.25}$$

ΔU (V)	v_z^0 (10^{-3} c)	$I_\perp(v_z^0)$ (c)	$I_\parallel(v_z^0)$ (c)	$\overline{v}$ (10^{-3} c)	$\Delta\overline{v}$ (10^{-3} c)	T_h (nominal) (keV)	T_h (average) (keV)	ΔT_h (average) (keV)
0	0	951.7	951.7	0.525	0.397	0.00	0.41	0.33
245	1.456	526.1	66.8	1.750	0.222	0.99	1.51	0.40
301	1.788	459.4	43.5	2.051	0.200	1.50	2.03	0.41
348	2.066	413.9	31.5	2.307	0.185	2.00	2.55	0.42
426	2.526	353.7	19.4	2.738	0.162	2.99	3.56	0.44

Table 3.3: Detune voltage ΔU, longitudinal drift velocity v_z^0, the integrals $I_\perp(v_z^0)$ and $I_\parallel(v_z^0)$, the average velocity $\overline{v}$ and its rms width $\Delta\overline{v}$ (not an uncertainty), and the proton kinetic energy T_h in the electron rest frame (the "nominal" value is calculated without thermal motion).
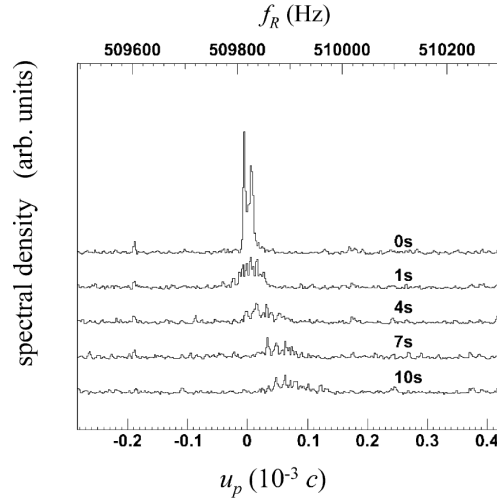
Figure 3.8: Schottky spectra (distribution of orbit frequency) of the stored proton beam. The top trace is measured when the beam is cooled. The remaining traces show the evolution of the distribution after a detune voltage of 246 V has been applied. The bottom scale shows the proton velocity u_p relative to its value at the start of the detune interval. The measurements cover a period of 10 s.

Here, $\eta = \frac{\Delta f_R/f_R}{\Delta B/B} = 0.7$ is the relative frequency change divided with the corresponding relative magnetic field change and is called frequency slip factor. It has been measured by observing the orbit frequency as a function of the change of the dipole field.

Thus, the proton velocity shift in 5 s is $0.035 \cdot 10^{-3}$ c, and the rms value of the distribution is $0.022 \cdot 10^{-3}$ c. Both numbers are negligibly compared to the electron-proton relative velocity of $v_z^0 = 1.46 \cdot 10^{-3}$ c corresponding to $\Delta U = 245$ V which was the lowest value used with different velocities of electrons and protons.

3.5 Deuterium Cluster Target

The deuterium cluster target [Mer07] is installed in the internal target position of the ANKE experiment. It provides high target densities in a small beam target overlap region together with a gas load in the target chamber, which is comparable to the integral of the ring without cluster target. In Fig. 3.9 a schematic view of the cluster target is given.
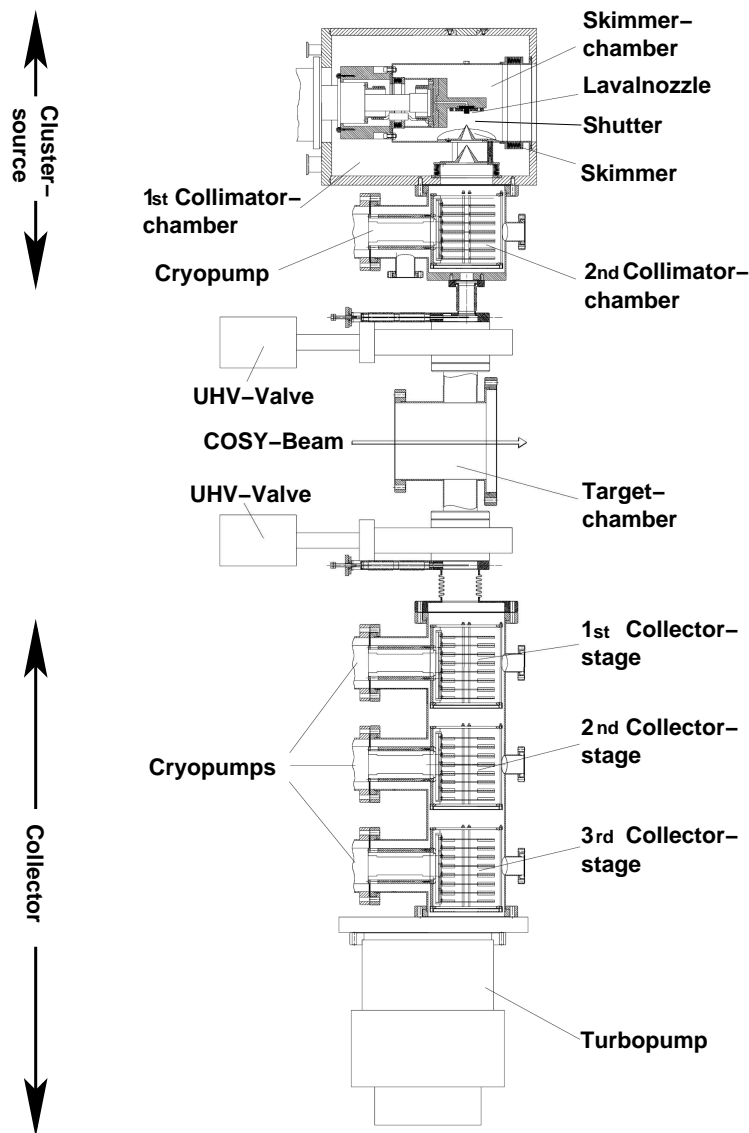
Figure 3.9: Schematic view of the cluster target. [Mer07]

Cluster Source In the part of the target indicated as cluster source the clusters are produced. Pure hydrogen or deuterium gas is cooled below vapor pressure curve to a temperature of 20 to 30 K. At a pressure of 15 to 20 bar the gas is pressed through a lavalnozzle with an opening diameter in the order of $20\,\mu$m into the vacuum of the skimmer chamber. Here the gas expands adiabatically and further cools down. In this over-saturated gas spontaneous condensation of atoms to clusters occur. These clusters consist of roughly 10^3 atoms close to the triple point. By the skimmer the cluster beam is separated from the residual gas, which is the biggest part of the total gas load into the skimmer chamber. By a shutter the skimmer can be blocked and thus the target switched on/off within less than 1 s.

Together with a collimator behind the skimmer and turbo- and cryo-pumps a differential pumping system is installed to reduce the gas load into the ring vacuum of $\approx 10^{-7}$ mbar. Additionally the collimator cuts the cluster beam.

Assuming a linear dispersion, this settles the extension of the cluster beam at the COSY beam.

Collector   In order to avoid the cluster beam to spoil the ring vacuum, three cryo-pumps and one turbomolecular pump is installed underneath the target chamber. The cluster beam directly hits the rotor blades of the turbomolecular pump and most of it is pumped directly. The vacuum at the turbomolecular pump is $> 10^{-5}$ mbar and the three cryo-pumps act as a differential pumping system to the target chamber.

3.6   Detection Setup

As described in sec. 3.2 the beam polarization is measured by analyzing proton-deuteron elastic scattering events. In order to detect these events, two ANKE-Silicon Tracking Telescopes (STT) have been installed close to the beam target overlap region. This detection system was designed to take data on double polarized proton-proton or proton-deuteron collisions. A polarized proton or deuteron beam is provided by COSY and the ABS of the ANKE Spectrometer is used to generate a polarized target. Especially the identification and tracking of low energy spectator protons allows to use the polarized deuteron gas of the ABS as a polarized neutron target and e.g. to study reactions of the type $pn \rightarrow pnX$ or $pn \rightarrow pdX$.

The basic detection concept is to combine particle identification of stopped particles by the $\Delta E/E$ method and particle tracking over a wide energy range. These issues are provided by double-sided silicon strip detectors that provide:

- $\Delta E/E$ proton identification from 2.5 up to 40 MeV kinetic energy. The telescope structure of 65(or 300), 300, 5500 μm thick double-sided silicon-strip detectors, read out by high dynamic range chips, allows $\Delta E/E$ particle identification over a wide dynamic range.

- self-triggering capabilities. By a fast amplifier with a peaking time of 75 ns a particle passage is identifies fast and provide a trigger, so that the system can be used as a stand alone detector.

- particle tracking over a wide range of energies, starting from 2.5 MeV spectator protons and reaching up to minimum ionizing particles.

- high rate capability.

- high modularity, in order to optimize the detection system for each experiment individually.

3.6.1   Silicon Microstrip Detectors

The double sided silicon microstrip detectors can be split logically into two groups. For the first two layers detectors with thicknesses of 69 μm up to 500 μm are available. Their pitch in the order of 400 μm is chosen to fulfill the tracking requirements. The last layer

usually consists of a $5500\,\mu$m thick silicon detector and is used to maximize the stopping capabilities of the detection setup.

During the depolarization experiment $300\,\mu$m detectors were used in the first and second layer, as the detection of proton-deuteron elastic events with a 49.3 MeV proton beam, does not need a low energy-threshold. A $5500\,\mu$m thick third layer was installed, but not used in the analysis.

In the following the $300\,\mu$m detectors are described in detail.

The BaBar IV Detectors

The detectors, which are used for the first two layers of the tracking telescope, have been originally designed for the BaBar experiment [Bou95, Boz01, Boz00, BaBar284, BaBar312] at the SLAC PEP-II B factory [PEP] by the British company Micron Ltd. [MIC]. As the size of their active area is suitable for the silicon tracking telescopes the reuse of their construction, masks and production facilities builds a cost efficient alternative to a complete redesign. To provide AC-coupling for each strip already on the detector, an additional mask is vacuum metallized onto both sides. The p-doped side the detector has 1023 strips and the n-doped side has 631 strips.

To increase the effective strip pitch to about $400\,\mu$m strips are connected to each other and segments are created. This is done in two steps. On the detector the strips are combined to groups and on the kapton flat cable, which is used to connect the detector with the front-end electronics, these groups are connected to segments. The connection scheme is displayed in fig. 3.10.

With this large number of readout channels (one per segment) a vacuum-feedthrough for each segment is not achievable and a front-end electronics in vacuum is necessary (sec. 3.6.2).

3.6.2 Front-end Electronics

The signals from the silicon microstrip detectors are transmitted via kapton flat cables to the in-vacuum front-end electronics. As their center part the VA32TA2[1] chips are used. It has 32 channels which can be logically split into an amplitude and a trigger part. A charge signal provided on the input pad of a channel is amplified in the preamplifier stage. After the preamplifier the signal is split into the two branches. The chip provides a low trigger threshold of 100 keV and can handle the signals from a variety of detectors ranging from 2.5 MeV for protons in a $69\,\mu$m silicon detector to about 40 MeV for deuterons in a 5 mm thick lithium drifted silicon detector. For each detector side two boards (90 mm x 90 mm) with 5 chips are used (fig. 3.11). The pre-processed signals are then further transmitted by additional kapton flat cables to the vacuum feedthrough connectors. On the electronic board are connectors, so that the kapton flat cables can be dismounted and the system is kept as modular as possible.

---

[1]produced by Ideas ASA, Norway
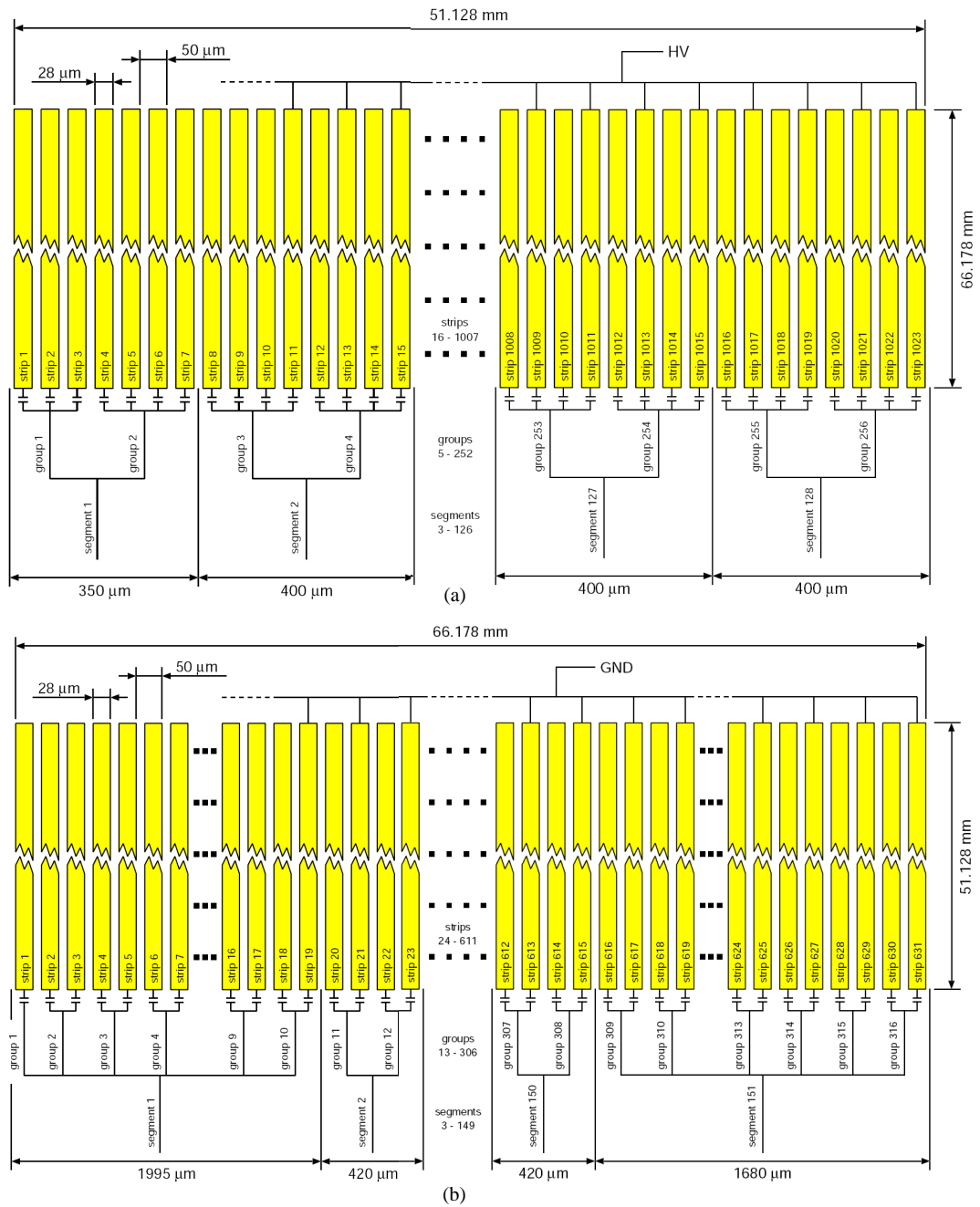
Figure 3.10: Geometry and connection scheme of the p-doped (a) and n-doped (b) sides of the BaBar IV detector [Mus07].
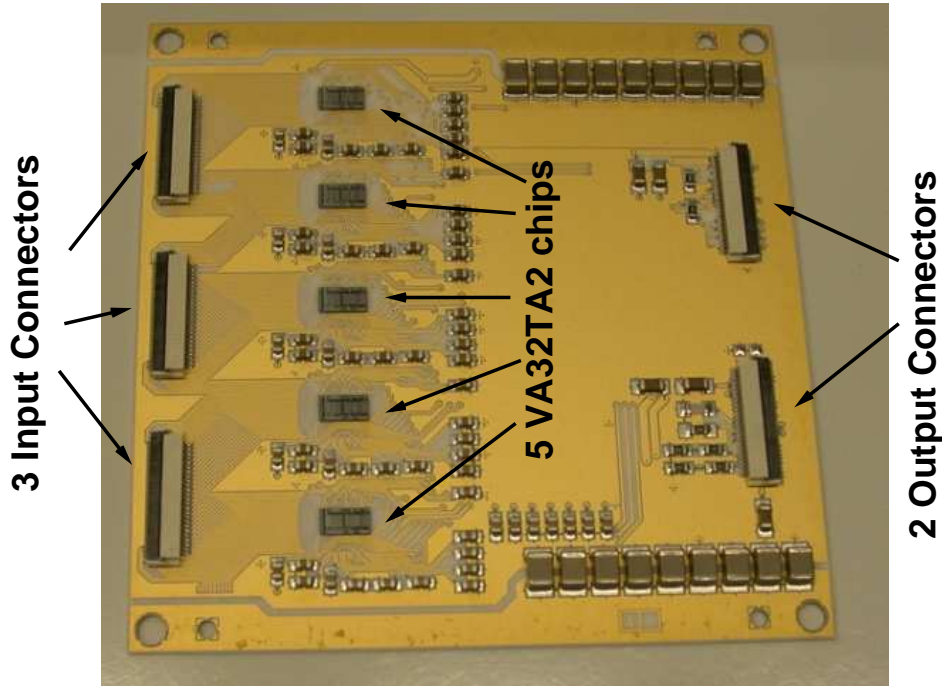
Figure 3.11: Picture of the in-vacuum front-end electronic board showing the three input connectors, the five VA32TA2 front-end chips as well as the output connector.

Each front-end electronics board is controlled via one interface card outside of the vacuum. The interface cards provide power supplies, control signals, trigger pattern threshold, and calibration pulse amplitudes. The total read-out chain guarantees a total dead time of less than $50\,\mu$s. More details about the front-end electronics can be found in [Mus07].

3.6.3 Cooling

The cooling of the detection system fulfills two main purposes. Firstly, it stabilizes the front-end electronics temperature at room temperature. The temperature gradient on the board ought to be minimized and the drift of the temperature during data taking and calibration has to be smaller than $5\,$K in order to achieve a constant energy-response of the chips. The second purpose is cooling of the detectors. Here two demands have to be met. The dark current must be reduced to ensure operation and noise reduction. Secondly, the charge collection time has to be small and stable to realize a constant time delay between hit and maximum charge on the preamplifier. The dependence of the dark current I_{dark} and the drift velocity v_{e^-} (v_h) of electrons (holes) from the detector temperature is given by:

$$I_{\text{dark}} \quad \propto T^2 \cdot e^{-\frac{0.62\,\text{eV}}{k_B \cdot T}} \tag{3.26}$$
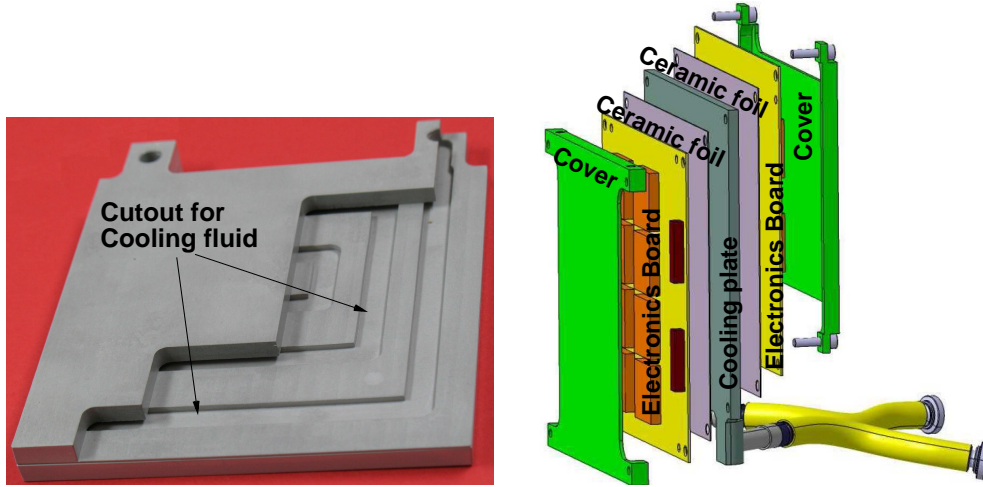
Figure 3.12: Pictures of the cooling plate. Left: A half cut so that the meandered cutout for the cooling fluid becomes visible. Right: An explosion sketch of the assembly: One cooling plate with two electronic boards. The shown parts are (from left to right): a cover, an electronics board, a ceramic foil, a cooling plate, a ceramic foil, an electronics board and a cover.

$$v_{e^-} \quad = 2.1 \cdot 10^{-9} \, \frac{\text{cm}^2}{\text{Vs}} \cdot \frac{U}{d} \cdot (T/\text{K})^{-2.5} \tag{3.27}$$

$$v_h \quad = 2.3 \cdot 10^{-9} \, \frac{\text{cm}^2}{\text{Vs}} \cdot \frac{U}{d} \cdot (T/\text{K})^{-2.7} \tag{3.28}$$

Here k_B is the Boltzmann-constant, U the bias voltage, d the thickness and T the temperature of the detector. From all three equations a low detector temperature is preferable. To achieve these points it is necessary to transport the cooling fluid as close as possible to the detectors and the frond-end electronics. A mixture of ethanol and water as cooling fluid is pumped through aluminum plates with a thickness of $3\,\text{mm}$. A typical temperature for the cooling fluid in this plate is $-20\,°C$ and will provide a heat-drain for all three detectors.

In fig. 3.12 one cooling plate is shown together with a half cut of a cooling plate and an explosion picture showing the assembly of one cooling plate with two front-end electronic boards and cover plates for protection. A $200\,\mu\text{m}$ thin ceramic foil [CER] adjusts mechanic inaccuracies to ensure a good planar heat connection.

3.6.4   Assembly

In order to gain maximum flexibility, one detector together with it's two front-end boards and one cooling plate builds up a unit (fig. 3.13). Each unit can be tested and calibrated individually. The detectors are mounted on a aluminum frame with four feet, very much like a table. These units are mounted - without being disassembled - to one telescope (STT): The feet of the table are screwed to the next detector-frame and thus by using frames with different length of the feet, the distance between two layers can be adjusted.

Each telescope is mounted on a CF-DN 160 flange. To achieve maximum mechanical precision, all parts fixed with two h7 dowel pins. On the frame of the thick detector one additional cooling plate is fixed. Here also a $200\,\mu\text{m}$ thin ceramic foil is used.
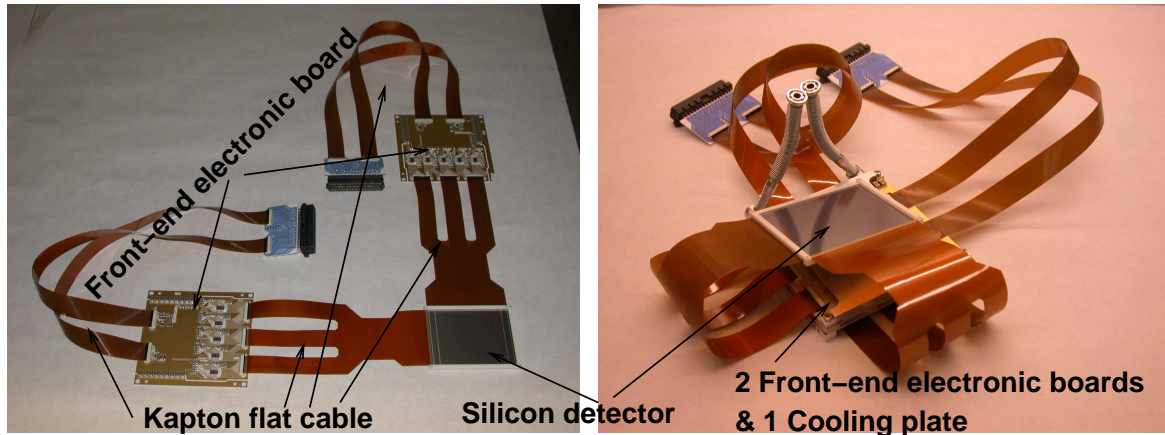
Figure 3.13: The left picture shows one detector together with the front-end electronic boards and the kapton flat cables. The right picture shows the complete assembly for one detector including the cooling plate for the electronic boards.

The second and the first layer are added subsequently. The electronic boards of the first layer are mounted in the most rear position to avoid a disarrangement of the kapton flat cables.

3.6.5 Geometry

The positioning of the detectors has been optimized to measure the beam polarization from proton-deuteron elastic scattering. Here four aspects have to be met:

- At a constant luminosity the beam polarization is to be determined with a small statistical error.

- The setup has to be build in a ϕ-symmetric (left-right) arrangement to make use of the double ratio method (sec. 4.4).

- To protect the detectors from radiation damage space to the beam is needed.

- Events with proton and deuteron tracks should be in the acceptance of the detection system, in order to align the setup.

A schematic view of the detection system build from two STT's is given in fig. 3.15. The first layer is placed 28 mm from the center of the beam pipe. Additionally, one aperture made of copper is placed 36 cm upstream. It has an inner diameter of 55 mm and a thickness of 50 mm to stop all secondary particles produced by the beam in the copper. By this the detectors should be protected from a direct hit of the beam.

The distance between the two first layers is set to 20 mm. The complete setup is moved 12 mm downstream. A Monte-Carlo simulation shows that the geometrical acceptance of
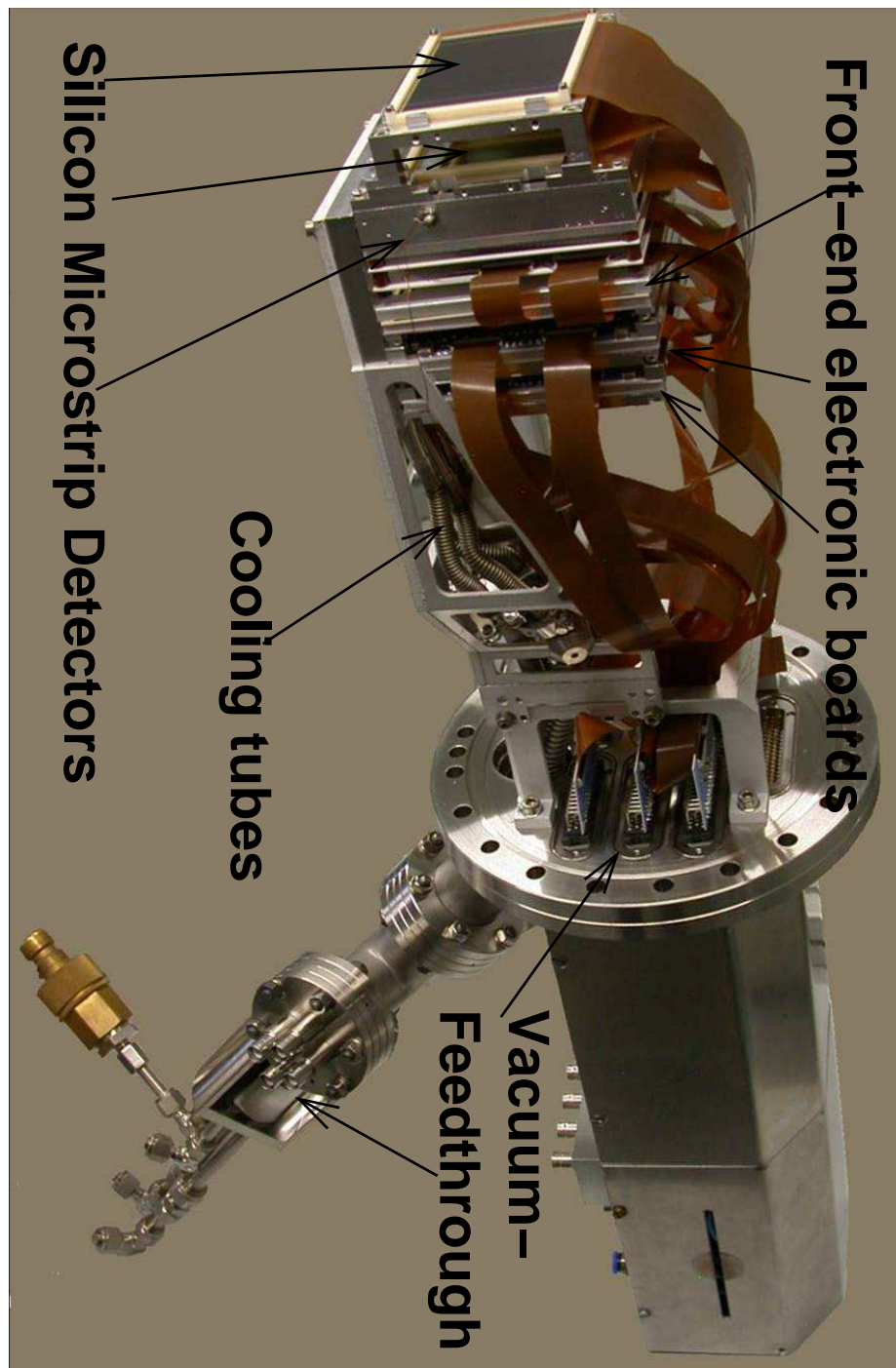
Figure 3.14: This picture shows the complete setup of one silicon tracking telescope (STT). It is equipped with three silicon microstrip detectors and the front-end electronic boards. The kapton flat cables from the detectors to the frond-end electronic and further to the vacuum-feedthrough are visible.
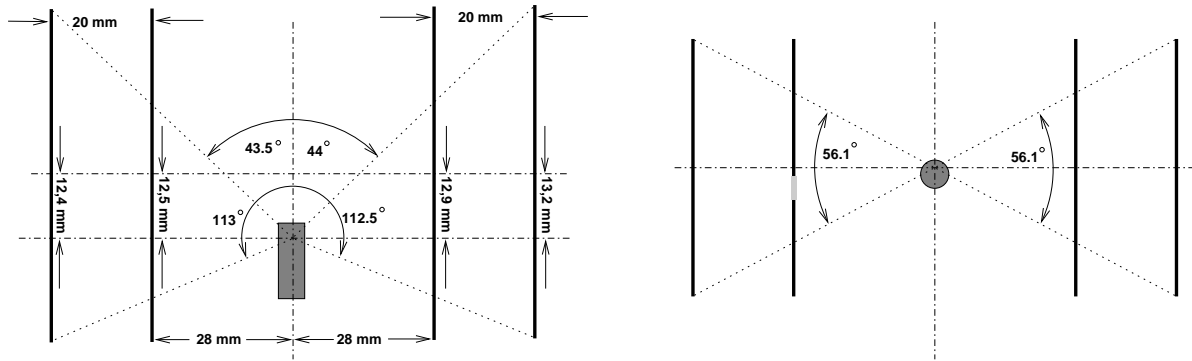
Figure 3.15: Left: A schematic view of the detection setup from the top with the proton beam pointing upwards. Right: A schematic view of the detection setup in beam direction. The gray circle indicates the beam target overlap. The given values for the geometry are taken by a 3-D coordinate measurement and the angles given indicate the geometrical acceptance for the scattering angle θ and the azimuthal angle ϕ. In the right figure a region of the detector is marked gray, as this returns no useful data due to a direct hit of the proton beam.

the detection setup is optimized to detect elastic scattering deuterons, so that the precission of the polarization measurement is maximized and all additional requirements are met.

3.7 Data Taking

3.7.1 Beam Development

With the previously described setup, data on the electron proton spin-flip was taken in February 2008. Previiently, from February 1 to 19 a machine development time of COSY took place. This machine development was intended to increase the polarization of a stored proton beam as a beam polarization of maximum $50\,\%$ was observed in the year 2007. The beam polarization was measured using proton deuteron elastic scattering events at COSY injection energy $T = 44.8\,\text{MeV}$. The trigger signal was generated, when at least one track was generated in the detection system. This is realized by demanding a coincidence between both sides of any second layer. The complete detection system and not only the silicon tracking telescope, from which the trigger was produced, was read out.

By changing the current of the electron-cooler solenoid, a partial snake was introduced and the vertical beam polarization was measured as a function of the solenoid current. A snake turns the stable polarization direction in a cyclotron from the vertical direction into the beam direction. While in a full snake the rotation is complete, a partial snake gives only a fractional rotation. When the beam polarization is partially turned in to the beam direction, the measured vertical beam polarization drops. So the observed low beam polarization in COSY could be caused by a partial snake. Figure 3.16 shows the maximum

vertical beam polarization without a solenoidal field. So a longitudinal magnetic field can be excluded at COSY and is not the reason of the observed low beam polarization.
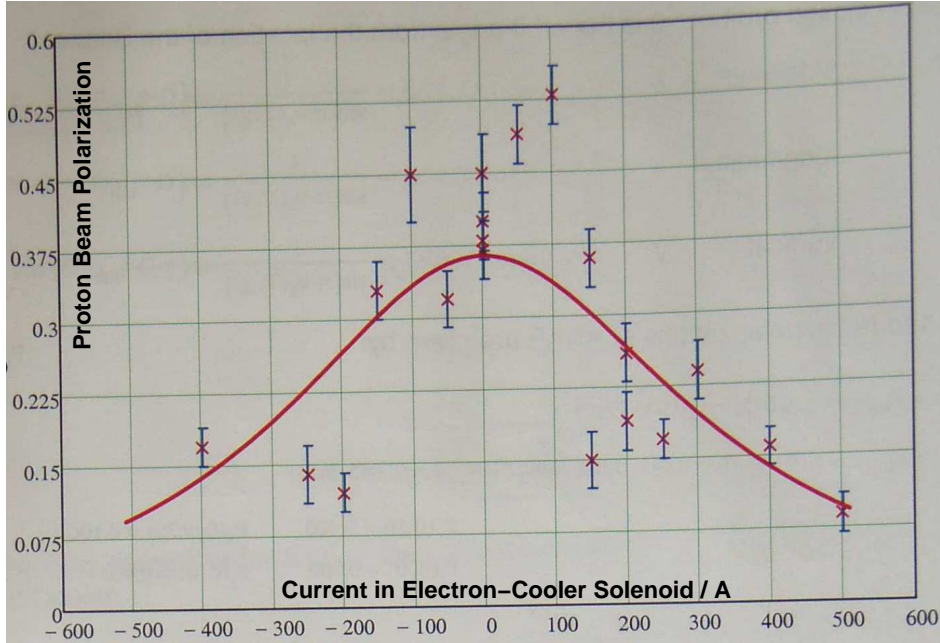
Figure 3.16: The polarization of a stored proton beam at injection energy was measured as a function of the current in the electron-cooler solenoid. The maximum polarization occurs at zero current.

As a second point the beam polarization was measured for different machine tunes[2]. A scan of Q_y with a fixed $Q_x \approx 3.58$ as well as a Q_x-scan with a fixed $Q_y \approx 3.54$ was performed. Both scans show no effect on the beam polarization. By this, high order resonances can be excluded as a reason for the low beam polarization.

For these studies the silicon detection system was already installed at the ANKE target point and proton-deuteron elastic scattering data were taken. Its online-analysis was used to give fast results during the machine development.

3.7.2   Data on Electron-Proton Spin-Flip

As a first step, COSY was prepared for the electron-proton spin-flip cross-section measurement. An acceleration ramp to $T = 49.3 \, \text{MeV}$ ($p = 308.15 \, \text{MeV/c}$) was introduced and the beam position was optimized to fit both to electron cooling and optimized beam target overlap with the ANKE cluster target. Additionally, the COSY software timing was adjusted to the cycle setup (sec. 3.3), where especially the change in the electron cooler parameters had to be taken into account. The tables showing these setting are attached in

---

[2]The tunes gives the number of turns of the particle in the phase space per revolution in the cyclotron.

App. C. The total COSY super-cycle consists of six injections: three times "0"-Cycle and "E"-Cycle. Two pairs with polarized beam (↑ and ↓) and one unpolarized pair of cycles (fig. 3.17).
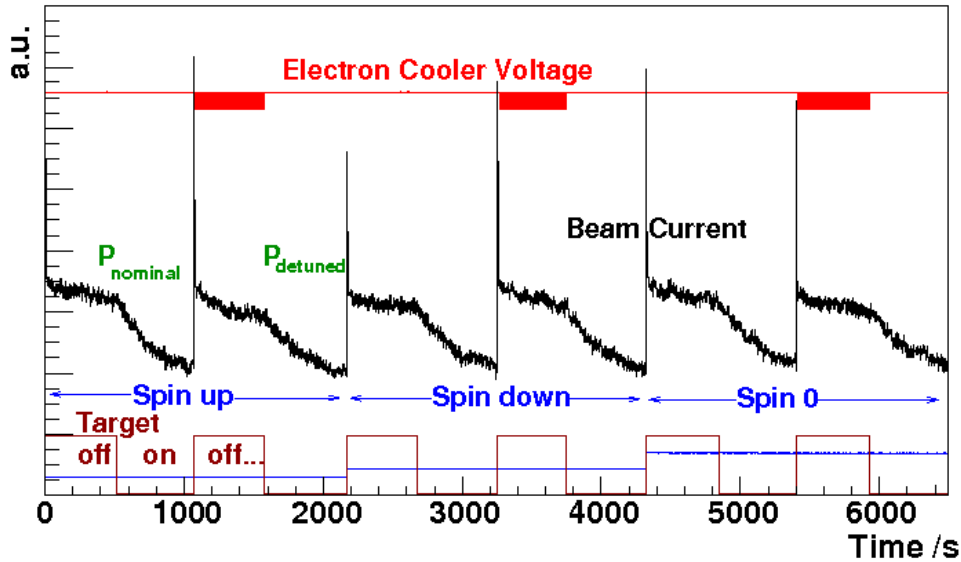
Figure 3.17: The six different cycles of COSY indicate the used Supercycle structure. Three different beam polarization states combined with two different electron cooler approaches (one with and one without electron target) give the COSY Supercyle.

From February 20 9:30am to February 25 8:00am data on the electron-proton spin-flip cross-section were taken. In total six different detuning voltages were used. They are $\Delta U = -426, 0, 246, 301, 348$ and $426\,\mathrm{V}$ and correspond to (neglecting the thermal movement) $T_p^e = -3, 0, 1, 1.5, 2$ and 3 keV proton kinetic energy in the electron rest frame. The minus (plus) sign indicates electrons moving slower (faster) than the beam protons.

The injected beam had a polarization of $\approx 50\,\%$ with intensities between $4 \cdot 10^7$ to $2 \cdot 10^8$ stored protons. In fig. 3.18 a picture from an oscilloscope is given. The lines indicate (from top to bottom): Count-rate of ANKE forward-system, electron-cooler high voltage, rate of recombined H^0 (cooling electrons and beam protons) and beam current during "0"-cycle and "E"-cycle.

Bad Spectra   From time to time, the uncorrected (RAW) QDC-spectra show a rapid change of the pedestal lines for each strip separately (fig. 3.19). This effect occurs only from the positive-doped sited of the silicon detectors. Due to these jumps, it is impossible to distinguish hits from noise and this data can not be used in analysis. A reset of the affected front-end electronic boards solved the problem. Always a new file for the data was started, to divide *good* from *bad* data.

In total 38 files of *good* data on all energies have been taken (tab. 3.4). The statistics of this data is sufficient to answer the question, whether the *ep* spin-flip provides a tool for
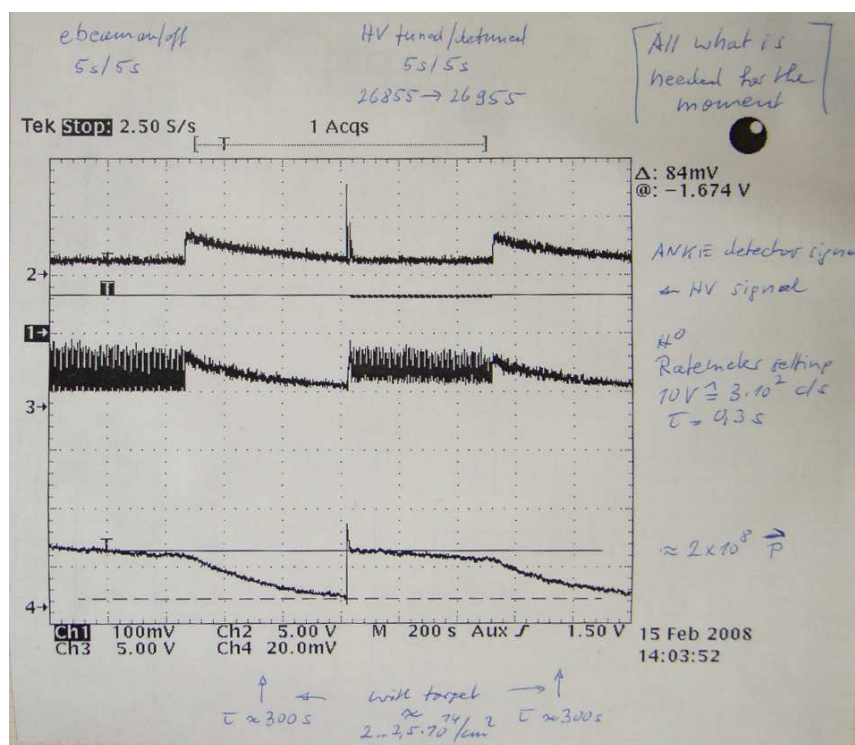
Figure 3.18: From top to bottom: Count-rate of ANKE-forward system, electron-cooler high voltage, rate of recombined H^0 (cooling electrons and beam protons) and beam current during "0"-cycle and "E"-cycle.

polarization build-up of antiprotons.
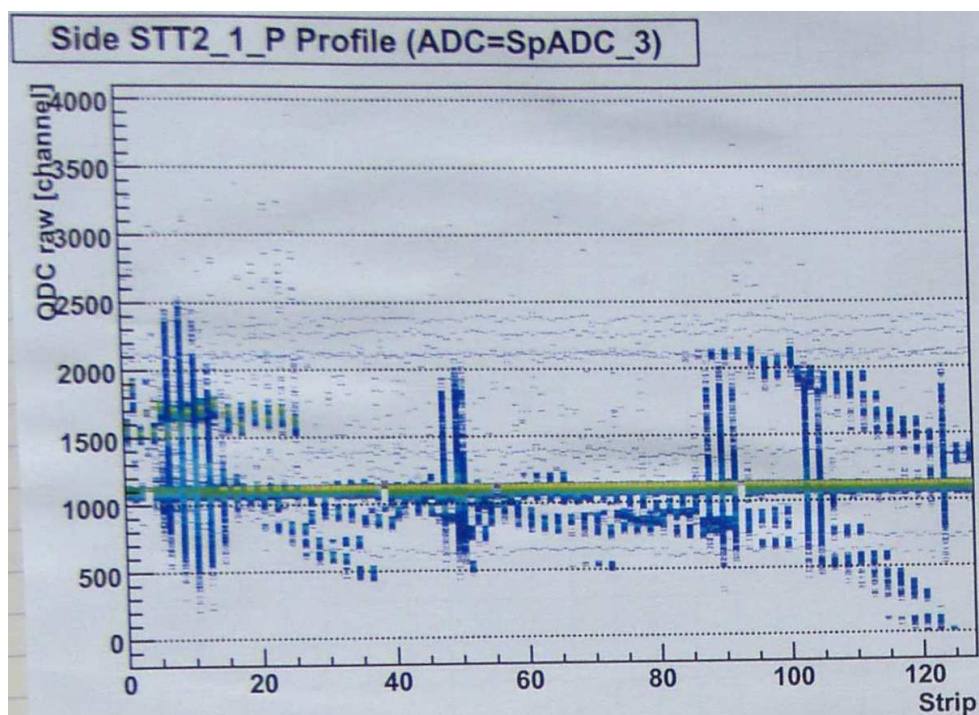
Figure 3.19: The uncorrected (RAW) QDC-spectra of all strips from the positive-doped detector side from the first layer of the right (in beam direction) telescope. A rapid change of the pedestal lines for each strip separately is visible.

Date(Start)	Start	Stop	Events	Run-Number	Comments
$\Delta U = 246\,\text{V}$					
Feb. 20, 2008	09:37	15:21	936584	872	
Feb. 20, 2008	15:22	02:23	1714330	873	only $1.2 \cdot 10^6$ good events
$\Delta U = 348\,\text{V}$					
Feb. 21, 2008	18:52	07:29	1389612	880	
Feb. 22, 2008	07:29	08:08	47827	881	
Feb. 22, 2008	10:55	12:57	971061	902	
Feb. 22, 2008	12:57	16:35	1304605	903	
Feb. 22, 2008	16:36	21:29	1418559	904	
Feb. 22, 2008	21:29	22:15	201522	905	
$\Delta U = 426\,\text{V}$					
Feb. 22, 2008	22:22	01:55	1171574	906	
Feb. 23, 2008	01:57	05:26	1265026	907	
Feb. 23, 2008	05:27	09:15	1293614	908	
Feb. 23, 2008	09:16	12:47	1413324	909	
Feb. 23, 2008	12:48	15:27	944530	910	
$\Delta U = -426\,\text{V}$					
Feb. 23, 2008	15:30	17:52	785698	911	
Feb. 23, 2008	19:11	22:49	1443031	912	
Feb. 23, 2008	22:49	02:20	1425558	913	
Feb. 24, 2008	02:20	05:52	1430697	914	
Feb. 24, 2008	05:52	07:20	473306	915	
$\Delta U = 0\,\text{V}$					
Feb. 24, 2008	07:22	10:45	1215721	916	
Feb. 24, 2008	10:45	13:56	1255503	917	
Feb. 24, 2008	13:57	18:00	1331698	918	
$\Delta U = 301\,\text{V}$					
Feb. 24, 2008	18:02	02:23	1638038	919	
Feb. 25, 2008	02:24	08:08	1241072	921	

Table 3.4: Table with all runs used for the electron proton spin-flip cross-section measurement. Together with the start and stop time, the run number and the number of the stored events are given. It is indicated which detuning voltage ΔU was used during for each file.

Chapter 4

Data Analysis

The goal of the analysis is to determine the ratio $\frac{P_E}{P_0}$ from eqn. (3.3) and it's systematical and statistical error. The data proton deuteron scattering at a beam energy of $T_p = 49.3\,\text{MeV}$. It is logically split into two different types.

The first type, consists of identified proton deuteron elastic scattered events, while the other type takes care of all other events, including both not identified elastic scattered events and break-up events. With the beam energy of $T_p = 49.3\,\text{MeV}$ the data is taken below pion-production threshold, so an identified deuteron ensures, that elastic scattering took place. For these events the analyzing powers are well known, and it is possible to calculate the beam polarization. The double ratio method is used, which minimizes systematic effects.

For the second sample the analyzing powers are unknown. Since only the ratio of the polarizations is of interest, they contain information on the depolarization cross-section, as the ratio of asymmetries is identical to the ratio of polarizations:

$$\frac{P_E}{P_0} = \frac{\epsilon_E \cdot A_y}{\epsilon_0 \cdot A_y} = \frac{\epsilon_E}{\epsilon_0}, \tag{4.1}$$

with the count-rate-asymmetry ϵ and the analyzing power A_y. This sample still provides additional information about the spin-flip cross section, without determining the absolute beam polarization.

The structure of this chapter follows the steps done in the analysis. Section 4.1 shows the detector stability, sec. 4.2 shows the reaction independent track reconstruction, sec. 4.3 describes the cuts used for the different sample selections, sec. 4.4 shows how the polarization (count-rate-asymmetry) is determined, while sec. 4.5 adds an error estimation.

4.1   Detector Stability

As a first step of the analysis the data has to be checked for stable conditions. This section shows that for the used data the detector system was working properly. This includes constant pedestal, and constant geometrical acceptance. Dead-time effects are totally
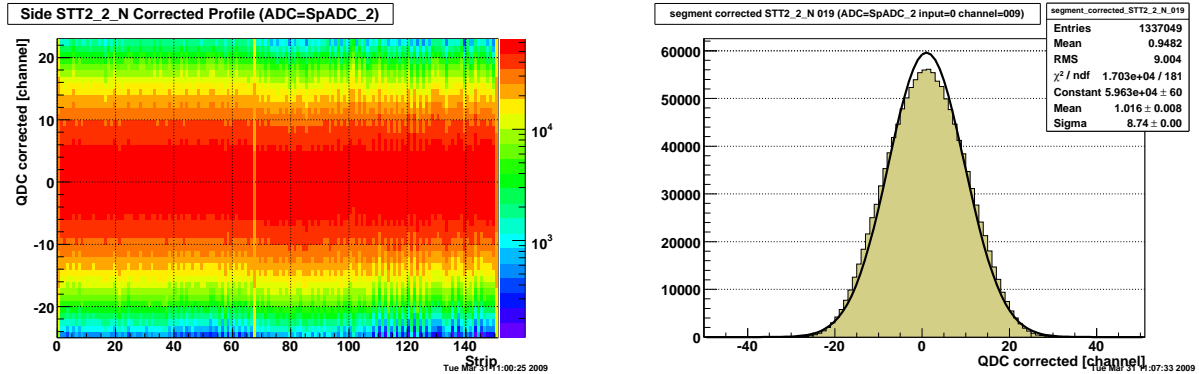
Figure 4.1: This histogram shows a typical common mode corrected pedestal line for STT2_1_P. The right histogram shows the pedestal peak for segment 19 with a width in the order of 10 channels of the 12bit ADC.

negligible as the total system has a dead-time of $< 100\,\mu s$ and the count-rate was always well below 500 /s.

4.1.1   Pedestal

Without any input signal on the detector, the detection system gives back a value > 0. This so-called pedestal has two contributions: A constant offset and a widening of the peak due to noise. The correction is done in two steps. The first corrects the constant offset, while the second one minimizes the noise effects.

In order to correct the constant offset, roughly 10000 events are analyzed of each data file. For each segment all events without own trigger signal (this ensures that no energy loss in this segment is detected in this event) are taken and the average of these QDC values is calculated. This offset, the so-called pedestal value, has to be calculated for all segments and all individual values are saved in a parameter file. In the further analysis the individual pedestal value of a segment is substracted.

Noise which comes randomly to the detector can not be corrected. But there is a part of the noise, which is equal on all segments of one detector side. It may be caused e.g. by tiny changes in bias voltages. This so-called common mode is corrected in the second step: For each event the average of all pedestal-corrected QDC outputs from one detector side is subtracted in addition.

For a stable detector acceptance, the pedestal values have to be stable. This is checked by calculating the pedestal from the first 10000 events of a data file and verifying, that the pedestal peak does not change more than its peak width during the complete data file.

Figure 4.1 shows a typical pedestal spectrum. On the left side an enlargement into the energy deposits for each segment of the detector side STT2_1_P is shown. On the right side the common-mode corrected QCD-spectrum (pedestal peak) of segment STT2_2_N 019 is given.

4.1.2 Geometrical Acceptance

A polarimeter has to provide an unvarying geometrical acceptance and an unvarying efficiency in order to eliminate fake asymmetries. There are different sources of fake asymmetries:

- A moving beam-target overlap,

- a moving detection setup (vibrations),

- changing energy response and trigger conditions, and

- loss of segments.

The first item will be discussed in sec. 4.5.3, the second and third ones can immediately be excluded: There are vibrations of the detection system due to the turbo-pumps for the vacuum system and due to the flow of the cooling liquid, but they obviously lead to a negligibly small movement compared with the detector pitch. Additionally, the temperature of the detectors and the front-end electronic boards were controlled and stable to $\Delta T < 1\,\mathrm{K}$.

To exclude a changing geometrical acceptance due to loss of segments, all segments, which are not working in at least one run, are taken out of the complete analysis.

Here especially the detector STT1_1 has to be mentioned. Supposedly, due to a direct hit of the COSY proton beam a complete region of this detector has been destroyed (fig. 4.2). This leads to a big discrepancy in the left-right asymmetry of the detection setup. The following analysis shows, that this effect does not influence the result for the polarization measurement.

4.2 Track Reconstruction

Independent of any constraints from the reaction, tracks of particles passing through the silicon tracking telescopes are reconstructed. As a first step, all hits in one silicon detector have to be reconstructed. A hit consists of the position and energy-deposit from each detector side. For each side all segments with a QDC value above threshold ($8\,\sigma$ above its pedestal peak) are identified. If there are two or more segments next to each other with a QDC value above threshold, the energy is added up and only one hit is generated. For all hits on one detector side, a corresponding hit on the other side is searched. Their energy must be identical, within some limits. Here the limit was set to infinity, as the p-doped sides do not provide a proper energy information. In order to exclude wrong combinations of hits for the two detector sides, only events with one hit per detector side ($\gtrsim 99\,\%$ of statistics) have been analyzed.

Combining hits in the first layer with hits in the second layer of one STT, gives a reconstructed track. This track includes position and energy information in each layer, and derived values for the scattering and azimuthal angle.
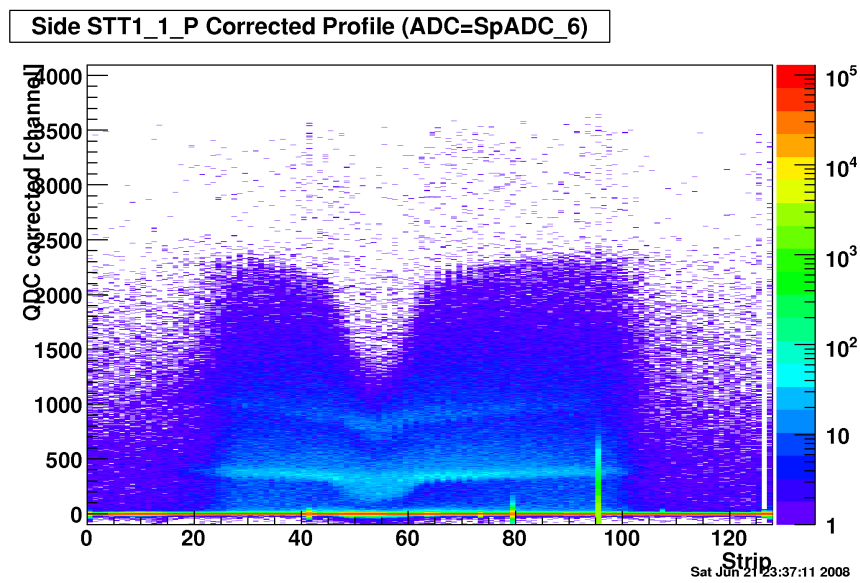
Figure 4.2: This histogram shows the pedestal corrected QDC values for each strip of the p-doped side of STT1_1 (left STT, 1st layer). In the region between strip number 37-66 the high energy response is missing. Additionally a clear broadening of the pedestal is visible. As no tracks can be reconstructed from this region of the detector, these strips are removed from the analysis.

In each event, there might be zero reconstructed, one reconstructed or two (in each STT one) reconstructed tracks. At this stage the analysis does not give any information on the type of particle or whether a proton deuteron break-up or elastic event was detected.

4.3 Event Selection

To measure the absolute polarization, it is necessary to reconstruct proton-deuteron elastic events with low background. As a first step, the stopped deuterons are identified. The energy loss of particles in matter is described by the Bethe-Bloch-formula eqn. 4.2 and depends on the mass of the slowed-down particles.

$$-\frac{dE}{dx} = \frac{4\pi n z^2}{m_e v^2} \cdot \left(\frac{e^2}{4\pi\epsilon_0}\right)^2 \ln\left(\frac{2m_e v^2}{I}\right), \tag{4.2}$$

is the Bethe-Bloch-formula. Here v is the velocity of the penetrating particle, ϵ_0 is the permittivity of free space, the electron mass m_e and some material related values: The electron density n, the atomic number z and the average ionization energy I. By this formula it is possible to distinguish with the detection system different particles. On a plot with the energy loss of the first layer *vs* the energy loss of the second layer, different particles populate different loci. Due to different inclination angles, the passing particle passes through more or less detector material. This effect, together with the finite energy resolution of the detector leads to a broadening of the loci. Figure 4.3 shows the described energy loss spectrum, both for the left and right detection system. Particles stopped in the
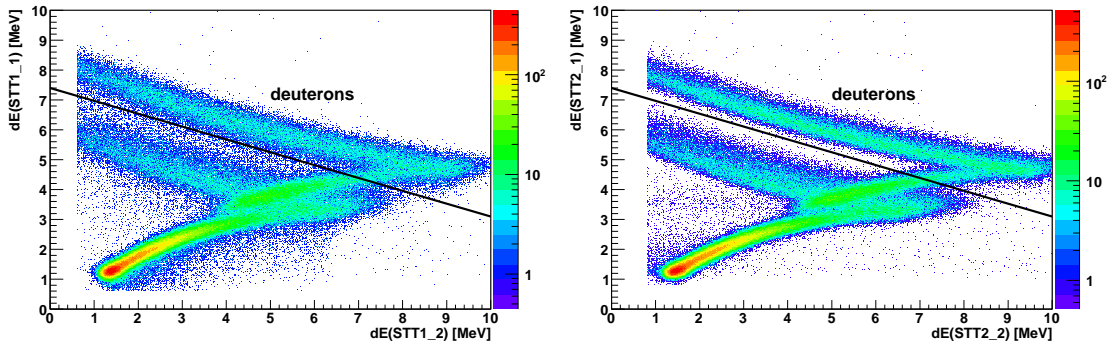
Figure 4.3: Energy loss in the first detector plane *vs* energy loss in the second detector plane for both telescopes separately. All particles above the line are identified as deuterons.

first layer do not cause any trigger and do not occur. With increasing energy they pass the first layer and generate a signal in the second layer. They have the highest energy loss in the first layer and only a low energy loss in the second. With increasing recoil energy, the

energy loss in the second layer increases, while the energy loss in the first layer decreases due to the $\frac{1}{v^2}$ dependenc of the energy loss (eqn. 4.2). As long as the particles are stopped in the second layer, their initial kinetic energy is the sum of two energy losses in layer one and two. At higher energies (roughly $10\,\text{MeV}$ for protons and $14\,\text{MeV}$ for deuterons) they pass through the second layer and produce a decreasing energy loss in the first two layers. The black lines indicate the used cuts. Above this line clearly identified deuterons are located. Most of them are stopped and some have just enough energy to penetrate both the first and second detection layers.

Below the line, there are additional deuterons. But these can not be identified with a single cut. So a chain of cuts is introduced. The main idea is to select events, with a deuteron in one STT and a proton in the other.

4.3.1   Kinematics of Proton-Deuteron Elastic Scattering

Before describing the cuts for the two particle events, the kinematics of proton-deuteron elastic scattering is shown. The data analysis is done in the laboratory frame, so all following variables are given in laboratory frame.

Proton-deuteron elastic reactions are two body reactions, and thus five independent parameters are needed to describe one event with known beam and target momentum. They are the three positions of the vertex X, Y and Z, which are prior known only within several millimeters from mechanical constraints. Additionally, the direction (two angles) of one particle is necessary. Here the scattering and azimuthal angles θ_d and ϕ_d from the deuteron are taken. The momentum of the proton is then fixed by the 4-momentum conservation.

In fig. 4.4 the energy *vs* scattering angles is plotted for both the proton and deuteron, while in fig. 4.5 the scattering angle of the proton is plotted *vs* the one of the deuteron. The geometrical acceptance of the detection system is indicated with lines. The region where
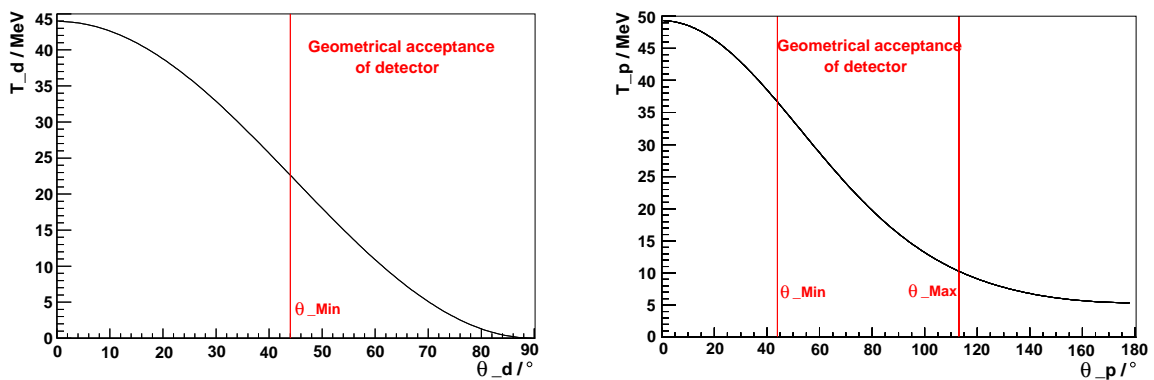

Figure 4.4: Left: Deuteron energy *vs* deuteron scattering angle. Right: Proton energy *vs* proton scattering angle. In both plots, the geometrical acceptance of the detection system is indicated.
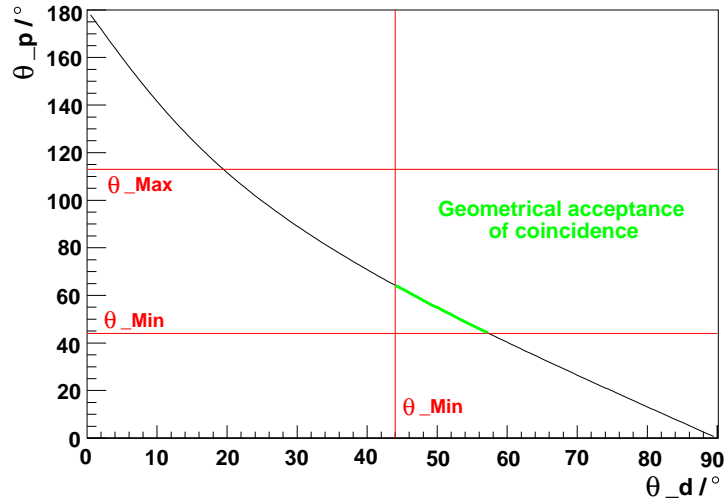
Figure 4.5: Deuteron scattering angle *vs* proton scattering angle. The geometrical acceptance of the detection system is indicated. The green line indicates the part of events were both proton and deuteron may be detected.

proton and deuteron may be detected in coincidence, is $44\,° < \theta_d < 57.3\,°$ corresponding to $64,2\,° > \Theta_p > 44\,°$. The kinetic energy ranges for deuteron and proton are: $12.7\,\text{MeV} < T_d < 22.4\,\text{MeV}$ and $36.6\,\text{MeV} > T_p > 22.4\,\text{MeV}$. This part of the recorded data, contains additional events, which are not identified with the single cut on deuterons shown in fig. 4.3.

4.3.2   Events with Proton Deuteron Coincidence

In order to reconstruct more proton-deuteron elastic events coincidences of a detected proton and deuteron are analyzed. As a first step, events with a candidate of a proton and deuteron from elastic events are selected. The used cuts are indicated in fig. 4.6. While the cut for deuterons takes as many deuterons as possible, the cut on protons selects mainly elastic scattered protons. These have in the coincidence region a high kinetic energy of more than $26\,\text{MeV}$ and therefore produce an energy loss of less than $4\,\text{MeV}$ in each detection layer.

For these candidates, the energy loss plot is shown in fig. 4.7.

The second step is the requested coincidence of a proton and a deuteron candidate, and additional cuts are following (fig. 4.8). The difference of the azimuthal angles $\Delta\phi = \phi_p - \phi_d = 180\,°$ is constant and a cut with $\Delta\phi = \pm\,7\,°$ around the peak is used. A second cut is on the scattering angles. Here the deuteron scattering angle is calculated from the measured proton scattering angle. The difference of this calculation to the measured value is plotted in the right histogram of fig. 4.8. A cut of $\Delta\theta = \pm 4\,°$ was used here.

For all reconstructed events, the deuterons are once again plotted in an energy loss histogram (fig. 4.9). The discontinuity in reconstructed deuterons is due to the two different methods. The coincidence method gives additional events, but with reduced efficiency.
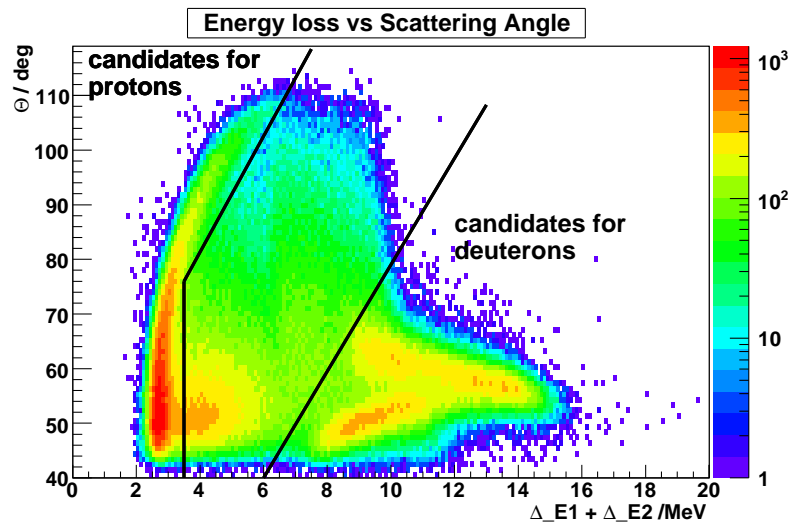
Figure 4.6: Scattering angle *vs* sum of energy loss in the first two layers. The particles left from the left line are candidates for elastically scattered protons, and the particles right from the right line are candidates for elastically scattered deuterons.

4.3.3   Minimum Bias Selection

A minimum bias selection is realized as a third way of selecting proton-deuteron elastic scattering events. In the energy loss plot, as it was used to identify single deuterons, the complete region for deuteron is selected. Additional to the clearly identified deuterons,
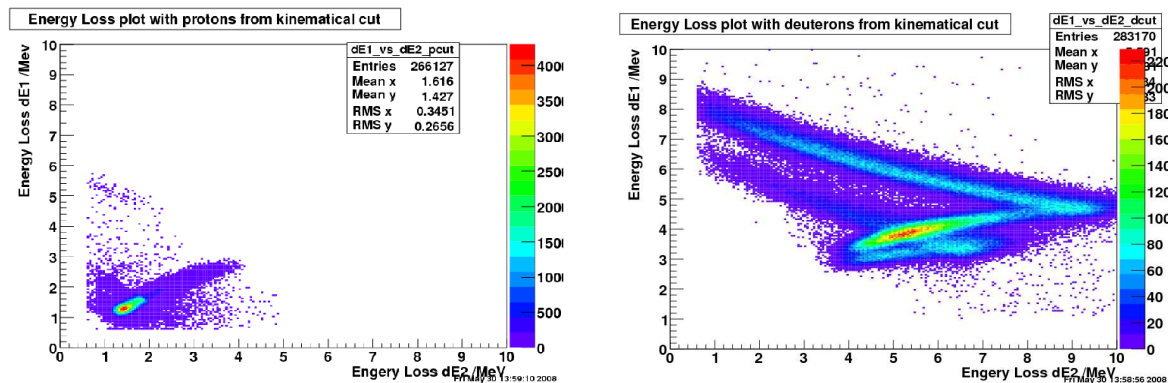
Figure 4.7: The particles from the cut in fig. 4.6 are plotted in the energy loss spectrum. Here one can see, that all deuterons are included, but with high background. High energy protons, mainly from proton-deuteron elastic scattering are shown in the left histogram.
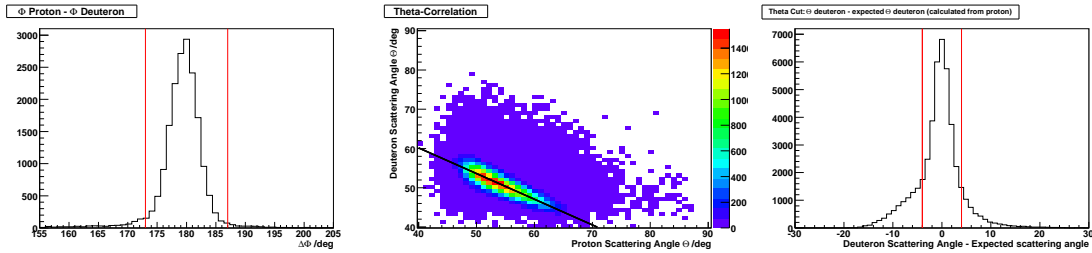
Figure 4.8: The left histogram shows the difference of the proton and deuteron polar angles. The middle histogram shows the deuteron scattering angle *vs* proton scattering angle. The line indicates the theoretical prediction. The right histogram shows the difference between the deuteron scattering angle and its prediction calculated from the proton scattering angle. The vertical lines show the used cuts.

which are mainly stopped in the second detection layer, deuterons with higher energies are selected as well. The cut region is indicated on the left histogram in fig. 4.10 by the solid lines. The dotted line gives shows the cut for the stopped deuterons. Additional a cut on the scattering angle is introduced: $\theta < 57°$ (right histogram in fig. 4.10). Deuterons with scattering angles $\theta_d > 55°$ have lower energies, are stopped in the second layer, and therefore are already identified as deuterons. The cut is set $2°$ higher, as this is the order of the smearing due to multiple scattering.

4.3.4 Additional events

If in an event no deuteron is found in the minimum bias cut and only one track is reconstructed, this is taken as additional events. These events include proton-deuteron elastic scattering, with the deuteron out of the detector acceptance, and proton-deuteron break-up events. For these events the analyzing powers are unknown, but the asymmetry of these events can also be used to determine the electron-proton spin-flip cross section.

4.3.5 Pre-analyzed Data

For the selected events the information, which are necessary for the further analysis, are stored. For each run four different files are produced - one for each selection. They contain the information of the reconstructed deuteron and of the reconstructed protons (if so) on an event-by-event basis. For each particle the reconstructed angles, energy deposits and the number of the fired segments are saved. Additional information about the beam polarization, whether the deuteron target was switched on, whether the stored beam experienced the electron target and the time-stamp of the event is appended.
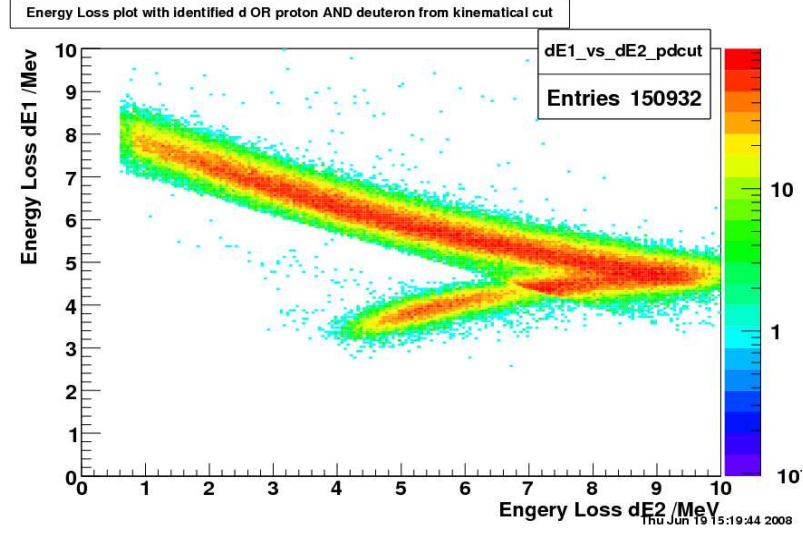
Figure 4.9: Energy loss spectra of all identified proton-deuteron elastic events. The step is due to the lower acceptance for the coincident events.

4.4   Polarization Determination

4.4.1   Double Ratio

Using the selected events, the beam polarization is deduced. The beam polarization leads to an azimuthal dependence of the differential cross section. It is:

$$\frac{d\sigma}{d\Omega}(\theta, \phi) = \frac{d\sigma_0}{d\Omega}(\theta) \cdot [1 + PA_y(\theta)\cos\phi], \tag{4.3}$$

with the unpolarized differential cross section $\frac{d\sigma_0}{d\Omega}$, the scattering angle θ, the azimuthal angle ϕ, the beam polarization P and the analyzing power A_y. Here the scattering angle θ is measured from the outgoing beam direction, and the azimuthal angle ϕ from the horizontal direction.

The actual number of counts recorded in a detector, $N(\theta, \phi)$, may be written as follows:

$$N(\theta, \phi) = n\, d_t\, \Delta t\, \Delta\Omega\, E\, \frac{d\sigma}{d\Omega}(\theta, \phi) \tag{4.4}$$

Here n is the number of particles incident on the target, d_t is the target area density, Δt the measurement time, $\Delta\Omega$ the solid angle subtended by the detector and E the detection efficiency. For the two detectors L and R (Left and Right) at $\phi = 0$ and $\phi = \pi$ eqn. 4.4 is:

$$N_{L\uparrow}(\theta, 0) \quad \equiv \quad L_\uparrow = n\, d_t\, \Delta t\, \Delta\Omega_L\, E_L\, \frac{d\sigma_0}{d\Omega}[1 + P\, A_y(\theta)] \tag{4.5}$$
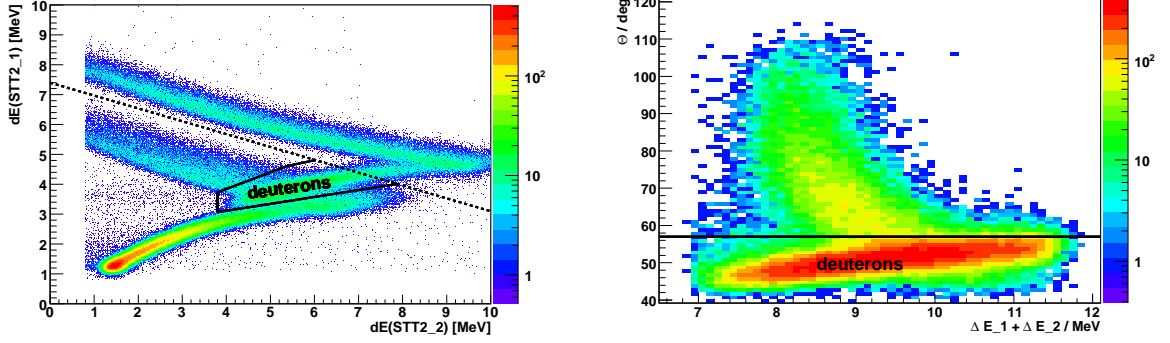
Figure 4.10: Left: This energy loss spectrum for STT2 (Right STT) indicates the minimum bias cuts, which are used to reconstruct deuterons. Right: The additional cut $\theta < 57\,^\circ$ strongly reduces the background from breakup protons.

$$N_{R\uparrow}(\theta, \pi) \quad \equiv \quad R_\uparrow = n\, d_t\, \Delta t\, \Delta\Omega_R\, E_R\, \frac{d\sigma_0}{d\Omega}\left[1 - P\, A_y(\theta)\right]. \tag{4.6}$$

And with a flipped beam polarization:

$$N_{L\downarrow}(\theta, 0) \quad \equiv \quad L_\downarrow = n'\, d'_t\, \Delta t'\, \Delta\Omega_L\, E_L\, \frac{d\sigma_0}{d\Omega}\left[1 - P\, A_y(\theta)\right] \tag{4.7}$$

$$N_{R\downarrow}(\theta, \pi) \quad \equiv \quad R_\downarrow = n'\, d'_t\, \Delta t'\, \Delta\Omega_R\, E_R\, \frac{d\sigma_0}{d\Omega}\left[1 + P\, A_y(\theta)\right], \tag{4.8}$$

where the primes are used to indicate that the integrated charge and the effective target thickness may not be the same for the two runs. Taking the geometric means

$$L \equiv \sqrt{L_\uparrow\, R_\downarrow} \quad = \quad \left[n\, n'\, d_t\, d'_t\, \Delta t\, \Delta t'\, \Omega_L\, \Omega_R\, E_L\, E_R\right]^{\frac{1}{2}} \frac{d\sigma_0}{d\Omega}\left[1 + P\, A_y(\theta)\right] \text{ and} \tag{4.9}$$

$$R \equiv \sqrt{R_\uparrow\, L_\downarrow} \quad = \quad \left[n\, n'\, d_t\, d'_t\, \Delta t\, \Delta t'\, \Omega_L\, \Omega_R\, E_L\, E_R\right]^{\frac{1}{2}} \frac{d\sigma_0}{d\Omega}\left[1 - P\, A_y(\theta)\right], \tag{4.10}$$

the solid angle subtended by the detector $\Delta\Omega$, the detection efficiency E and the integrated luminosity $n \cdot d_t \cdot \Delta t$ cancel in the fraction

$$\delta = \frac{L}{R} = \frac{1 + P A_y(\theta)}{1 - P A_y(\theta)}. \tag{4.11}$$

Solving for $P\, A_y$ one concludes that the left-right asymmetry ϵ is:

$$\epsilon = \frac{\delta - 1}{\delta + 1} = P\, A_y(\theta). \tag{4.12}$$

The statistical error of the asymmetry ϵ follows error propagation:

$$\Delta\epsilon = \frac{2}{(L + R)^2} \cdot \sqrt{R^2 \Delta L^2 + L^2 \Delta R^2}, \tag{4.13}$$

with $\Delta L = 0.5\sqrt{L_\uparrow + R_\downarrow}$ and $\Delta R = 0.5\sqrt{R_\uparrow + L_\downarrow}$.

4.4.2   Beam Polarization

Within the analysis the previously described double ratio method is applied. The analyzing power is taken from [Kin77]. In fig. 4.11 the used 4th order polynomial is displayed together with the original data points.
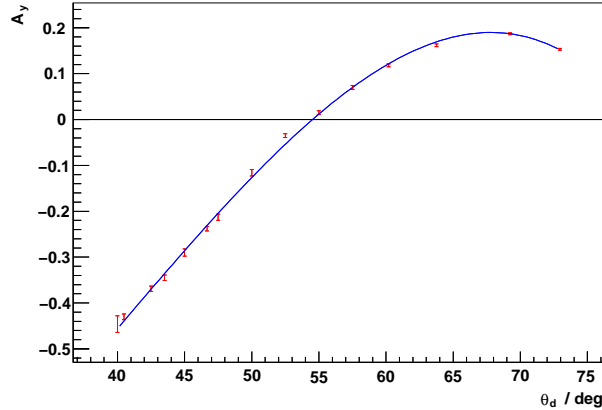
Figure 4.11: The analyzing power from [Kin77] *vs* the scattering angle of the deuteron in the laboratory frame. The dotted line gives a 4th order polynomial fit to the data. This fit is used for the analyzing power in the analysis.

As the analyzing power is a function of the scattering angle Θ, the selected events have to be binned in Θ. Here $3\,^\circ$ bins in the deuteron scattering angle θ_d are chosen. The binning is in the same order as the angular straggling in the first layer. In a good approximation the analyzing power is constant over each bin, but the large geometrical acceptance in the azimuthal angle $\phi = 0\,^\circ (180\,^\circ) \pm 28\,^\circ$ requires to be corrected.

This done by modifying the simple eqn. 4.12 and finally the beam polarization is:

$$P = \frac{\epsilon}{A_y \cdot \, <\cos(\phi)>}. \tag{4.14}$$

4.5   Systematic Errors

Systematic errors in the electron proton spin flip cross section measurement can originate from different sources. In the following, the momentum spread of the stored proton beam, the rise time of the electron cooler voltage, fake asymmetries from a moving beam target overlap and errors caused by different polarizations for up and down polarized beams are discussed.

4.5.1   Spread of Proton Energy in Electron Frame

The momentum spread of the proton beam was measured as a function of the beam intensity. The result is shown in fig. 4.12. During the measurement of the electron proton spin

flip cross section, the maximum beam intensity was $< 2 \cdot 10^8$ stored particles. From this a maximum momentum spread of the proton beam of $\frac{\Delta p}{p} < 3 \cdot 10^{-5}$ can be deduced.
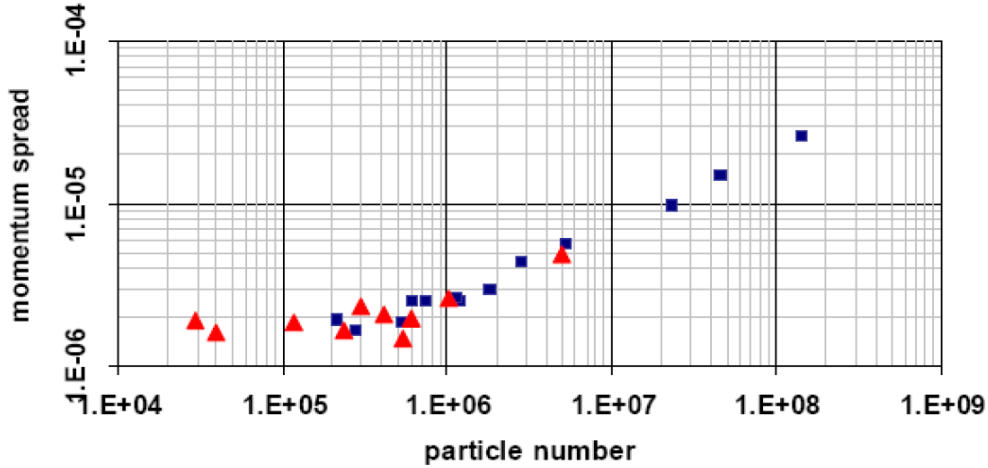
Figure 4.12: Momentum spread of the proton beam *vs* beam intensity. The measurement shows a momentum spread of $\frac{\Delta p}{p} < 3 \cdot 10^{-5}$ for beam intensities less than $2 \cdot 10^8$ stored protons.

By $\frac{\Delta p}{p} = \frac{\gamma}{\gamma+1} \cdot \frac{\Delta T}{T}$ the spread of the kinetic energy in the laboratory frame is $< 2.88 \, \text{keV}$ and $< 4 \, \text{eV}$ in electron frame. Thus it is completely negligible compared with the kinetic energy of the protons in the electron frame (fig. 4.13).

4.5.2 Electron Cooler Voltage

The acceleration voltage for the electrons can not be changed spontaneously. This leads to a time with changing electron voltage. Additionally a difference in the rise and decrease time would lead to an offset in time with electron target switched on. To judge this effects the rise and decrease time of the voltage was measured with an oscilloscope. From fig. 4.14 a maximum rise and decrease time of $< 0.1 \, \text{s}$ can be evaluated. All used voltage jumps were smaller than the here shown jump of $1000 \, \text{V}$ so their effects are smaller, too.

The fraction of the time with changing electron velocity compared with the time with electron target is smaller than $\frac{0.2 \, \text{s}}{5 \, \text{s}}$ and no difference in the rise and decrease time is visible. Both effects lead to only negligible small systematic errors.

4.5.3 Fake Asymmetry from Moving Beam Target Overlap

A change of the beam-target overlap leads to a change of the measured asymmetry. A systematic shift of the beam-target overlap between two different spin states, is identical to a different geometrical acceptance and cancels in first order by the used double ratio method. As only fractions of polarizations contribute in the cross section evaluation eqn. (3.3) a systematic shift of the beam-target overlap between cycles with and without
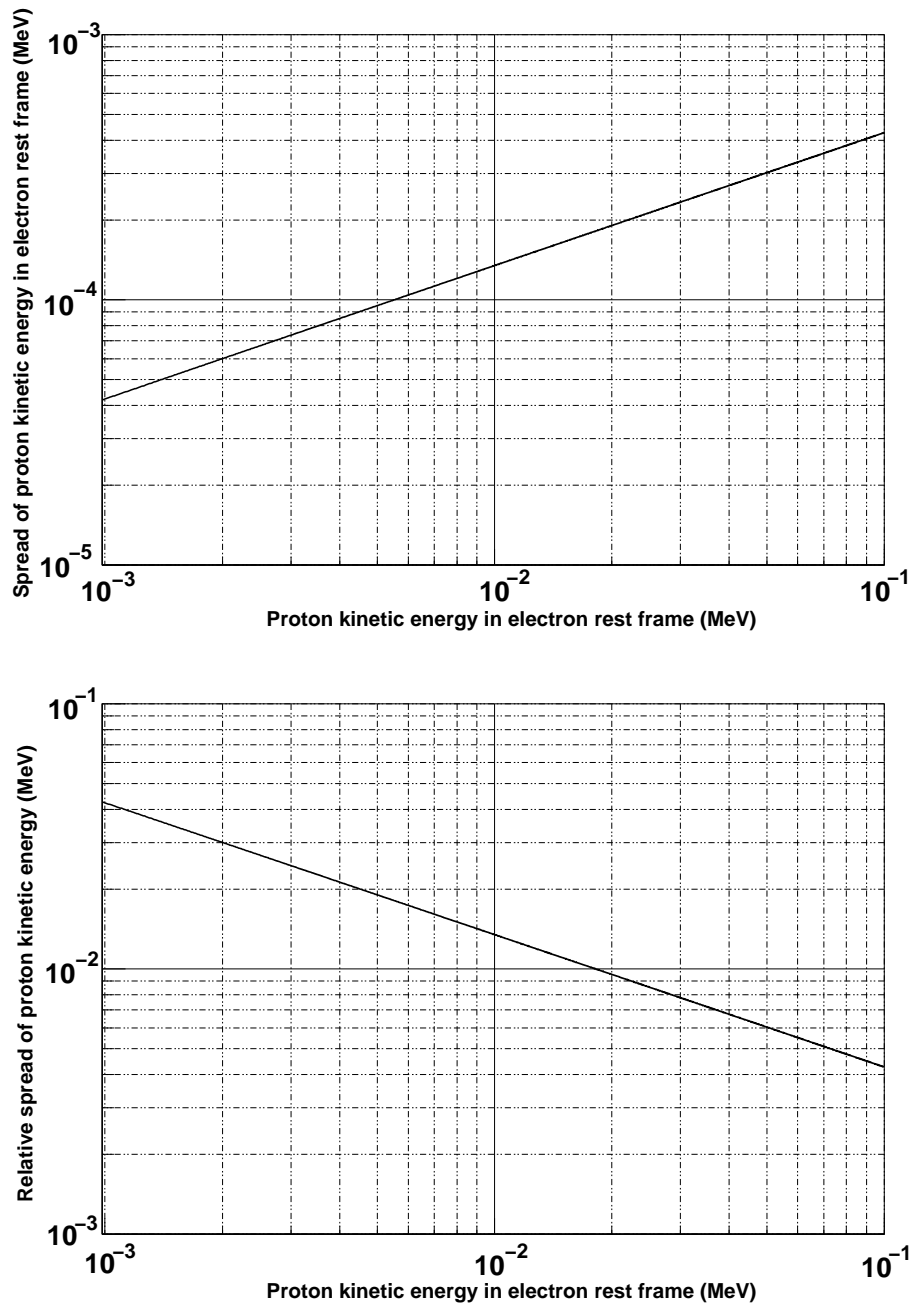
Figure 4.13: The two figures show the spread of the proton kinetic energy in the electron rest frame. In the upper plot absolute values are given and the plot below shows the relative values.

electron target cancels, too. Only a different shift of the beam-target overlap for polarization up/down combined with a shift for cycles with and without electron target, contribute
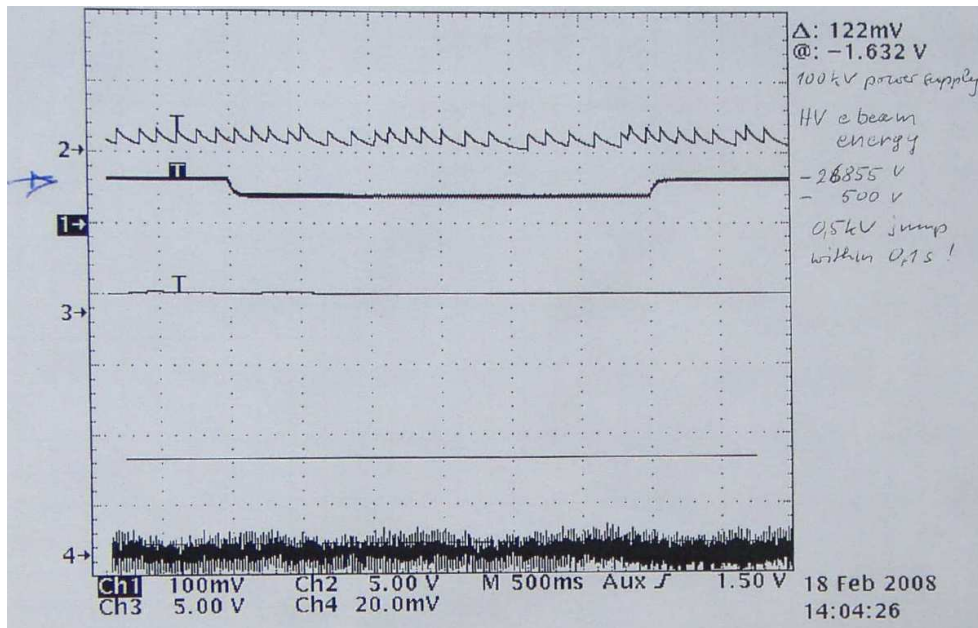
Figure 4.14: The acceleration voltage of the electron cooler was measured with an oscilloscope. Here the rise and decrease time for an voltage jump of 1000 V is shown. Within less than 0.1 s the final voltage is reached. For smaller voltage jumps the rise time is even smaller.

to a systematic error.

For each of this four combinations, and for each detune voltage the beam target overlap was computed. For that purpose proton-deuteron elastic events with both a reconstructed proton *and* deuteron was used. There are two tracks, which made signals in two layers of the silicon detectors and each detector gives the x- and y- coordinate. In total 8 parameters are measured. Only 5 parameters are necessary to describe proton deuteron elastic scattering at fixed energy. Here the primary vertex (X, Y, Z) and the two deuteron angles (θ and ϕ) were used. By fitting the vertex on an event-by-event basis is deduced. In fig. 4.15 the time dependence of the vertex position is shown for the X and Y coordinates. No shift of the vertex occurred.

In fig. 4.16 the X and Y coordinates of all reconstructed vertices are plotted and fitted with a Gaussian distribution. Here one typical data set with electron target switch on, beam polarization state down and one relative velocity is shown for illustration. As the used deuterium cluster target is much wider, the proton beam distribution becomes visible. The results for all other data is given in tab. 4.1. The result is that no difference in the reconstructed vertices or beam spread could be detected. A systematic effect of a systematic shift of the vertex between different cycles or polarizations is therefore excluded.
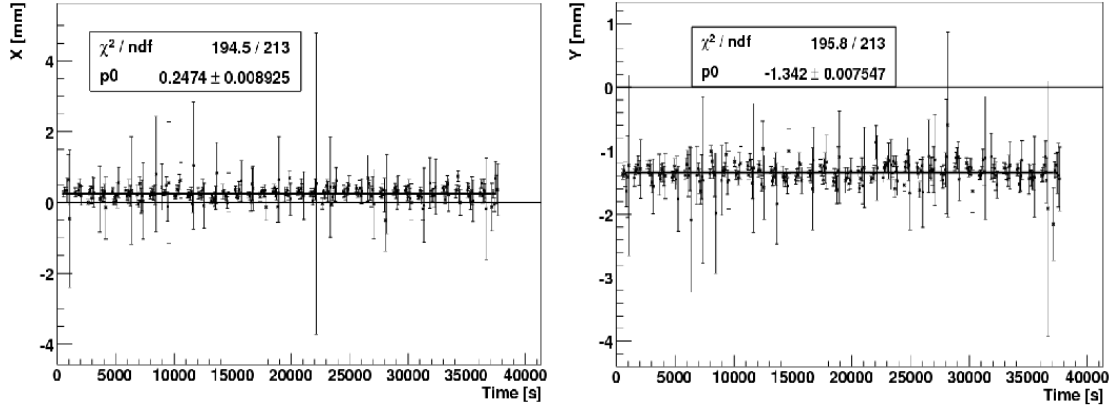
Figure 4.15: Left (Right): X (Y) position of the vertex *vs* time. Complete statistics of the $\Delta U = 0\,\mathrm{V}$ data is shown.
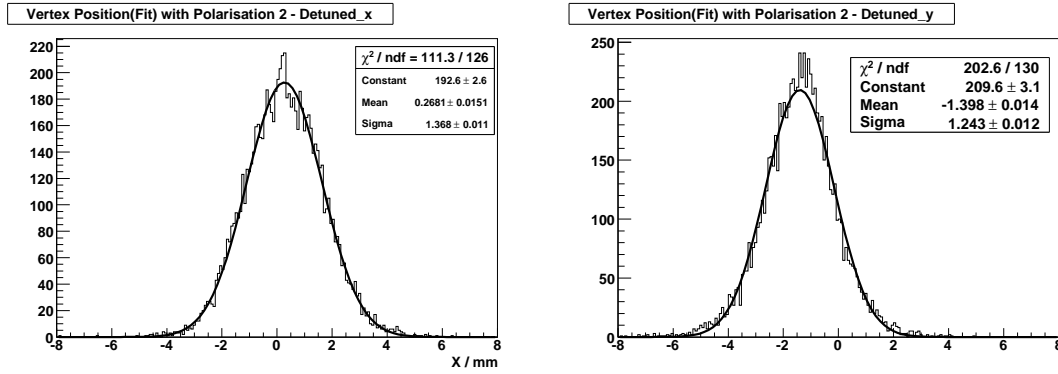
Figure 4.16: Left (Right): X (Y) position of the vertex. Only data from cycles with electron target switch on, beam polarization state down and one relative velocity is shown. The gaussian distribution represents the proton beam, as the cluster target is much wider.

4.5.4   Errors from Polarization-Analysis

The used double ratio method assumes identical polarizations of polarization up and down samples. This assumption is tested by two methods. Firstly, the low energy polarimeter, placed in the injection beamline gives a beam polarization for up (down) states of 0.80 ± 0.02 (0.84 ± 0.02) which are compatible to each other. Secondly, the polarizations can be calculated using the silicon detectors. To do so, the double ratio method is applied with up (down) polarized and unpolarized data. The numbers are given in sec. 5.1.1.

	Voltage jump 0 V					
	with electron target			without electron target		
	up	down	unpolarized	up	down	unpolarized
x	0.262 ± 0.014	0.238 ± 0.014	0.268 ± 0.015	0.235 ± 0.015	0.231 ± 0.016	0.271 ± 0.015
σ_x	1.342 ± 0.010	1.364 ± 0.011	1.368 ± 0.011	1.361 ± 0.011	1.387 ± 0.012	1.363 ± 0.011
y	-1.354 ± 0.013	-1.351 ± 0.014	-1.389 ± 0.014	-1.322 ± 0.013	-1.336 ± 0.014	-1.343 ± 0.013
σ_y	1.239 ± 0.011	1.231 ± 0.011	1.243 ± 0.012	1.237 ± 0.011	1.238 ± 0.012	1.246 ± 0.011
	Voltage jump 246 V					
	with electron target			without electron target		
	up	down	unpolarized	up	down	unpolarized
x	0.257 ± 0.019	0.256 ± 0.020	0.256 ± 0.020	0.320 ± 0.026	0.240 ± 0.032	0.208 ± 0.028
σ_x	1.390 ± 0.018	1.418 ± 0.015	1.410 ± 0.019	1.331 ± 0.019	1.369 ± 0.025	1.404 ± 0.022
y	-1.388 ± 0.017	-1.332 ± 0.017	-1.356 ± 0.017	-1.435 ± 0.023	-1.297 ± 0.029	-1.453 ± 0.024
σ_y	1.233 ± 0.014	1.233 ± 0.014	1.215 ± 0.015	1.215 ± 0.021	1.250 ± 0.026	1.225 ± 0.020
	Voltage jump 301 V					
	with electron target			without electron target		
	up	down	unpolarized	up	down	unpolarized
x	0.247 ± 0.018	0.269 ± 0.020	0.263 ± 0.017	0.253 ± 0.019	0.227 ± 0.020	0.247 ± 0.019
σ_x	1.432 ± 0.014	1.443 ± 0.015	1.433 ± 0.012	1.442 ± 0.015	1.433 ± 0.016	1.431 ± 0.014
y	-1.380 ± 0.020	-1.414 ± 0.019	-1.384 ± 0.017	-1.394 ± 0.019	-1.404 ± 0.020	-1.362 ± 0.019
σ_y	1.438 ± 0.016	1.435 ± 0.016	1.399 ± 0.014	1.380 ± 0.010	1.430 ± 0.020	1.409 ± 0.015
	Voltage jump 348 V					
	with electron target			without electron target		
	up	down	unpolarized	up	down	unpolarized
x	0.202 ± 0.013	0.222 ± 0.014	0.187 ± 0.014	0.189 ± 0.014	0.201 ± 0.016	0.235 ± 0.015
σ_x	1.396 ± 0.010	1.378 ± 0.010	1.392 ± 0.010	1.370 ± 0.010	1.370 ± 0.010	1.385 ± 0.011
y	-1.317 ± 0.012	-1.287 ± 0.012	-1.308 ± 0.012	-1.310 ± 0.010	-1.303 ± 0.014	-1.306 ± 0.014
σ_y	1.238 ± 0.010	1.235 ± 0.011	1.252 ± 0.010	1.251 ± 0.011	1.253 ± 0.012	1.240 ± 0.010
	Voltage jump 426 V					
	with electron target			without electron target		
	up	down	unpolarized	up	down	unpolarized
x	0.222 ± 0.013	0.236 ± 0.012	0.253 ± 0.012	0.275 ± 0.013	0.256 ± 0.013	0.269 ± 0.012
σ_x	1.385 ± 0.009	1.404 ± 0.009	1.415 ± 0.009	1.399 ± 0.010	1.394 ± 0.009	1.369 ± 0.009
y	-1.361 ± 0.011	-1.350 ± 0.010	-1.335 ± 0.011	-1.362 ± 0.012	-1.335 ± 0.011	-1.329 ± 0.011
σ_y	1.267 ± 0.010	1.284 ± 0.010	1.289 ± 0.009	1.287 ± 0.010	1.269 ± 0.010	1.274 ± 0.009
	Voltage jump -426 V					
	with electron target			without electron target		
	up	down	unpolarized	up	down	unpolarized
x	0.240 ± 0.012	0.204 ± 0.013	0.259 ± 0.013	0.252 ± 0.013	0.228 ± 0.013	0.273 ± 0.013
σ_x	1.424 ± 0.009	1.416 ± 0.010	1.426 ± 0.010	1.433 ± 0.010	1.399 ± 0.010	1.410 ± 0.010
y	-1.343 ± 0.011	-1.323 ± 0.012	-1.335 ± 0.013	-1.337 ± 0.012	-1.318 ± 0.012	-1.316 ± 0.012
σ_y	1.342 ± 0.010	1.318 ± 0.010	1.349 ± 0.011	1.324 ± 0.010	1.320 ± 0.010	1.304 ± 0.010

Table 4.1: X and Y coordinate of vertex position in mm. All values, including the variance are from a Gaussian fit. No significant shift of the beam target overlap is observed within the statistical uncertainties of the vertex positions.

Chapter 5

Results

In the previous chapter the analysis of the data is described. There are different samples of data which can be divided into two main groups. The first one deals with identified proton-deuteron elastic events, while the other sample consists of a mixture of proton-deuteron elastic and proton-deuteron break-up events. In sec. 5.1 the results for the beam polarization are presented. We will see, that the result for clearly identified deuterons and for coincident events are consistent with each other and do not depend on the symmetrical geometrical acceptance of the detection setup. The minimum bias selection on the other hand exhibits a higher background from non-elastic events and is therefore not used for the polarization determination. In sec. 5.2 the minimum bias and the additional one track sample is used to deduce the ratio of beam polarizations with and without electron target. Finally, in sec. 5.3, a likelihood method is described. By this the data-points for the six different detuning voltages are combined and an upper limit for the spin flip cross-section is obtained.

5.1   Polarization from Proton Deuteron Elastic Scattering

There are three different samples of identified elastic events. The first one are the clearly identified deuterons "D". The second disjunct sample is the coincidence sample "PD". The third sample "MB" is from the minimum bias and includes both sample "D" and "PD". Additionally a sample "D + PD" and a sample "Sym" are introduced. While "D + PD" adds the samples "P" and "D", "Sym" is the fraction of "D + PD" were the geometrical acceptance of the right detection system is cut to the reduced acceptance of the left fraction (sec. 4.1).

For all of these samples the polarization is calculated for the cycles with and without electron target separately. In the following, the cycles with electron target of the "D + PD" sample is shown to illustrate the method.

The selected events are sorted into bins covering $\theta_n \pm 1.5°$, where θ is the laboratory deuteron scattering angle and n is the bin number. This is done separately for the left

and the right detector and for runs with up or down beam polarization ($\uparrow$, $\downarrow$), resulting in the four yields $Y_{L\uparrow}(n), Y_{R\downarrow}(n), Y_{R\uparrow}(n), Y_{L\downarrow}(n)$. Making use of the double ratio method described in sec. 4.4, the asymmetry for each angle bin

$$\epsilon_n = \frac{1}{\langle cos\phi \rangle} \frac{\delta_n - 1}{\delta_n + 1},$$ (5.1)

where

$$\delta_n = \sqrt{\frac{Y_{L\uparrow}(n) \cdot Y_{R\downarrow}(n)}{Y_{L\downarrow}(n) \cdot Y_{R\uparrow}(n)}}$$ (5.2)

is calculated.

The average $\langle cos\phi \rangle$ over the azimuthal coverage of the detector takes into account the dependence of the analyzing power on azimuth. Asymmetries obtained during a typical run are shown in fig. 5.1. The solid curve results from a polynomial fit to the known analyzing power (sec. 4.4.2), folded with the width of the angle bins, and scaled to fit the data in the figure.

Figure 5.1: The asymmetry ϵ_n with its statistical errors *vs* the deuteron scattering angle in laboratory θ observed during the run with $\Delta U = 246\,\mathrm{V}$. The horizontal bars indicate the bin width of $3°$. The curve is deduced from the known analyzing power scaled to the measured polarization [Kin77].

For each angle bin the analyzing power $\overline{A}_{y,n}$ that represents the data from [Kin77] is calculated, using the polynomial fit and the measured θ for all events in that bin. Each bin then yields the value $\epsilon / \overline{A}_{y,n}$ for the beam polarization. Taking the weighted average for all bins, one arrives at the overall beam polarization (fig. 5.2). As this procedure is carried out separately for cycles with and without electron target, the result is the respective polarizations P_E and P_0. The runs with $\Delta U = 426\,\mathrm{V}$ are used to check, whether the polarization result is independent on the used sample and on the asymmetric detection
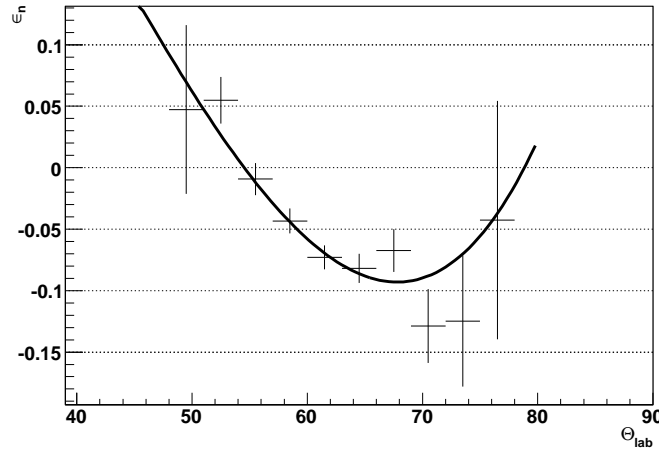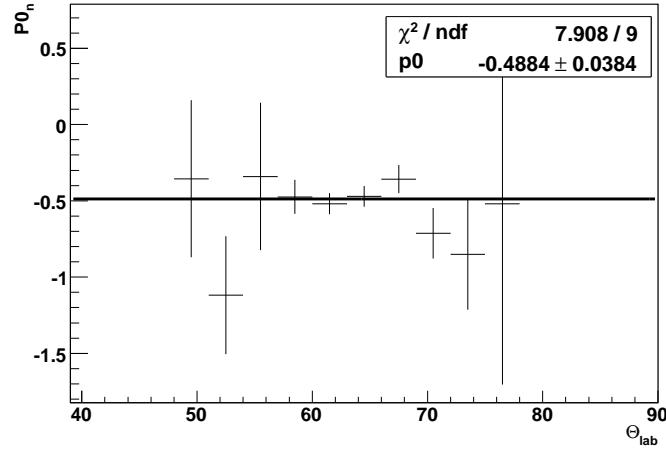
Figure 5.2: The polarization $P0_n$ with its statistical errors *vs* the deuteron scattering angle in laboratory θ observed during the run with $\Delta U = 246\,$V. The curve indicates the average polarization.

setup. In tab. 5.1 the beam polarizations P_E and P_0 are deduced from the different samples. All except the "MB" sample give identical results. The "MB" sample has the additional problem, that the analyzing power does not fit well to the measured asymmetries and gives a χ^2/ndf close to 11. This behavior can be explained by the background from non-elastic events in this sample. The other samples ("D+PD", "Sym" and "D") yield within error the same polarizations, which is a strong indication, that the geometrical acceptance drops out in the double ratio method as expected and that no significant background is contained in any of these samples. As a result the polarization for all other runs can be deduced from the "PD" sample.

Sample	P_E	P_0
MB	0.525 ± 0.014	0.510 ± 0.014
D+PD	0.486 ± 0.016	0.474 ± 0.016
Sym	0.487 ± 0.017	0.475 ± 0.017
D	0.482 ± 0.016	0.468 ± 0.016

Table 5.1: The beam polarization with and without electron target from different data selections. All except the minimum bias sample ("MB") give identical results.

In tab. 5.2 the polarizations for all ΔU and their ratio $R = P_E\,/\,P_0$ are given. For each ΔU the ratio R is compatible with 1, so no depolarization is measured. Figure 5.3 gives the ratio R *vs* the relative velocity. The vertical bars indicate statistical errors, while the horizontal bars indicate the range $\Delta\overline{u}$ of velocities that contribute to the measurement.

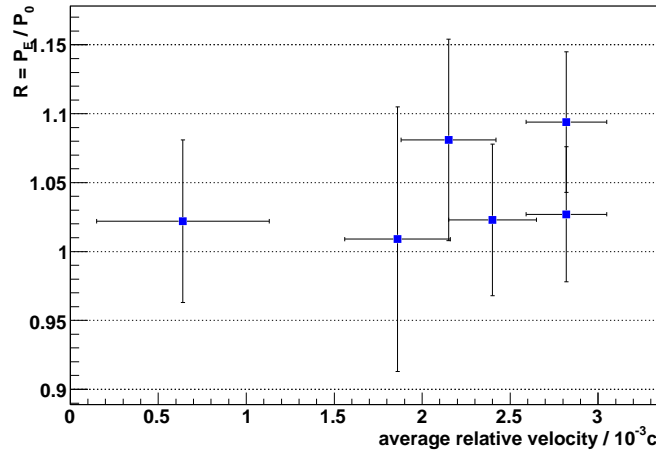| $\Delta U/$ V	P_E	P_0	R
0	0.529 ± 0.020	0.518 ± 0.023	1.022 ± 0.059
246	0.493 ± 0.026	0.488 ± 0.038	1.009 ± 0.096
301	0.534 ± 0.023	0.494 ± 0.025	1.081 ± 0.073
348	0.513 ± 0.018	0.501 ± 0.021	1.023 ± 0.055
426	0.487 ± 0.016	0.474 ± 0.016	1.027 ± 0.049
-426	0.532 ± 0.017	0.487 ± 0.017	1.094 ± 0.051

Table 5.2: Beam polarizations and their ratios for the different ΔU.

Figure 5.3: Ratio of the beam polarization with and without electron beam during the "interaction" part of the cycle as a function of the average relative velocity $\overline{v}$. The horizontal bars indicate the range $\Delta \overline{v}$ of velocities that contribute to the measurement. Here only data from clearly identified pd elastic events are taken into account.

5.1.1   Polarization of $\uparrow$ and $\downarrow$ Spin States

By combining data from the unpolarized spin state with data from $\uparrow$ and $\downarrow$ spin states, the double ratio method provides access to the two beam polarizations of the $\uparrow$ and $\downarrow$ spin states individually. In order to get statistical independent values, the unpolarized data set was dedived into two parts and only one part is used with each spin state.

The values of the polarizations and their ratios for the different data samples are given in tab. 5.3. The weighted average of the ratio R_P 0.995 ± 0.042 is compatible with 1 and no indication of different values is observed. Additionally, errors in the polarization due to different values for $\uparrow$ and $\downarrow$ polarizations occur identical for P_E and P_0, and cancel in the ratio $R = \frac{P_E}{P_0}$.

Data Sample	P	ΔP	R_P	ΔR_P
0 keV				
P_{up}	0.481	0.037	-0.847	0.085
P_{down}	-0.568	0.037		
1 keV				
P_{up}	0.639	0.063	-1.408	0.205
P_{down}	-0.454	0.049		
1.5 keV				
P_{up}	0.497	0.046	-0.829	0.098
P_{down}	-0.599	0.043		
2 keV				
P_{up}	0.514	0.036	-1.044	0.100
P_{down}	-0.492	0.033		
3 keV				
P_{up}	0.518	0.032	-1.155	0.107
P_{down}	-0.449	0.031		
-3 keV				
P_{up}	0.537	0.031	-1.067	0.089
P_{down}	-0.504	0.030		

Table 5.3: The beam polarization was deduced for the beam spin states ↑ and ↓ individually. The values for the six different data samples are given.

5.2   Asymmetry detection

Two disjunct samples of data are handled without knowing the analyzing power precisely. The one track sample ("OT") and the minimum bias ("MB") sample. As described in sec. 5.1 the data from the "MB" sample contain too much background to fit to the known analyzing power of proton deuteron elastic scattering. By comparing the asymmetries for cycles with and without electron target for these two samples independently, additional information about the electron proton spin flip cross-section can be achieved. As a first step the asymmetry is plotted identical as for the events with known analyzing power. A 3rd order polynomial was fitted to the measured asymmetry of cycles without electron target and a detuning voltage of 426 V. These asymmetries and their fit is shown in fig. 5.4. The resulting functions are
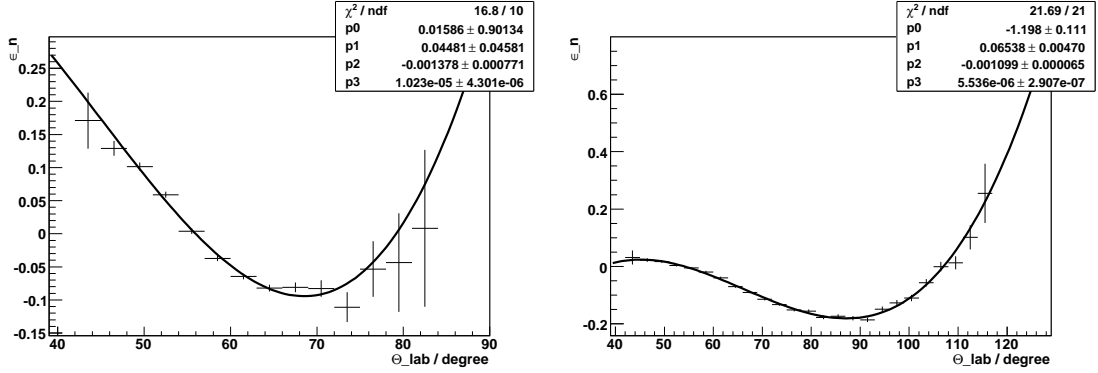

Figure 5.4: The shown data is from cycles without electron target and a detuning voltage of 426 V. Left: "MB" sample with a 3rd order polynomial fit. Right: "OT" sample with a 3rd order polynomial fit.

$$
\begin{aligned}
Ay_{MB}\left(\theta_d\right) &= 0.0159 + 0.0445\theta_d - 0.00137\theta_d^2 + 0.0000102\theta_d^3 \text{ and} & (5.3)\\
Ay_{OT}\left(\theta\right) &= -1.198 + 0.0654\theta - 0.00110\theta^2 + 0.00000554\theta^3. & (5.4)
\end{aligned}
$$

In the following two functions, with one fit parameter each, was used. They are

$$
\begin{aligned}
\epsilon_{MB} &= \alpha_{MB} \cdot Ay_{MB}\left(\theta_d\right) \text{ and} & (5.5)\\
\epsilon_{OT} &= \alpha_{OT} \cdot Ay_{OT}\left(\theta\right). & (5.6)
\end{aligned}
$$

The complete data set was fitted with this functions. The resulting factors α_{MB} and α_{OT} are given in tab. 5.4.

The same procedure was repeated with a 2nd and 4th order polynomial resulting in the same values for α_{MB} and α_{OT}. This ensures the independence to the used fit-function. The ratios of beam polarization can now be calculated by the ratios of α with and without electron target. The result is given in fig. 5.5.

Voltage Jump	Minimum Bias Sample		One Track Sample	
	with e^- target	without e^- target	with e^- target	without e^- target
0 V	1.114 ± 0.033	1.113 ± 0.034	1.001 ± 0.015	0.9982 ± 0.0148
246 V	1.037 ± 0.043	1.092 ± 0.064	1.025 ± 0.019	1.046 ± 0.028
301 V	1.106 ± 0.039	1.092 ± 0.042	1.063 ± 0.017	1.061 ± 0.018
348 V	1.093 ± 0.030	1.029 ± 0.034	1.009 ± 0.013	0.995 ± 0.015
426 V	1.029 ± 0.027	1.000 ± 0.027	0.999 ± 0.012	1.000 ± 0.012
−426 V	1.103 ± 0.029	1.038 ± 0.028	1.004 ± 0.012	0.999 ± 0.012

Table 5.4: For both samples with unknown analyzing power the fit values of the functions ϵ_{MB} and ϵ_{OT} for all detuning voltages. The result of 1.000 for 426 V without electron target is a necessity, as this data were used to prepare the fit-functions.

The usage of the fit functions instead of calculating the fractions of the asymmetries bin-by-bin, provides a check, that the asymmetries are stable and therefore that the event selection is stable over all data.

5.3   Depolarization Cross-Section

In tab. 5.5 the detune voltages ΔU used in this experiment, the detune velocity u_0 in the proton rest frame, the integrals $I_\parallel$ and $I_\perp$ of eqs. (3.19) and (3.20), and the average velocity $\overline{u}$ and its standard deviation. The calculation assumes a transverse electron temperature of $kT_e = 0.3\,\text{eV}$. The last two columns show the measured ratio R, of the polarization with and without electron target and its statistical uncertainty δR (sec. 5.2).

ΔU / V	u_0 / 10^{-3}c	$I_\perp$	$I_\parallel$	$\overline{u}$ / 10^{-3}c	$\Delta\overline{u}$ / 10^{-3}c	R	δR
-426	-2.53	338	25.8	2.82	0.23	1.01318	0.015764
0	0	777	777	0.64	0.49	1.00243	0.018935
246	1.46	482	79.4	1.86	0.30	0.97448	0.028898
301	1.79	429	54.3	2.15	0.27	1.00367	0.021365
348	2.07	391	40.3	2.40	0.25	1.0219	0.018402
426	2.53	338	25.8	2.82	0.23	1.00369	0.015216

Table 5.5: The detune voltages ΔU used in this experiment, the detune velocity u_0 in the proton rest frame, the integrals $I_\parallel$ and $I_\perp$ of eqs (3.19) and (3.20), and the average velocity $\overline{u}$ and its standard deviation. The calculation assumes a transverse electron temperature of $kT_e = 0.3\,\text{eV}$. The last two columns show the measured ratio R, of the polarization with and without electron target and its statistical uncertainty δR (sec. 5.2).

It is believed that the systematic errors of this measurement can be neglected, since the beam position was stable, the up and down polarizations were the same within statistics,
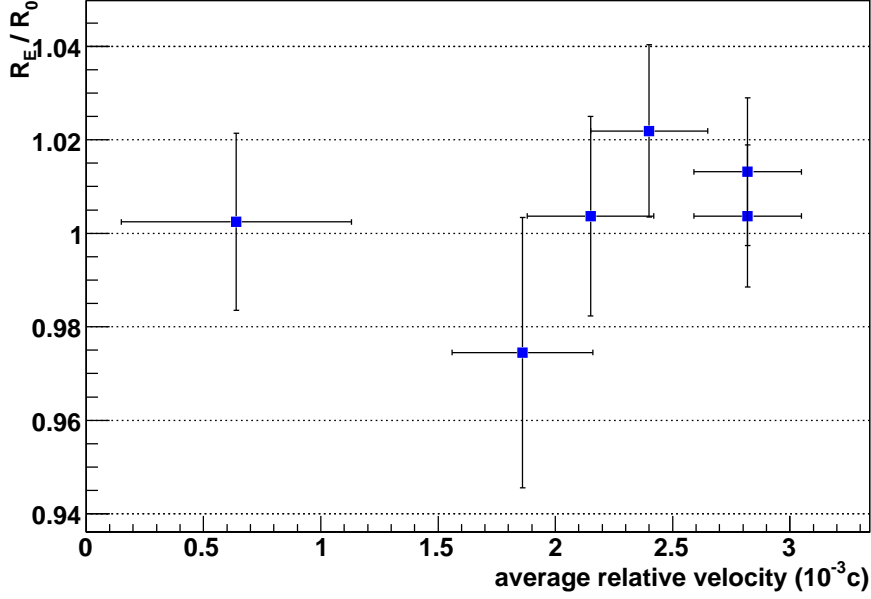
Figure 5.5: Ratio of the beam polarization with and without electron beam during the "interaction" part of the cycle as a function of the average relative velocity $\overline{v}$. The horizontal bars indicate the range $\Delta\overline{v}$ of velocities that contribute to the measurement. Here all data are taken into account.

and systematic asymmetries in beam current and target density cancel to first order in the cross ratio. Furthermore, the ratio R depends only on the *change* of the polarization between E-cycle and 0-cycle, and the actual value of the beam polarization (between 0.47 and 0.53) merely affects δR, while the normalization of the imported analyzing power cancels.

For each of the six detune potentials ΔU_k (k = 1,....,6) (tab. 5.5), the result of the measurement consists of the ratios $R_k \equiv (P_E/P_0)_k$. When combining eqs. 3.8 and 3.18 one obtains

$$y_k \equiv \frac{-ln(r_k)}{2\,c\,t_{int}\,n_{e,k}\,v^{\star 2}(L_C/L_r)} = \sigma_\perp \cdot I_{\perp,k} + \sigma_\parallel \cdot I_{\parallel,k}. \tag{5.7}$$

The denominator contains the speed of light, the interaction time $t_{int} = 245\,\text{s}$, the electron density n_e, the reference velocity eqn. 3.16, arbitrarily set to $v^\star = 0.002$, the active length $L_C = (1.75 \pm 0.25)\,\text{m}$ of the cooler, and the ring circumference $L_R = 183.47\,\text{m}$. The cooler length is uncertain because of details of inflection and extraction of the electron beam, and the electron density (eqn. 3.7) is affected by uncertainties of the electron beam current $I_e = 170\,\text{mA}$ and its area $A_e = 5\,\text{cm}^2$. The overall systematic uncertainty of the denominator is estimated to $\pm20\%$.

The polarization ratios R_k (fig. 5.5) are consistent with unity, i.e., the polarization differences between E-cycle and 0-cycle are of the order of their statistical errors.

The integral weights $I_{\parallel,k}$ and $I_{\perp,k}$ on the right side of eqn. (5.7) depend on the transverse electron temperature kT_e, which, for a number of reasons, is larger than the temperature of the emitting cathode, which operates at $900°\,\mathrm{C}$, corresponding to $kT_e = 0.1\,\mathrm{eV}$. The actual temperature, $kT_e = (0.3 \pm 0.1)\,\mathrm{eV}$, has been deduced from a measurement of the rate of electron pick-up by co-moving protons [Pot90].

The depolarizing cross sections, $\sigma_\parallel^\star$ and $\sigma_\perp^\star$ (at the reference velocity $v^\star$) appear as unknowns in eqn. (5.7). Since the experiment fails to find a depolarization effect, instead an upper limit for the two cross sections that is compatible with our data is derived. Following the usual treatment (see, e.g. [pdg08]), the likelihood function is defined as:

$$L(\overrightarrow{y}|\sigma_\perp^\star, \sigma_\parallel^\star) \equiv \prod_k exp\left(-\frac{(y_k - \sigma_\perp^\star I_{\perp,k} - \sigma_\parallel^\star I_{\parallel,k})^2}{2\delta y_k^2}\right). \tag{5.8}$$

The experimental result, y_k, is defined in eqn. (5.7); the statistical uncertainty δy_k follows from the error δR (tab. 5.5). Following the Bayesian approach, the posterior probability density function p is calculated by

$$p(\sigma_\perp, \sigma_\parallel|\overrightarrow{y}) = \frac{L(\overrightarrow{y}|\sigma_\perp^\star, \sigma_\parallel^\star)h(\overrightarrow{y}|\sigma_\perp^\star, \sigma_\parallel^\star)}{\int L(\overrightarrow{y}|\sigma_\perp^\star, \sigma_\parallel^\star)h(\overrightarrow{y}|\sigma_\perp^\star, \sigma_\parallel^\star)d\hat{\sigma}_\perp^\star d\hat{\sigma}_\parallel^\star}. \tag{5.9}$$

The function h reflects the prior knowledge (cross sections are positive numbers) and is set to a constant for all non-negative values $\sigma_\perp^\star$ and $\sigma_\parallel^\star$, and to zero otherwise.

The probability p is evaluated numerically and the probability area is shown in fig. 5.6. In 1500×1500 bins the value was calculated and the not normalized sum gives 13473.2. To test, that the area, which is not covered by the plot, gives only a negligible contribution to the normalization, the same plot was calculated, with identical binning, but a larger coverage. The not normalized sum in the area of $\sigma_{S,\perp} < 1.0 \cdot 10^6\,\mathrm{b}$ and $\sigma_{S,\parallel} < 1.6 \cdot 10^6\,\mathrm{b}$ with 2000×2000 bins gives a not normalized sum of 13473.2, as well.

The upper cross section limits, shown in fig. 5.7, are contours of constant p. The significance level is the integral of p over the region below the curve, and equals the probability that the two cross sections are less than the values along the contour. The parameters with a systematic uncertainty are taken to be completely unknown within the range equal to that uncertainty. So a conservatively value for these parameters (within this range) is chosen, that results in the largest upper limit.

5.4   Conclusion

In the experiment no depolarization of the stored proton beam due to ep spin-flip was observed. Upper limits on the transverse and longitudinal spin-flip cross-sections $\sigma_\perp^\star$ and $\sigma_\parallel^\star$ at a relative velocity of $v^\star = 0.002\,c$ are $4 \cdot 10^6\,\mathrm{b}$ and $7 \cdot 10^6\,\mathrm{b}$, respectively, at $99\,\%$ significance level (Fig. 5.7). This is in clear contradiction to the cross-section of $2 \cdot 10^{13}\,\mathrm{b}$ predicted by the Mainz group [Are07]. Due to the low electron-target density the sensitivity
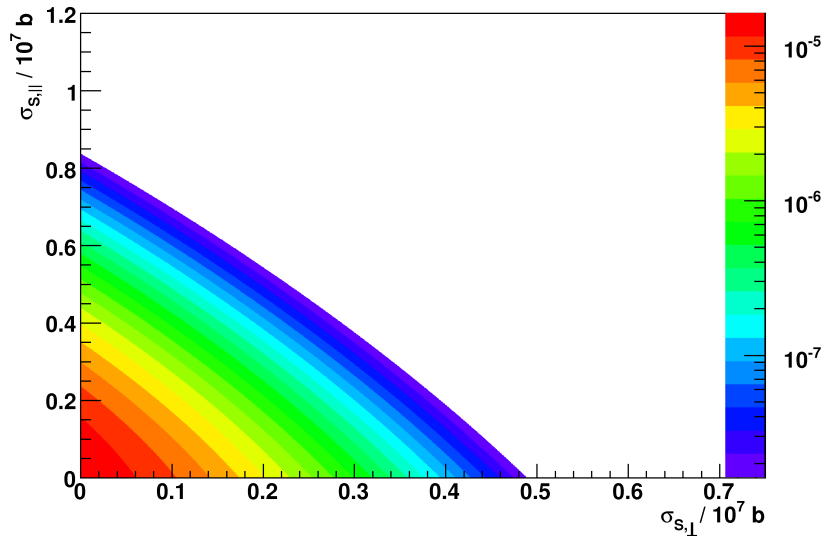
Figure 5.6: Probability function p, as a function of the two depolarizing cross-sections $\sigma_{S,\perp}^{\star}$ and $\sigma_{S,\parallel}^{\star}$.

of this experiment is too small to verify the prediction of $0.75\,\mathrm{mb}$ calculated with help of perturbation theory using the exact non-relativistic Coulomb wave functions [Mil08].

Preliminary results of the experimentally deduced cross-section have been shown at the WE-Heraeus-Seminar *"Polarised Antiprotons"* in Bad Honnef, June 2008 [Her08]. Later, an erratum[Are09] on [Are07] was published giving a corrected value of $30\,\mathrm{mb}$. The numerical calculation in the distorted-wave approximation for the hyperfine contribution led to a difference of two almost equal numbers multiplied by a large number. A numerical problem in the evaluation led to the tremendous overestimation of the cross-section.

As any experiment, which would make use of this cross-section, would lack on a high free-electron-target density, this effect is far too small for an efficient polarization buildup of a stored antiproton beam. Comparing the deduced upper limit in the order of $10^6\,b$ with the new theoretical result of $30\,mb$ it becomes clear, that at least 8 orders of magnitude are missing. Thus this method to produce a stored polarized antiproton beam is killed [Wal09].
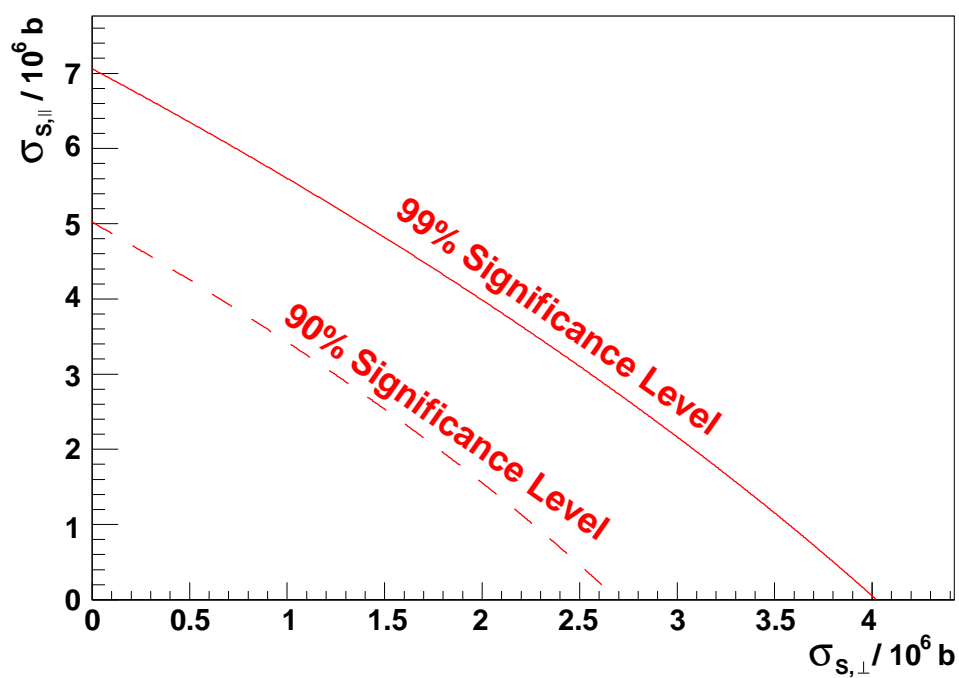
Figure 5.7: Upper limit allowed by the data of this experiment for the transverse and the longitudinal spin flip cross sections $\sigma^\star_{S,\perp}$ and $\sigma^\star_{S,\parallel}$ at a relative velocity of $v^\star = 0.002$, corresponding to a center-of mass energy of about $1\,\text{eV}$. The significance level is the probability that the actual cross sections are smaller than the values on the contour line.

Chapter 6

Conclusion and Outlook

Within the scope of this thesis, the ANKE silicon tracking telescopes have been optimized to work as a polarimeter. By using e.g. proton-deuteron elastic scattering the beam polarization can be detected over a wide energy range. In an experiment, these detectors have been used to measure the beam polarization. The major part of this thesis deals with the polarization analysis.

The depolarization of a proton beam by electron-proton spin-flip was observed at six relative velocities between 0 and $3 \cdot 10^{-3}$ c. All data points are within errors consistent with a zero cross-section. They have been extrapolated to a reference velocity of $v^{\star} = 2 \cdot 10^{-3}$ c and as a result the upper limits of the spin-flip cross-sections $\sigma_{\parallel}^{\star}$ and $\sigma_{\perp}^{\star}$ yield $7 \cdot 10^{6}$ b and $4 \cdot 10^{6}$ b at 99 % significance level (Fig. 5.7). After the first results were disclosed - later published in [Oel09] -, errata on the prediction were published [Are09, Wal09]. These give a cross-section of 30 mb, which is still about a factor of 30 larger than the precictions from Milstein et al. [Mil05, Mil08]. It is shown, that the measured cross-section σ_{S} is an upper limit of the positron-antiproton spin-flip cross-section $\Delta\sigma_{S}$ for polarization build-up. This experiment clarifies the role of electrons in spin filtering experiments and as a consequence shows that co-moving positrons are not a reasonable method to polarize a stored antiproton beam. Therefore, the PAX-Collaboration proposed to polarize a stored antiproton beam by spin-filtering at the CERN-AD [PAX09]. The existing silicon tracking telescopes could be used as a detection system to measure the beam polarization. In preparation of these experiments at the CERN-AD, a spin-filtering experiment is currently set-up at COSY. Depending on the outcome of the antiproton spin-filtering studies the PAX-Collaboration is aiming at experiments with polarized antiproton beams to measure the transversity distribution.

Appendix A

Polarization Evolution

To describe the time-dependence of the polarization in a stored spin-$\frac{1}{2}$ beam, 4 different spin dependent cross sections are needed. In the following the two spin states of the beam are indicated as $\uparrow$ for spin up and $\downarrow$ for spin down particles: $\sigma_{\uparrow\uparrow}^{R}$, $\sigma_{\uparrow\downarrow}^{R}$, $\sigma_{\uparrow\uparrow}^{SF}$ and $\sigma_{\uparrow\downarrow}^{SF}$. Here the indices $\uparrow\uparrow$ ($\uparrow\downarrow$) indicate parallel (anti-parallel) spins of the beam particle and target particle. "R" stands for scattering out of the machine acceptance, while "SF" stands for scattering within the machine acceptance, but with spin flip.

With $N_\uparrow$ and $N_\downarrow$ giving the number of beam-particles in each spin state, the target area density d_t, the target polarization Q and the beam revolution frequency of f_{rev}, one can give the time dependence of $N_\uparrow$ and $N_\downarrow$:

$$
\begin{aligned}
\frac{d}{dt}N_\uparrow(t) = -d_f \cdot f_{rev} \cdot \Bigg(\quad & \sigma_{\uparrow\uparrow}^{R} \cdot \frac{1+Q}{2} \cdot N_\uparrow(t) + \sigma_{\uparrow\downarrow}^{R} \cdot \frac{1-Q}{2} \cdot N_\uparrow(t) \\
+ \quad & \sigma_{\uparrow\uparrow}^{SF} \cdot \frac{1+Q}{2} \cdot N_\uparrow(t) + \sigma_{\uparrow\downarrow}^{SF} \cdot \frac{1-Q}{2} \cdot N_\uparrow(t) \\
- \quad & \sigma_{\uparrow\uparrow}^{SF} \cdot \frac{1-Q}{2} \cdot N_\downarrow(t) - \sigma_{\uparrow\downarrow}^{SF} \cdot \frac{1+Q}{2} \cdot N_\downarrow(t) \Bigg),
\end{aligned}
\tag{A.1}
$$

$$
\begin{aligned}
\frac{d}{dt}N_\downarrow(t) = -d_f \cdot f_{rev} \cdot \Bigg(\quad & \sigma_{\uparrow\uparrow}^{R} \cdot \frac{1-Q}{2} \cdot N_\downarrow(t) + \sigma_{\uparrow\downarrow}^{R} \cdot \frac{1+Q}{2} \cdot N_\downarrow(t) \\
+ \quad & \sigma_{\uparrow\uparrow}^{SF} \cdot \frac{1-Q}{2} \cdot N_\downarrow(t) + \sigma_{\uparrow\downarrow}^{SF} \cdot \frac{1+Q}{2} \cdot N_\downarrow(t) \\
- \quad & \sigma_{\uparrow\uparrow}^{SF} \cdot \frac{1+Q}{2} \cdot N_\uparrow(t) - \sigma_{\uparrow\downarrow}^{SF} \cdot \frac{1-Q}{2} \cdot N_\uparrow(t) \Bigg).
\end{aligned}
\tag{A.2}
$$

For each spin state three different terms are contributing. The first describes the scattering out the machine acceptance depending on the fraction $\frac{1+Q}{2}$ (or $\frac{1-Q}{2}$) of target particles in the spin state up (or down). The second term gives the loss due to spin flip into the other state, while the third term gives the increase due to spin flip from the other state.

With the abbreviations $\sigma_R = \frac{1}{2}\left(\sigma_{\uparrow\uparrow}^{R} + \sigma_{\uparrow\downarrow}^{R}\right)$, $\Delta\sigma_R = \frac{1}{2}\left(\sigma_{\uparrow\downarrow}^{R} - \sigma_{\uparrow\uparrow}^{R}\right)$, $\sigma_S = \frac{1}{2}\left(\sigma_{\uparrow\uparrow}^{SF} + \sigma_{\uparrow\downarrow}^{SF}\right)$

and $\Delta\sigma_S = \frac{1}{2}\left(\sigma_{\uparrow\downarrow}^{SF} - \sigma_{\uparrow\uparrow}^{SF}\right)$ the equations simplify to:

$$
\frac{d}{dt}N_\uparrow(t) = -d_f \cdot f_{rev} \cdot \Big(\ \ (\sigma_R - \Delta\sigma_R \cdot Q) \cdot N_\uparrow(t)
$$
$$
+ \ \ (\sigma_S - \Delta\sigma_S \cdot Q) \cdot N_\uparrow(t)
$$
$$
- \ \ (\sigma_S + \Delta\sigma_S \cdot Q) \cdot N_\downarrow(t)\Big), \tag{A.3}
$$

$$
\frac{d}{dt}N_\downarrow(t) = -d_f \cdot f_{rev} \cdot \Big(\ \ (\sigma_R + \Delta\sigma_R \cdot Q) \cdot N_\downarrow(t)
$$
$$
+ \ \ (\sigma_S - \Delta\sigma_S \cdot Q) \cdot N_\downarrow(t)
$$
$$
- \ \ (\sigma_S + \Delta\sigma_S \cdot Q) \cdot N_\uparrow(t)\Big). \tag{A.4}
$$

This system of coupled differential equations can be solved analytically. The solutions are unique with two initial conditions. Here the initial beam intensity and beam polarization are used.

$$
N_0 \ = \ N_\uparrow(0) + N_\downarrow(0) \tag{A.5}
$$

$$
P_0 \ = \ \frac{N_\uparrow(0) - N_\downarrow(0)}{N_\uparrow(0) + N_\downarrow(0)} \tag{A.6}
$$

With $A = \sqrt{\Delta\sigma_R(2\Delta\sigma_S + \Delta\sigma_r)Q^2 + \sigma_S^2}$ the solution is:

$$
N_\uparrow = \frac{N_0}{4A}\Bigg\{ \Big[(1 + P_0) \cdot A + (\Delta\sigma_R Q - \sigma_S) \cdot P_0 \ + \ (2\Delta\sigma_S + \Delta\sigma_R) \cdot Q + \sigma_S\Big]
$$
$$
\cdot e^{-(\sigma_S + \sigma_R - A)f_{rev}\, d_t \cdot t}
$$
$$
+ \Big[(1 + P_0) \cdot A - (\Delta\sigma_R Q - \sigma_S) \cdot P_0 \ - \ (2\Delta\sigma_S + \Delta\sigma_R) \cdot Q - \sigma_S\Big]
$$
$$
\cdot e^{-(\sigma_S + \sigma_R + A)f_{rev}\, d_t \cdot t}\Bigg\}, \tag{A.7}
$$

$$
N_\downarrow = \frac{N_0}{4A}\Bigg\{ \Big\{\big[(1 - P_0) \cdot \Delta\sigma_R + 2\Delta\sigma_S\big] \cdot Q \ - \ (1 + P_0) \cdot \sigma_S + (P_0 - 1)\Big\}
$$
$$
\cdot e^{-(\sigma_S + \sigma_R - A)f_{rev}\, d_t \cdot t}
$$
$$
\Big\{\big[(P_0 - 1) \cdot \Delta\sigma_R - 2\Delta\sigma_S\big] \cdot Q \ + \ (1 + P_0) \cdot \sigma_S + (P_0 - 1)\Big\}
$$
$$
\cdot e^{-(\sigma_S + \sigma_R + A)f_{rev}\, d_t \cdot t}\Bigg\}. \tag{A.8}
$$

The polarization evolution function is $\frac{d}{dt}P(t) = \frac{d}{dt}\frac{N_\uparrow(t) - N_\downarrow(t)}{N_\uparrow(t) + N_\downarrow(t)}$. As this gives a long formula, here an approximation is used: The derivation is evaluated at $t = 0$ resulting in formulas which are good, as long as the initial conditions P_0 and N_0 are close to $P(t)$ and $N(t)$.

$$
\left.\frac{d}{dt}P(t)\right|_{t=0} = f_{rev} \cdot d_t \left[Q(1 - P_0^2)\Delta\sigma_R + 2Q\Delta\sigma_S - 2P_0\sigma_S\right], \tag{A.9}
$$

while the derivation of the number of beam-particles is

$$\frac{d}{dt}N(t)\bigg|_{t=0} = -f_{rev} \cdot d_t \left[\sigma_R - QP_0\Delta\sigma_R\right]N_0. \tag{A.10}$$

Two special cases are of interest. The first one deals with polarizing an initially unpolarized beam ($P_0 = 0$). As long as the beam polarization P is small, the rate of change of polarization is given by:

$$\frac{dP}{dt} = f_{rev} \cdot d_t \cdot Q \left[2 \cdot \Delta\sigma_S + \Delta\sigma_R\right]. \tag{A.11}$$

The "polarizing cross section", σ_{pol} is defined as the sum of the two terms in the bracket:

$$\sigma_{\mathrm{pol}} = 2 \cdot \Delta\sigma_S + \Delta\sigma_R \tag{A.12}$$

The second special case describes the effect of an unpolarized target ($Q = 0$) on an already polarized beam,

$$\frac{dP}{dt} = -2f_{rev} \cdot d_t\sigma_S P, \tag{A.13}$$

which shows that the "depolarizing cross section" is directly proportional to the spin flip cross section σ_S. Since the sum of two positive values is always bigger than the norm of their difference, it is $\sigma_S \geq \Delta\sigma_S$ and it follows from eqs. A.11 and A.13 that *if a polarized target is capable of polarizing an unpolarized beam by spin flip, an unpolarized target will depolarize an already polarized beam.*

Appendix B

Machine Studies

As long beam lifetimes and polarisation lifetimes are essential to perform spin filtering experiments, several machine studies have to be performed in order to test these parameters. Here the summary of the study on the beam lifetime is given.

B.1 Beam Lifetime

B.1.1 Goal and Status

The PAX collaboration plans to perform experiments with stored polarised antiproton beams at FAIR. The existing data from FILTEX shows that spin filtering is working. Presently, there exist two competing theoretical scenarios: one with substantial spin filtering of (anti-)protons by atomic electrons, while the second one suggests an almost exact self-cancellation of the electron contribution to spin filtering. To distinguish between these scenarios a depolarising study of a stored polarised proton beam with an kinetic energy of $T_p = 45\,\mathrm{MeV}$ was proposed at COSY-PAC in autumn 2006 [Oel06, Oel07]. With electrons in a ^4He or a D_2 target it should be possible to measure the electron contribution to spin filtering. To achieve 4-5 σ significance in 4 weeks of data taking the following beam requirements are needed:

The goal of this machine development is to improve the beam lifetime at injection energy to reach the necessary lifetime of $\sim 10000\,\mathrm{s}$ without target and $\sim 2700\,\mathrm{s}$ with target.

So far, only $\sim 800\,\mathrm{s}$ [Die04] at the injection energy of 44.83 MeV without target have been observed, although calculations[1] show that a lot can be improved.

B.1.2 Machine Setup

A change in the magnet settings at injection energy can lead to a complete loss of the injection as the matching conditions for the injected beam are defined by the quadrupole setting in the ring. Lattice functions x, x$'$, $\beta_{x,y}$, $\alpha_{x,z}$ of the beam line have to match the

---

[1]Archil Garishvili

Parameter	Value
Target Thickness	$2 \cdot 10^{14} \, \text{cm}^{-2}$
Beam Intensity	$2 \cdot 10^{10}$ stored protons
Initial Beam Polarisation	0.8
Beam Lifetime with target	2700 s
Beam Lifetime without target	10000 s
Beam Polarisation Lifetime	45000 s
Beam Energy	45 MeV

Table B.1: Set of parameters to evaluate the depolarising effect of the electrons in a deuterium cluster target with 4-5 σ accuracy.

ring parameters. By changing the ring focussing elements these parameters also change. To keep the injection one then has to re-adjust the beam line to match the new ring parameters. To avoid frequent re-adjusting, which consumes a lot of time, it was planned to work at "flat top" after the smallest possible acceleration. For the unpolarised proton beam a ramp from $p = 293.48 \, \text{MeV/c}$ up to $p = 295 \, \text{MeV/c}$ was introduced[2]. This is equivalent to beam kinetic energies of $T = 44.83 \, \text{MeV}$ and $T = 45.28 \, \text{MeV}$, respectively.
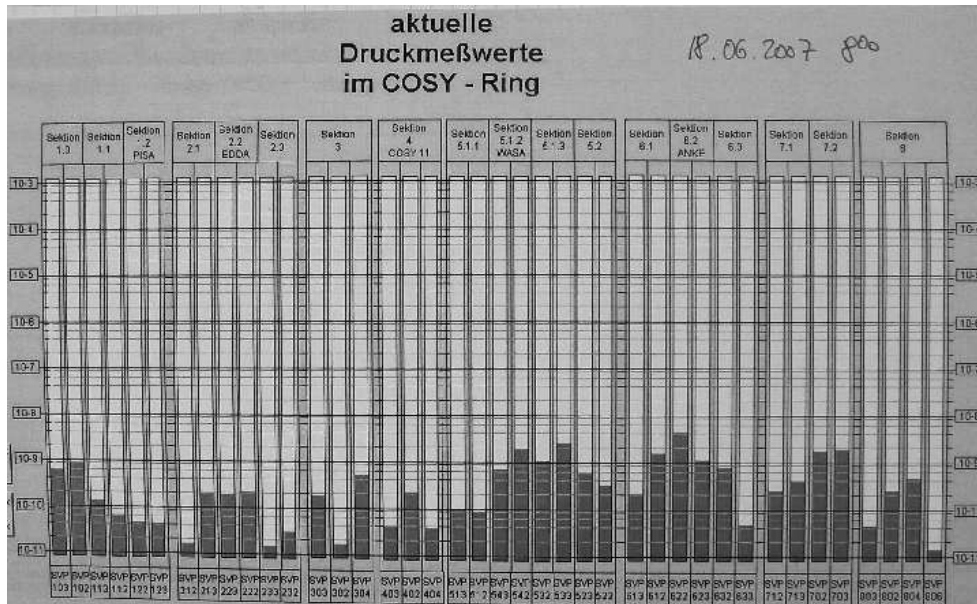
Figure B.1: Pressure distribution of the COSY ring on 18th of June 2007.

It is extremely important to know which contribution to beam lifetime is due to the residual gas. So in the beginning of the beam development each of the mass spectrometers

---

[2]Dieter Prashun

installed in the ring has been read out. From these data combined with the total pressure in each section the partial pressures of some prominent gases in every section of the ring have been calculated[3].
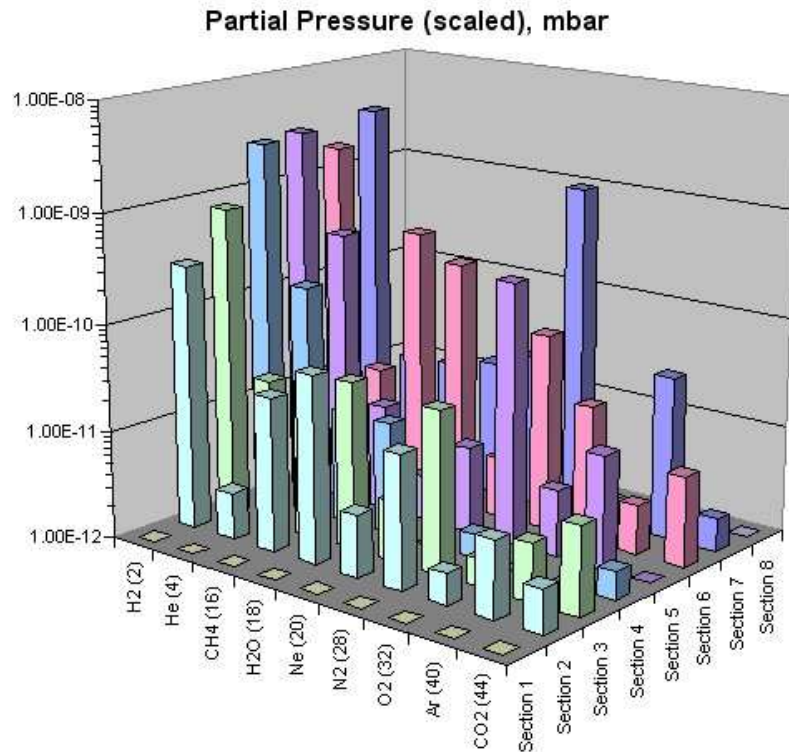

Figure B.2: Main residual gas components in every COSY section at the beginning of the beam development.

In figure B.2 one can clearly see, that H_2 is the dominating gas in the COSY ring. In section 7 there is a big contribution from nitrogen, which is an indication for a leakage. The nitrogen contribution to the residual gas will produce roughly as much Coulomb scattering losses as the H_2 contribution due to the Z^2 dependence. Additionally, one should mention that the residual gas monitor (RGM) from GSI people in section 7 is producing a lot of residual gas of every kind every time the voltage is switched on. In the whole ring, the titanium sublimation pumps (TSP) were switched on, and the vacua were quite good. Nevertheless, the TSP's were heated every 5 hours, which caused temporary pressure increase. The improvements like closing the leakages and removing the RGM should immediately lead to higher beam lifetimes.

A MAD[4] calculation aimed at estimating the beam lifetime has been performed[5]. The area occupied by particles in phase space at the beginning of a beam transport line allows to

---

[3]Kirill Grigoriev

[4]**M**ethodical **A**ccelerator **D**esign

[5]Archil Garishvili and Bernd Lorentz [PAX-note-3/2007]

determine the location and distribution of the beam at any other place along the transport
line. In phase space it is an ellipse and the area is a constant parameter at any point of the
ring. Its shape and orientation are fixed by three parameters α, β and γ (see figure B.3).
The acceptance is computed from the relation:

$$A_{x,y}(s)/\pi\,mm\,mrad = \frac{r_{x,y}^2(s)/mm}{\beta_{x,y}(s)/mm},$$

and leads to a result of A = 42.35 π mm mrad for the six-fold symmetry of the ring[6]. The
acceptance limit is located in the arcs.
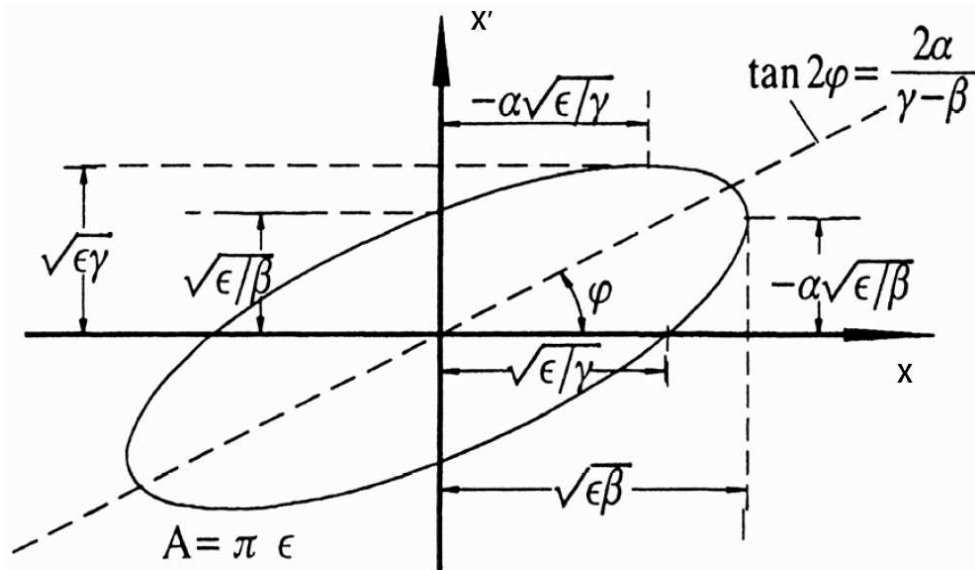
Figure B.3: Phase space ellipse.

With this number, the γ at each point of the ring and the single Coulomb scattering
cross section, the lifetime contribution from each residual gas is calculated. As result the
total lifetime for the COSY beam without target is 11300 s.

During the beam development the lifetime has been determined online using a fit of the
BCT (beam current transformer) signal available in the data stream. Several exponential
fits to the BCT have been made available. Data from the Schottky spectra have been
monitored to ensure that the revolution frequency and energy spread are stable. In the
electron cooler beam protons recombine with electrons to H^0. These atoms can be detected
to measure the beam profile. The detection system comprises 2 proportional chambers with
wires placed horizontally and vertically, and 2 scintillation counters giving the integral flux
of H^0s. Since the MWPCs were not working properly, the profile has not been measured
in this beam development, although the rate of H^0s has been permanently monitored. The

---

[6]Number of periods in lattice functions counted in the arcs.

H^0 rate should be proportional to the beam current, provided that the relative conditions of the electron beam and the stored beam do not change. For two cycles the rate of H^0/I is shown in figure B.4.
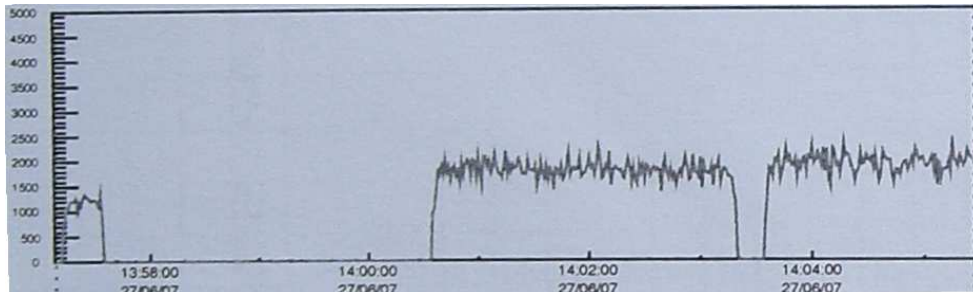

Figure B.4: Counting rate of H^0 divided by the beam intensity in arbitrary units as a function of time.

For studies of the target effect on the beam lifetime, a storage cell has been prepared. This could be filled with different gases. The gas inlet needed to be calibrated in terms of the target thickness. The calibration plots for different gases are shown in figure B.5[7].

B.2 Closed Orbit Manipulations and Acceptance Measurement

Initial closed orbit ranged within ± 7 mm vertically and ± 18 mm horizontally. The biggest machine acceptance is achieved, if orbit is in centre of the beam pipe. In order to reach the best orbit with the storage cell and the electron cooler a 3-step approach has been chosen:

1. Optimisation without electron-cooler magnets switched on (see figure B.6), where the orbit stayed within 5 mm both vertically and horizontally.

2. Optimisation with electron-cooler magnets on. The orbit has also been flattened, down to 12 mm, although not being as good as without the cooler (see figure B.7).

3. Optimisation with the storage cell. This did work without any problem, and no changes to the orbit were needed.

An attempt to further improve the orbit with help of the orbit response matrix, based on the BPM reaction to local orbit kicks has been carried out[8]. But there was only very limited time to test this method, and it has failed. It has also been found out, that some of the BPMs and kickers could have been wrongly connected. In addition, the BPMs had

---

[7]The calibration for N_2 plotted here is not correct as different settings for a valve opening have been used and have led to a changed device conductance.
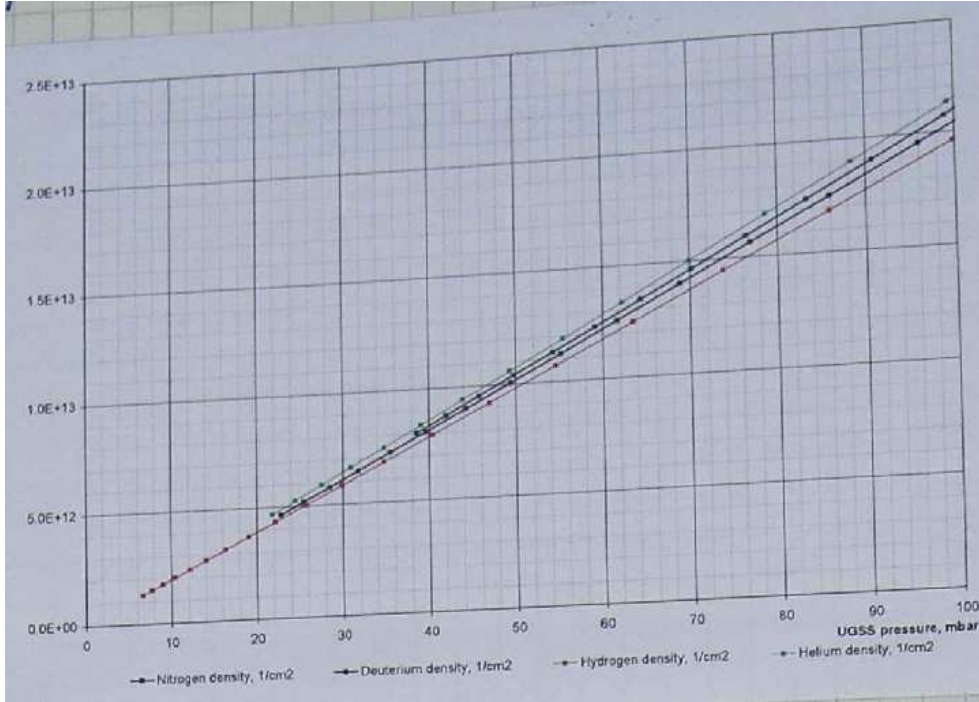
[8]Dominik Welsch

Figure B.5: Calibration curve: Target density in particles / cm^2 *vs* pressure in the unpolarised gas supply system (UGSS).

never been exactly calibrated, thus can have an offset in the middle position. It is worth to have an additional look into this.

To measure the acceptance, a fast kicker has been used. As it is able to kick only in the horizontal plane, this measurement can only give an upper limit for the machine acceptance. For each kick the beam emittance ϵ is calculated as $\epsilon = \Theta^2/\gamma$, with the kick angle Θ and the beta function at the kicker of $\gamma = 0.1797$ /m. A calibration curve of the kicker (see figure B.8) is used to get the kick angle from the voltage at the kicker. From the voltage one can calculate the current and the magnetic field. The kick angle Θ is calculated by $\Theta = \frac{\int BdL}{B\rho}$, with the magnetic rigidity $B\rho = 984.002$ mT m and $\int BdL$ being the integral of the magnetic field along the kicker.

The survival probability p is calculated using $p = \frac{BCT_f}{BCT_i}$, with BCT_f and BCT_i the BCT signal before (i) and after (f) the kick. The acceptance is the value, where the survival probability drops to zero. There have been two measurements: one with the beam passing through the storage cell, and second with the storage cell moved out of the beam. Both results are shown in figure B.9.

For both measurements with and without the storage cell the measured acceptance is very similar and has the value of $\approx 20\,\pi$ mm mrad. Therefore, the storage cell is not the acceptance limitation. In order to study the machine acceptance and the beam lifetime,
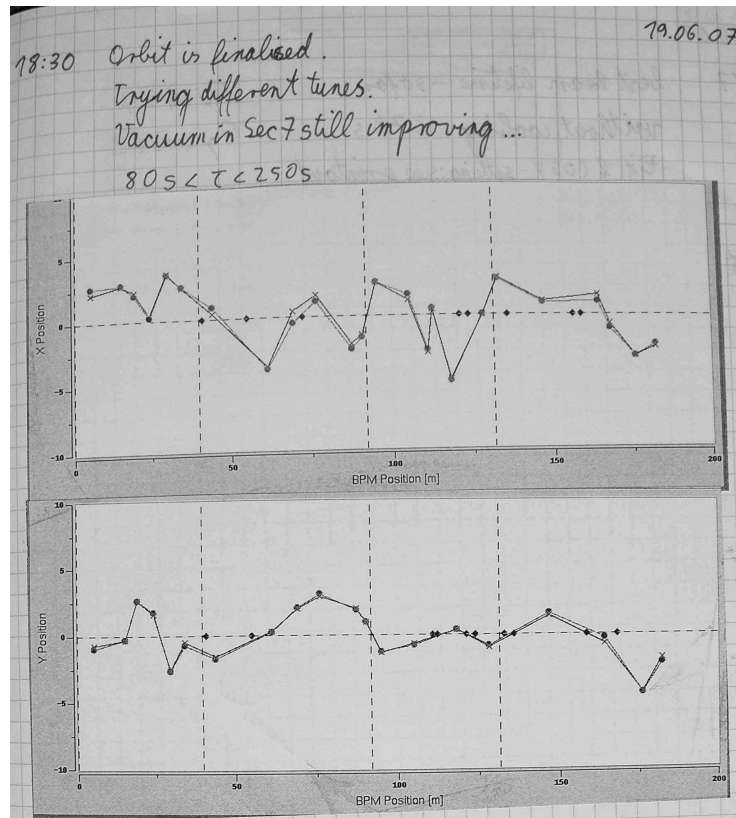
Figure B.6: Beam orbit after closed orbit manipulations with all electron-cooler magnets switched off.

that can be reached a MAD-calculation has been carried out.[9]. For horizontal and vertical direction the beam was deferred randomly from the beam pipe centre and the acceptance was calculated. The dependence of the acceptance on the different maximum deviations is plotted in figure B.10 for each plane with and without a storage cell. For all calculations it was assumed, that the beam was in the centre of the storage cell.

For the horizontal plane one can clearly see, that the storage cell is the acceptance limit. The acceptance drops from $> 160\,\pi\,\mathrm{mm\,mrad}$ to $36\,\pi\,\mathrm{mm\,mrad}$. The acceptance with storage cell shows no dependence on the orbit deviation. From this one concludes that even with orbit deviations of $10\,\mathrm{mm}$ the storage cell is the acceptance limit. For the vertical plane things are different. The acceptance is $< 42\,\pi\,\mathrm{mm\,mrad}$ without storage cell and $< 28\,\pi\,\mathrm{mm\,mrad}$ with storage cell. It is much lower than in the horizontal plane. The kink in the plot with the storage cell indicates, that with orbit deviations of $6\,\mathrm{mm}$ or more the acceptance limitation moves from the storage cell to the ring and drops to $20\,\pi\mathrm{mm\,mrad}$ at $10\,\mathrm{mm}$ orbit deviations. This is in good agreement with the acceptance measurement performed with the kicker. The uncalibrated BPM measurements show an
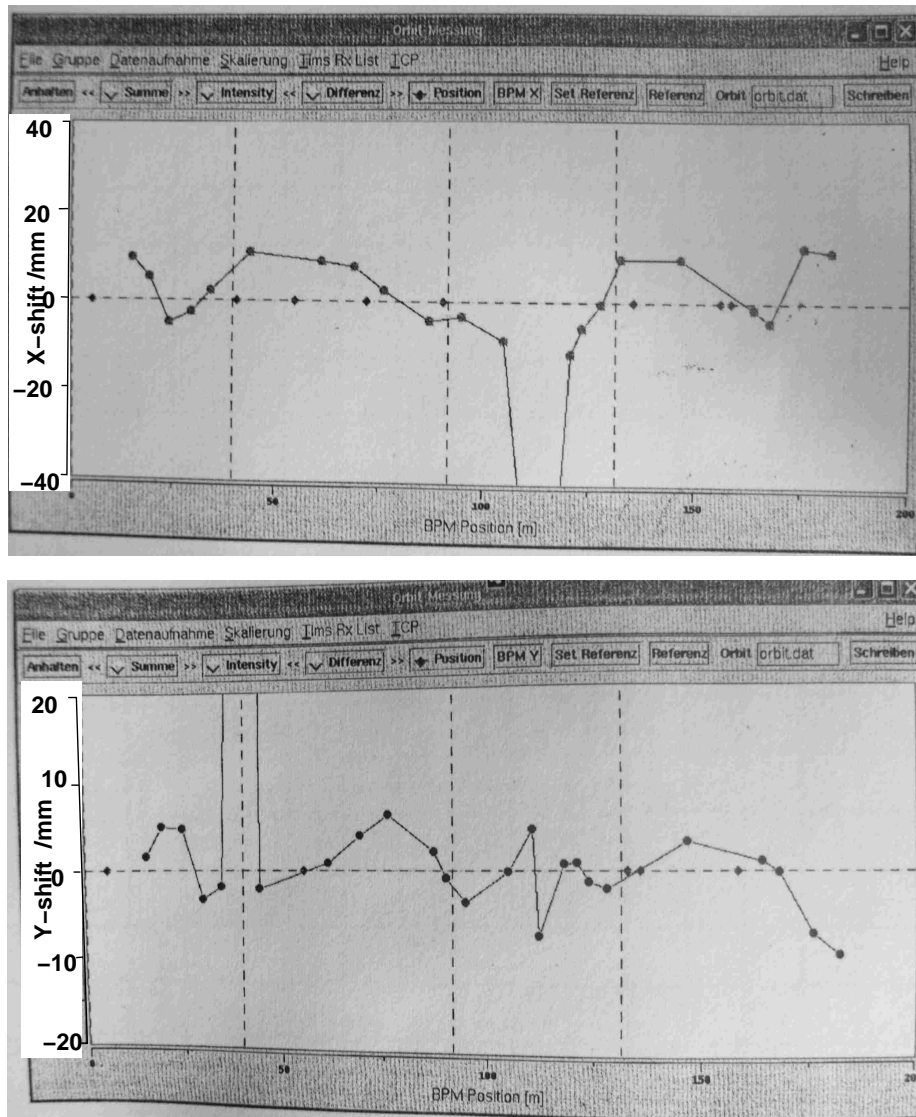
---

[9]Archil Garishvili

Figure B.7: Beam orbit with electron-cooler magnets switched on.

orbit with roughly 12 mm deviations. Further calculations show that with the storage cell the beam lifetime drops from 7400 s to 5400 s because of the orbit deviations (see figure B.11). So it becomes clear, that the orbit limited within 12 mm leads to a serious acceptance limit, and, therefore, has to be improved for further measurements.
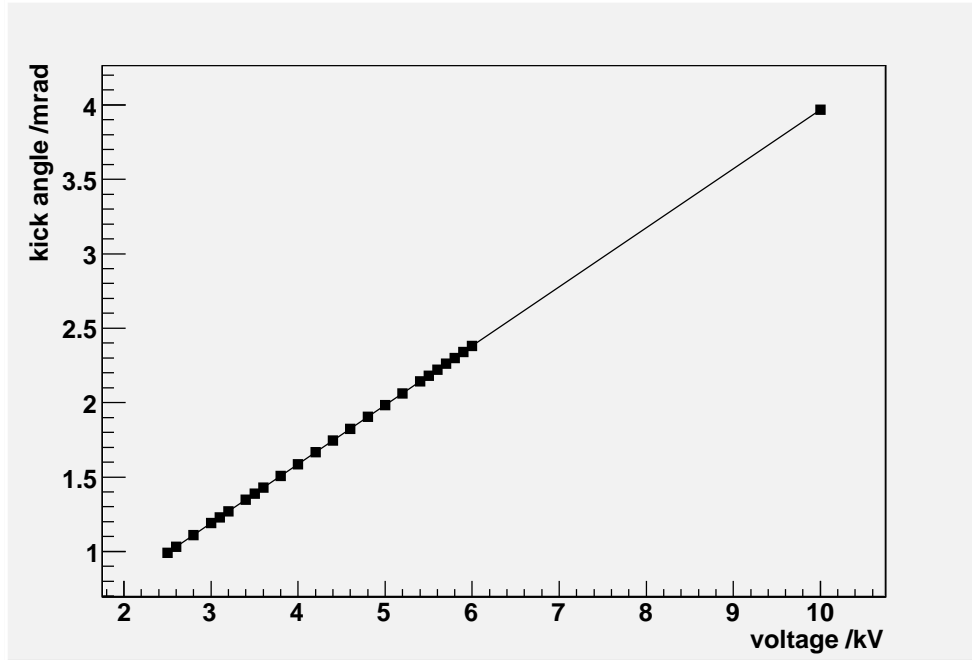
Figure B.8: Calibration curve for the horizontal kicker. Voltage at the kicker *vs* kick angle Θ. The markers show the points used for the acceptance measurement.

B.3 Tune Scans and Beam Lifetime

The beam lifetime strongly depends on the chosen machine tunes. Ideally the tunes should be irrational numbers, while in practice one just tries to stay far from the machine resonances, plotted in figure B.12 up to 7th order.

To change the tunes, the current in two families of quadrupoles (Quad 1-3-5 and 2-4-6, due to the 6-fold symmetry) was varied to map the empty region of the tune diagram around $Q = 3.61$, and a lifetime has been recorded for each tune combination. The result of the measurements is presented in figure B.13.

The gap around $Q_x = Q_y$ is a clear indication for coupling between the x- and y-planes, but also a region where higher lifetimes are expected. The determined lifetimes *vs* the tune difference are shown in figure B.14.

Here the two measurements near $\Delta Q = -0.4$ show the highest lifetimes. Further investigations close to these points should be performed in the next beam development period at injection energy. Reducing the coupling to reach the region closer to $Q_x = Q_y$ has been achieved by adjusting the sextupole magnets of COSY. After this change the gap in the tune plot has been reduced. These results are included into the plot with brown points. They do not show an increase in lifetime, and are even not stable without any explanation for it. The lifetime of all measurements is shown in figure B.15.

With the properly electron cooled beam, a pure exponential behaviour of the beam current has been observed (see figure B.16). Therefore, the beam losses are mainly due to
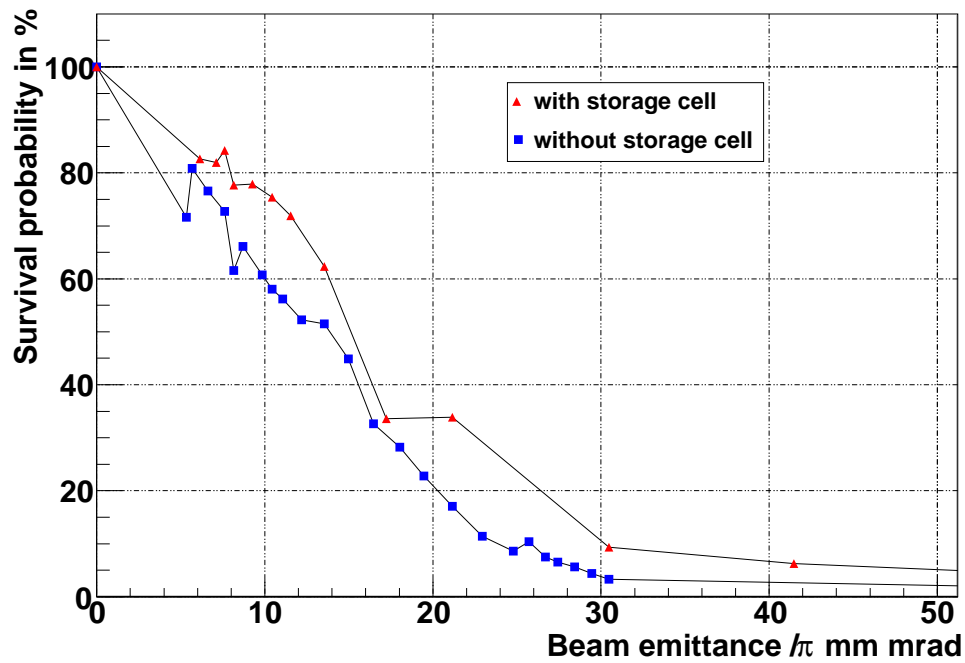
Figure B.9: Survival probability *vs* emittance.
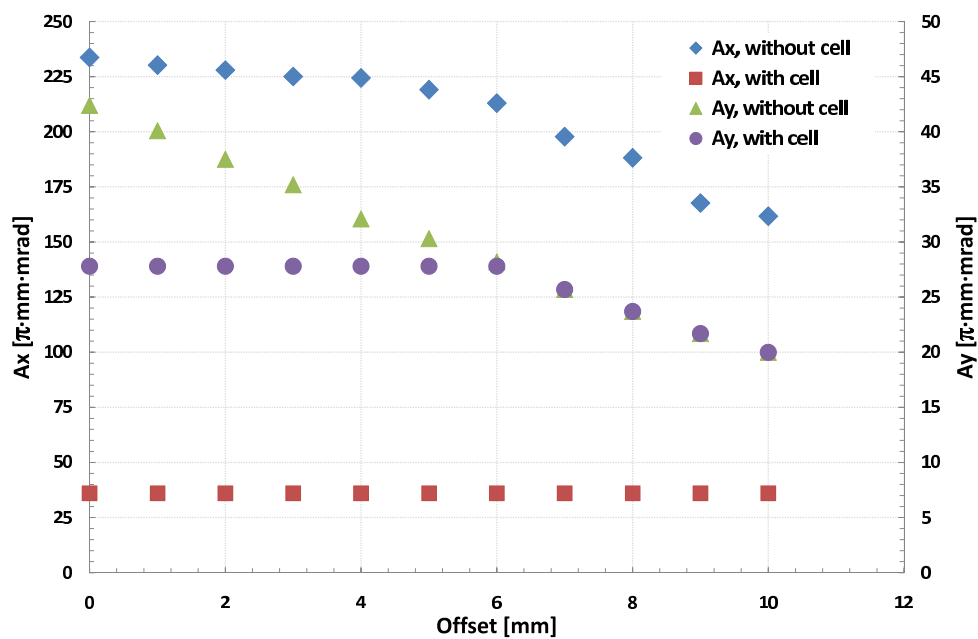
Figure B.10: The plot shows the orbit deviations *vs* the vertical and horizontal acceptance with and without the storage cell.
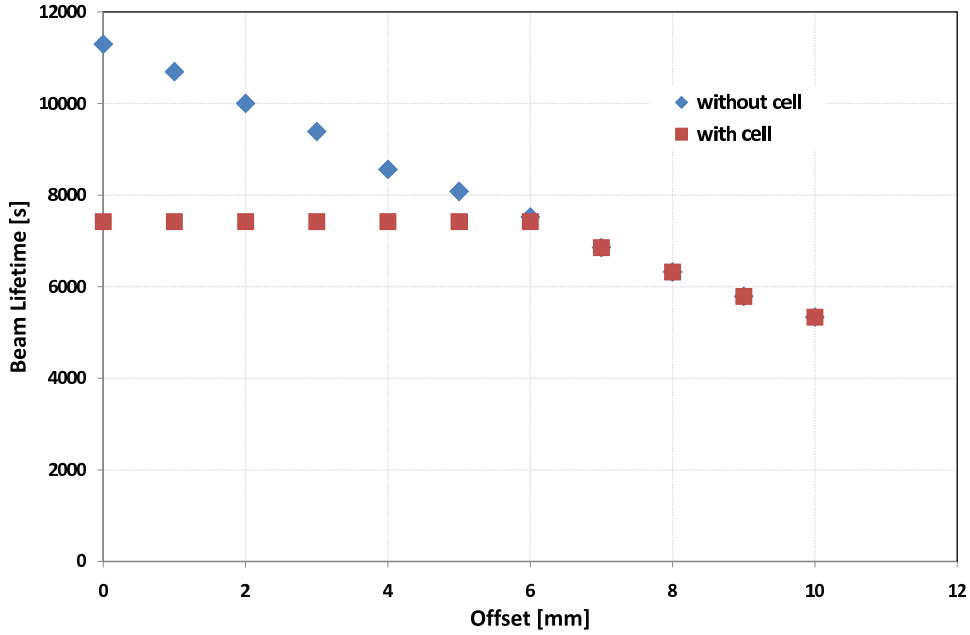
Figure B.11: Beam lifetime as a function of orbit deviations.

single Coulomb scattering.

The second plot in figure B.16 shows the $dBCT/dt$ signal, and the beam lifetime is calculated by $\tau = -\frac{BCT}{\frac{d(BCT)}{dt}}$. Here one can see the points representing the beam lifetime grouped into lines. A Fourier analysis is needed to clarify the structure.

B.4   Coupling with Electron Cooler Solenoids

By kicking the beam with different frequencies in the x- and y-direction and measuring the amplitude of the beam oscillations the tunes show up as narrow peaks in this spectra. Tunes with $Q_x = Q_y$ are not reachable due to the coupling of the x- and y-planes. This coupling leads to a rotation of the eigenvectors of the transversal oscillations with respect to the x- and y-planes. So one sees both frequencies in both x and y spectra. Only from the amplitudes of each peak one could associate one frequency to a plane. But sometimes this does lead to an ambiguity which can't be resolved. Two reasons for coupling are:

- Sextupole magnets.

- Not compensated solenoid field.

- Torodial field (in E-Cooler).

The solenoid of the electron cooler has compensating magnets, with which the overall solenoidal field of the cooler should be zero. From the minimum difference the coupling
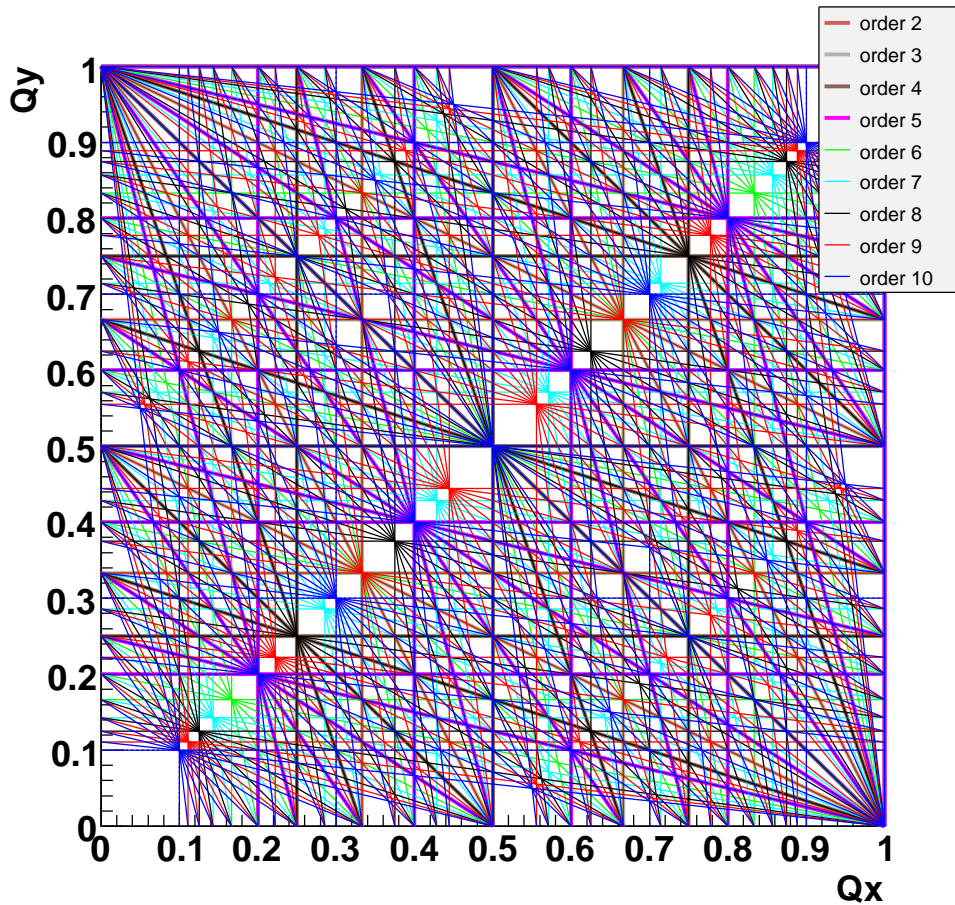
Figure B.12: Fractional machine resonances up to the 10th order.

strength could be calculated in terms of a bending power $(B \cdot dL)$. A measurement of the coupling strength in terms of the minimal tune difference as a function of the current in the compensating solenoids has been performed (see figure B.17). This measurement has the result, that the coupling can't be generated by the electron-cooler solenoid alone. After this measurement the coupling was reduced by tuning the sextupole magnets of the ring (see also figure B.14).

B.5 Target Density and Beam Lifetime

To check up to which target density the electron cooler could compensate the multiple Coulomb scattering, the lifetime was measured with different gases and different target densities. As the time dependence of the beam current is purely exponential the lifetimes
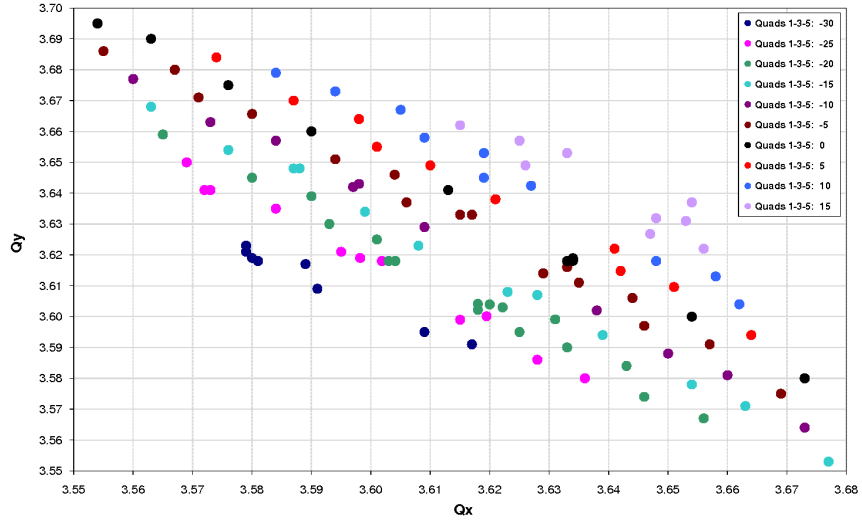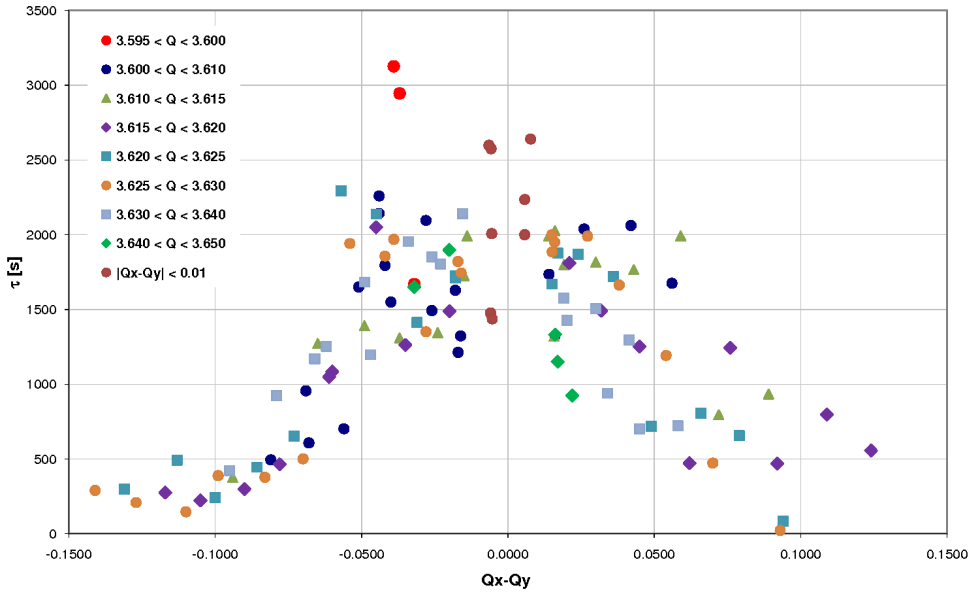
Figure B.13: Tune occupancy plot.

Figure B.14: Beam lifetime as a function of tune difference. Each colour stands for a constant tune $Q = \sqrt{(Q_x^2 + Q_y^2)/2}$.

resulting from different effects τ_i lead to a total lifetime τ_{total} of:

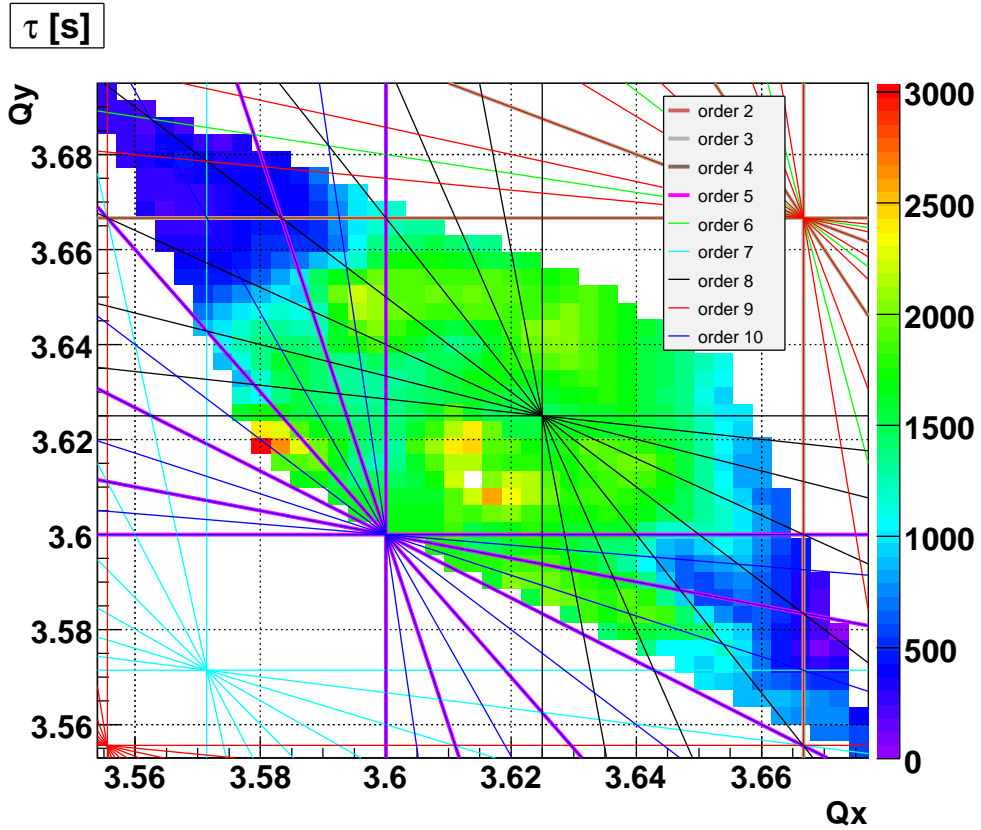$$\frac{1}{\tau_{total}} = \frac{1}{\tau_1} + \frac{1}{\tau_2} \ ,$$

Figure B.15: Beam lifetime as a function of the tune.

where τ_1 is the contribution from the target and τ_2 is the lifetime, which is due to the residual gas. In order to disentangle the two contributions, the measurement has been performed in two cycles: one with the target switched on and one with the target off.

Each cycle has been organised as follows:

- Injection: $0\,\mathrm{s}$

- Cooling on: $6\,\mathrm{s}$

- Target on: $26\,\mathrm{s}$, (later $66\,\mathrm{s}$)

- Target off: $1740\,\mathrm{s}$

- Cooling off: $1790\,\mathrm{s}$

For higher target densities, the target-on signal was shifted to a later time. This became necessary as we observed higher beam losses just after switching the target on, as shown in figure B.18. With the shifted target-on time these beam losses has not occurred anymore.
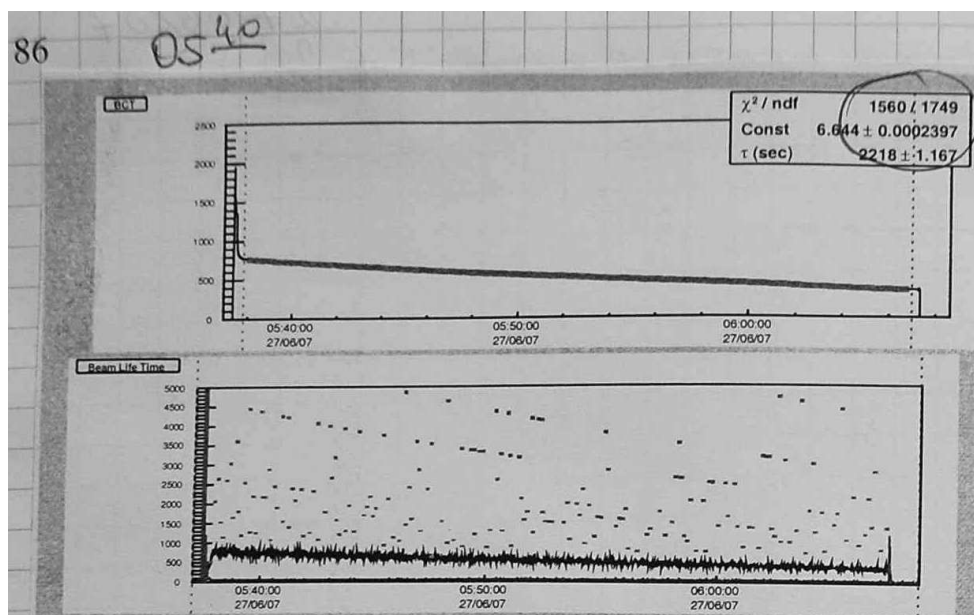
Figure B.16: Beam current with exponential fit in upper plot, $d(BCT)/dt$ and local beam lifetime in plot below.
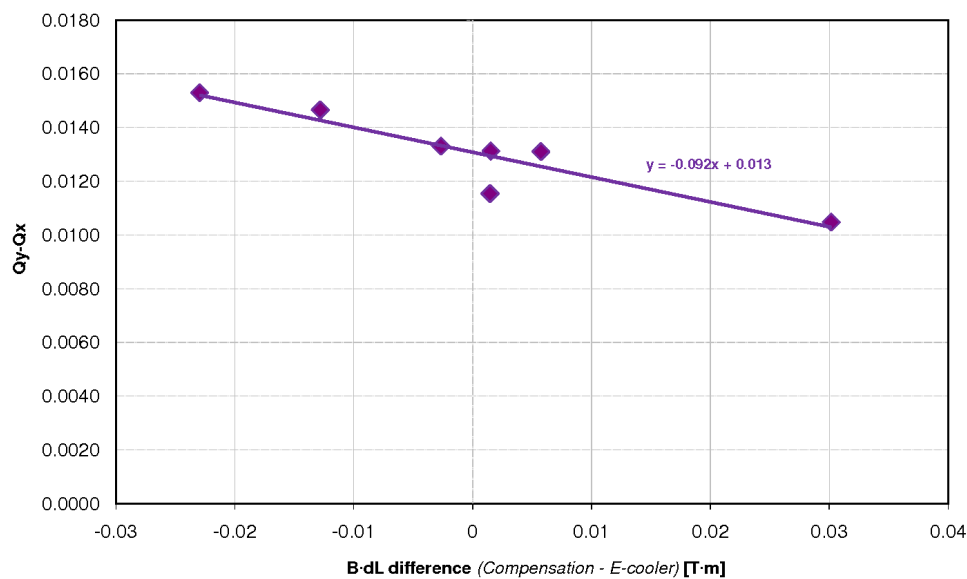

Figure B.17: Tune difference as a function of the magnetic field of the electron-cooler solenoid.

The only explanation for this effect would be that the beam needs more time to be cooled down.

For every gas several target densities have been measured. As the single Coulomb scat-
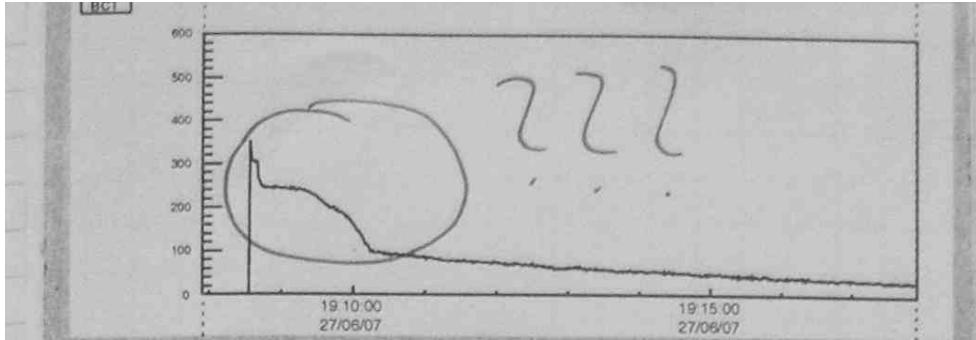
Figure B.18: Initial beam loss after switching the target on.

tering losses increase linearly with the target density ρ, the lifetime should be proportional to $\frac{1}{\rho}$.

For each target density the lifetime caused by the target effect was calculated using the lifetime from the cycle with target and one cycle without target nearby. This was done to minimise the effects coming from varying residual gas or other effects in the ring.

Deuterium

In the deuterium case the target dependence was measured during two nights. All results are shown in figure B.19. The plotted fit curve gives an exponent of -1.01, which is in a perfect agreement with the expected value of -1. The lifetime with the target density of $\approx 1.2 \cdot 10^{14} \frac{1}{\mathrm{cm}^{-2}}$ was only 150 s, which has to be improved by at least an order of magnitude.

Helium

As helium is pumped very badly (see figure B.20), it was not possible to measure the target density dependence with helium. The helium was moving around the ring and the lifetime without target was strongly varying from cycle to cycle.

Thus, the result is that there is no way to use helium as a target with the existing pumps. Only a decrease of the temperature for the cryo pumps from 10 K to 7 K (see figure B.21) or the replacement of cryo pumps with turbo pumps could give us a benefit.

Nitrogen

For nitrogen the lifetime dependence on the target thickness is in good agreement with the expected $\propto 1/\rho$ behaviour (see figure B.19). Like in the deuterium case, the reached lifetime with the target density of $\approx 1.0 \cdot 10^{13} \frac{1}{\mathrm{cm}^{-2}}$ was only 170 s. The ratio between the lifetime with deuterium and nitrogen should be 49:1, as nitrogen has $Z = 7$ and the lifetime goes with $1/Z^2$, although the observed ratio is roughly 20:1. There are several effects, which can cause this. First, for the two gases the gas inlet was calibrated separately. A small
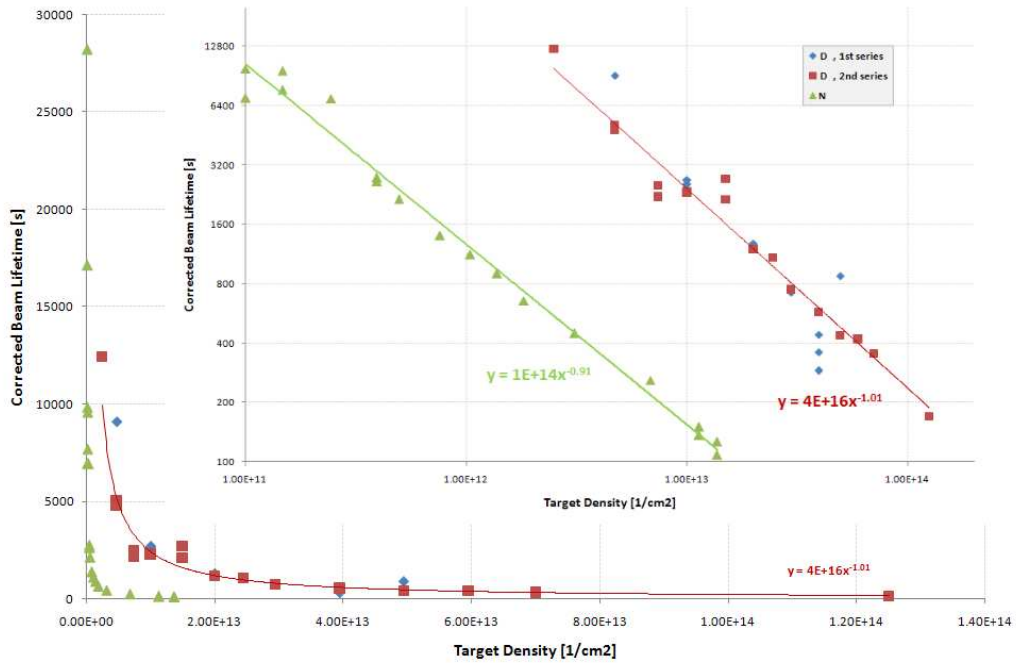
Figure B.19: Beam lifetime dependence of the target density and a fit curve with the exponent as a fit variable for deuterium and nitrogen targets. The densities given here are atomic ones.
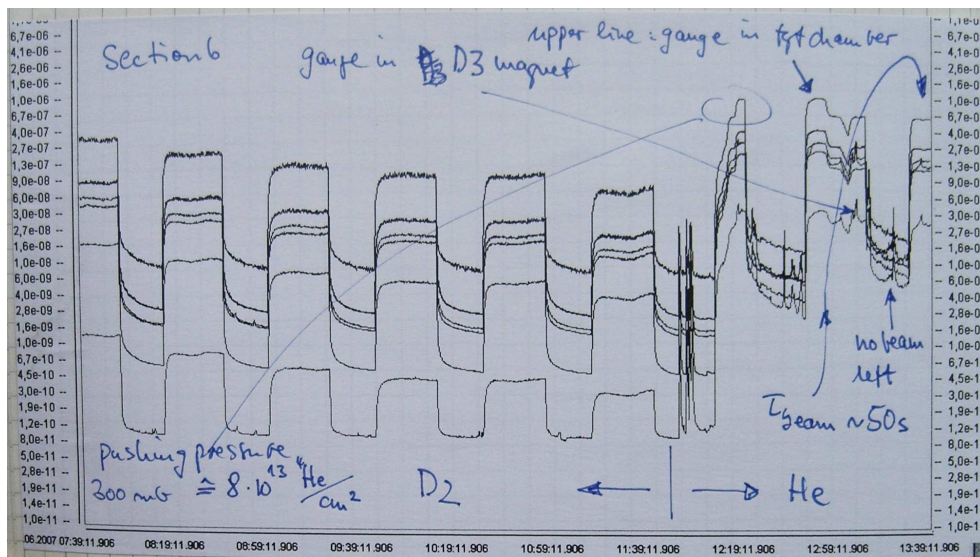

Figure B.20: Pressure in section 6 with and without a deuterium and helium target.
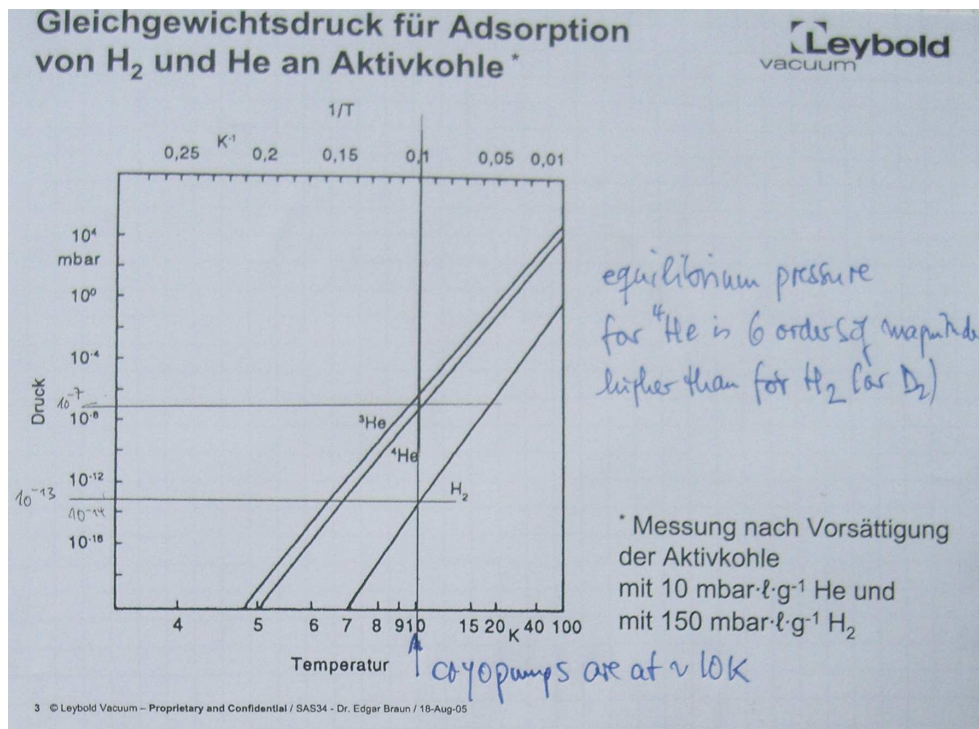
Figure B.21: Equilibrium pressure for absorption of H_2 and He with active coal.

uncertainty in this calibrations can easily lead to a big change in the ratio. On the other hand it is possible, that the residual gas is different in the cycle with and without target. This would lead to a wrongly corrected lifetime resulting in a change of the ratio.

B.5.1   Beam Lifetime and Beam Intensity

At COSY we have a possibility to use stack injection in order to increase the beam intensity and micro pulsing to have less intensity.

By using the micro pulsing the beam intensity has been adjusted between $4 \cdot 10^8 \frac{1}{\text{cm}^2}$ and $1.4 \cdot 10^9 \frac{1}{\text{cm}^2}$. For all the different targets the measured lifetime exhibits no dependence on the beam intensity (see figure B.22).

B.5.2   Conclusions and Outlook

1. In current situation the use of ^{4}He as a target is not possible unless pumping capabilities are improved.

2. With the electron cooling the beam exhibits purely exponential behaviour, thus being caused by the single Coulomb losses only.
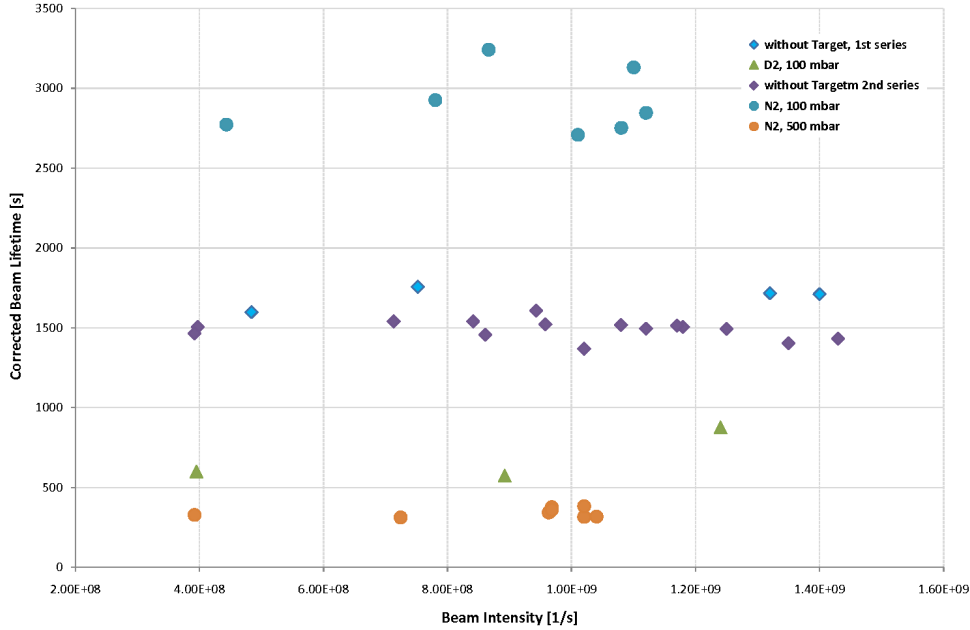
Figure B.22: Beam lifetime dependence on the beam intensity for different gases and target densities .

3. Flat orbit is required. For a careful adjustment it is however necessary to calibrate the BPMs.

4. A machine acceptance of $20\,\pi\,\mathrm{mm}\,\mathrm{mrad}$ has been measured both with and without cell. The cell is not the limiting aperture in the machine and a better close orbit setting is necessary to improve the machine acceptance.

5. In spite of the fact that higher beam lifetimes are expected in the region where horizontal and vertical tunes are equal, there is an area quite far from $Q_x = Q_y$ line where highest lifetime is observed. This region has to be studied once again in detail. Furthermore, the tune dependence of the beam lifetime in close to the tune equality line displays structures, which at the moment are not understood.

6. The beam lifetime is generally independent on the beam current, although the situation at high intensities of the order of 10^{10} particles per spill has not been checked yet.

7. The beam lifetime of only $250\,\mathrm{s}$ is observed for a deuterium target of $10^{14}\,\mathrm{cm}^{-2}$, which is much lower than the predicted value. Such lifetime makes proposed depolarisation studies almost impossible. Therefore, further machine development is necessary.

8. The beam lifetime at high beam currents has to be investigated. This requires electron cooler to be set-up at two different energies, as it is needed both for stacking

and at the flat top[10].

---

[10]This is possible according to Dieter Prasuhn.

Appendix C

COSY Timing Table

Trigger	Oberflaeche	Zeit/ms	Aktion	aktiv	Experimente
tuned	HV-ecool	1000	Soll_100_KV-Netzgeraet	ja	1 2 3 4 5 6 7 8
cooling	HV-ecool	1500	Datensatz_1	ja	1 2 3 4 5 6 7 8
detuned _02	HV-ecool	15000	SW-Soll_100_KV-Netzgeraet	ja	3
aus_02	HV-ecool	15500	Datensatz_2	ja	2
retuned_02	HV-ecool	20000	Soll_100_KV-Netzgeraet	ja	3
an_02	HV-ecool	20500	Datensatz_1	ja	2
detuned_03	HV-ecool	25000	SW-Soll_100_KV-Netzgeraet	ja	3
aus_03	HV-ecool	25500	Datensatz_2	ja	2
retuned_03	HV-ecool	30000	Soll_100_KV-Netzgeraet	ja	3
an_03	HV-ecool	30500	Datensatz_1	ja	2
⋮	⋮	⋮	⋮	⋮	⋮
detuned_48	HV-ecool	475000	SW-Soll_100_KV-Netzgeraet	ja	3
aus_48	HV-ecool	475500	Datensatz_2	ja	2
retuned_48	HV-ecool	480000	Soll_100_KV-Netzgeraet	ja	3
an_48	HV-ecool	480500	Datensatz_1	ja	2
detuned_49	HV-ecool	485000	SW-Soll_100_KV-Netzgeraet	ja	3
aus_49	HV-ecool	485500	Datensatz_2	ja	2
retuned_49	HV-ecool	490000	Soll_100_KV-Netzgeraet	ja	3
an_49	HV-ecool	490500	Datensatz_1	ja	2
detuned_50	HV-ecool	495000	SW-Soll_100_KV-Netzgeraet	ja	3
aus_50	HV-ecool	495500	Datensatz_2	ja	2
retuned_50	HV-ecool	500000	Soll_100_KV-Netzgeraet	ja	3
an_50	HV-ecool	500500	Datensatz_1	ja	2
cooling_aus	HV-ecool	1058000	Datensatz_2	ja	2 3

Table C.1: This table shows the used software timings for the "O"-Cycle (2) and "E"-Cycle (3). The numbering of the triggers starts with 2, as the first iteration was skipped in order to start with a well-cooled beam.

Bibliography

[Age07] E.S. Ageev et al. (COMPASS Collaboration), Nucl. Phys. **B765**, 31 (2007).

[Air05] A. Airapetian et al. [HERMES Coll.], Phys. Rev. Lett. **94**, 012002 (2005).

[Akh74] A.I. Akhiezer and M.P. Rekalo, Sov. J. Part. Nucl **3**, 277 (1974);

[ANK] S. Barsov et. al., Nucl. Instr. Meth **A462**, 364 (2001).

[Ans07] M. Anselmino et al., Phys. Rev. **D75**, 054032 (2007).

[Are07] H. Arenhövel, *Coulomb effects in polarization transfer in elastic antiproton and proton electron scattering at low energies*, Eur. Phys. J. **A34**, 303 (2007).

[Are09] Arenhoevel et al.,*Erratum, Coulomb effects in polarization transfer in elastic antiproton and proton electron scattering at low energies*, Eur. Phys. J. **A39**, 133 (2009). R. Arnold, C. Carlson and F. Gross, Phys. Rev. **C23**, 363 (1981).

[Art90] X. Artru, M. Mekhfi, Z. Phys. C **45**, 669 (1990).

[BaBar284] G.Batignani et. al. "Geometrical Specifications of the Silicon Detectors Barrel Detectors", BaBar Not #**284**, March 29, 1996.

[BaBar312] G.Batignani et. al. "Specifications and Quality Control Procedures of Silicon Detectors for SVT", BaBar Not #**312**, July 12, 1996.

[Bar07] *Proc. Workshop on Polarized Antiproton Beams = How? Daresbury, UK, 2007*, AIP Conf. Proc. **1008** (2008).

[Bir97] V.M. Biryukov, Yu.A. Chesnokov, and V.I. Kotov, Criystal Channeling and its Application at High Energy Accelerators (Springer, Berlin, 1997).

[Bjo69a] J.D. Bjørken, "Asymptotic sum rules at infinite momentum", Phys. Rev. **169**, 1547 (1969)

[Bjo69b] J.D. Bjørken and E.A. Paschos, "Inelastic electron-proton and γ-proton scattering and the structure of the nucleon", Phys. Rev. **185**, 1975 (1969).

[Bod85] *Proc. Workshop on Polarized Antiprotons, Bodega Bay, CA, 1985*, AIP Conf. Proc. **145** (1986).

[Bou95] D. Boutigny et al. BaBar Technical Design Report. Technical report, SLAC-R-95-457 Report, March 1995.

[Boz00] C.Bozzi et al. The design and construction of the BaBar silicon vertex tracker. Nucl. Instr. and Meth. in Phys. Res., **A447**:15-15, 2000.

[Boz01] C.Bozzi et al. The BaBar Silicon Vertex Tracker. Nucl. Instr. and Meth. in Phys. Res., **A461**:162-167,2001.

[Bys78] J. Bystricky, F. Lehar, P. Winternitz, J. Phys. (Paris) 39 (1978) 1.

[Cal69] C.G. Callan and D.J. Gross, Phys. Rev. Lett. **33**, 156 (1969).

[CER] Ceramasil Ltd.

[Col93] J.C. Collins, Nucl. Phys. **B396**, 161 (1993).

[Cor92] J.L. Cortes, B. Pire, J.P. Ralston, Z. Phys. C **55**, 409 (1992).

[COS] R. Maier, Nucl. Instr. Meth. **A 390**, 1 (1997) .

[Cso68] P.L. Csonka, Nucl. Instrum. Methods **63**, 247 (1968).

[Die] M. Diefenthaler [HERMES Coll.], arXiv:0706.2242 [hep-ex].

[Die01] S. Dieterich et al., Phys. Rev. Lett. **84**, 1398 (2000).

[Die04] J. Dietrich et al., *Characteristic Features of Electron Cooling at COSY*, Annual Report IKP-FZ Jülich p77 (2004), available from http://www.fz-juelich.de/ikp/publications/AR2004/en/contents.shtml.

[Dür92] M. Düren et al., Nucl. Instrum. Methods Phys. Res., Sect. **A322**, 13 (1992).

[Dur95] *The HERMES Experiment: From the Design to the First Results*, DESY HERMES-95-02 (1995).

[Fey69] R. Feynman, "Very high-energy collisions of hadrons", Phys. Rev. Lett. **23**, 1415 (1969).

[Gab08] G. Gabrielse et al., Phys. Rev. Lett. **100**, 113001 (2008).

[Gay01] O. Gayou et al., [Jefferson Lab Hall A Collaboration], Phys. Rev. **C64**, 038202 (2001).

[Gay02] O. Gayou et al., [Jefferson Lab Hall A Collaboration], Phys. Rev. Lett. **88**, 092301 (2002).

[Gel64] M. Gell-Mann, "A schematic model of baryons and mesons"; Phys. Lett. **8**, 214 (1964).

[Gem74] D.S. Gemmell, Rev. Mod. Phys. **46**, 129 (1974).

[Hae67] W. Haeberli Ann. Rev. Nucl. Sci. **17**, 373 (1967).

[Hae85] W. Haeberli, in Nuclear Physics with Stored, Cooled Beams, edited by P. Schwandt and H.O. Meyer, AIP Conference Proceedings No. 128, 251 (1985).

[Her08] WE-Heraeus-Seminar, *Polarized Antiprotons*, June 2008, http://www.fe.infn.it/heraeus/.

[Jac76] J.D. Jackson Rev. Mod. Phys. **48**, 3 (1976).

[Jaf92] R.L. Jaffe, X. Ji, Nucl. Phys. B **375**, 527 (1990).

[Jon00] M.K. Jones et al., [Jefferson Lab Hall A Collaboration], Phys. Rev. Lett. **84**, 1398 (2000).

[Kin77] N.S.P. King et. al., Phys. Lett **69B**, 2 (1977).

[Kra89] D. Krämer et al., Nucl. Instrum. Methods Phys. Res., Sect. **A287**, 268 (1989).

[Lee04] S. Y. Lee, *Accelerator Physics - Second Edition*, World Scientific (2004) p426.

[Lin64] J. Lindhard, Phys. Lett. **12**, 126 (1964).

[Lin65] J. Lindhard, Kgl. Danske Videnskab. Selskab, Mat. Fys. Medd. 34 (1965).

[Mar99] O. Martin et. al, Phys. Rev D**60**, 117502 (1999).

[Mer07] T. Mersmann, "Untersuchung der Wechselwirkung zwischen η-Mesonen und ^3He-Kernen am Experimentaufbau ANKE", Doktorarbeit, Institut für Kernphysik, Westfälische Wilhelms-Universität Münster, 2007.

[Mey94] H.O. Meyer, Phys. Rev. **E50**, 1485 (1994).

[MIC] Micron Semiconductro Ltd. http://www.micronsemiconductor.co.uk.

[Mil05] A.I. Milstein and V.M. Strakhovenko, Phys. Rev. **E72**, 066503 (2005).

[Mil08] A.I. Milstein, S.G. Salnikov and V.M. Strakhovenko, Nucl. Instr. Meth. **B266**, 3453 (2008).

[Mil98] B. Milbrath et al., Phys. Rev. Lett. **80**, 452(1998), **82**, 2221 (E) (1990).

[Mur74] J.J. Murphi et al., Phys. Rev. C **9**, 2125 (1974).

[Mus07] A.Mussgiller, Identification and Tracking of low Energy Spectator Protons, PHD-thesis.

[Nas05] A.Nass et. al., Nucl. Instr. Meth. **A505**, 633 (2003).

[Oel06] D. Oellers for the ANKE and PAX Collaborations, *Do unpolarized electrons affect the polarization of a stored proton beam?*, Proposal to COSY, Jülich 2006, available from the PAX-webpage http://www.fz-juelich.de/ikp/pax.

[Oel07] D. Oellers for the ANKE and PAX Collaborations,*Do unpolarized electrons affect the polarization of a stored proton beam?*, Beam Request to COSY, Jülich 2007, available from the PAX-webpage http://www.fz-juelich.de/ikp/pax.

[Oel09] D. Oellers et al., *Polarizing a stored proton beam by spin flip?*, Phys. Lett. **B 674**, 269 (2009).

[PAX05] P.Lenisa, F. Rathmann (PAX Collaboration), arXiv:hep-ex/0505054v1 (2005).

[PAX09] arXiv:0904.2325 ; CERN-SPSC-2009-012 ; SPSC-P-337.

[pdg08] C. Amsler at. al, Phys. Lett. **B667**, 1 (2008).

[PEP] PEP II - Conceptual Design Report. Technical report, Report SLAC-418, June 1993.

[Pot90] H. Poth, Phys. Rep. **196**, 135 (1990).

[Rat05] F. Rathmann, Summary of the *Worksho pn Spin Filtering in Storage Rings* (8th PAX Meeting), Heimbach, Germay September 2005; available from the PAX website at http://www.fz-juelich.de/ikp/pax.

[RAT93] F. Rathmann et al., PRL 71, 1379 (1993).

[Rat94] F. Rathmann, Ph.D. thesis, Phillips-Universit´at Marburg, January 1994.

[Ros50] M.N. Rosenbluth, Phys. Rev. **79**, 615 (1950).

[Ruth19] E. Rutherford, Phil Mag **ser6, xxxiv** 537-561, 562-571, 571-580, 581-587 (1919).

[Sei] R. Seidl et al [BELLE Coll.], arXiv:0805.2975 [hep-ex].

[Sei06] R. Seidl et al [BELLE Coll.], Phys. Rev. Lett. **96**, 232002 (2006).

[Ste] J. Stein, FZ Jülich, private communication.

[Ste03] E. Steffens and W. Haeberli, Rep. Prog. Phys **66**, 1887 (2003).

[Ukh08] M. Ukhanov, Polarized Antiproton Beams - How?, An International Workshop, Warrington, UK, 2007, AIP Proceedings 1008 (2008).

[Wal07] Th. Walcher et al., *A surprising method for polarising antiprotons*, Eur. Phys. J. **A34**, 447 (2007).

[Wal09] Th. Walcher et al., *Erratum, A surprising method for polarising antiprotons*, Eur. Phys. J. bf A39, 137 (2009).

[Wiki] http://en.wikipedia.org/wiki/Drell-Yan (2010).

[Zel85] A.N. Zelenski et. al., Nucl. Instr. Meth. **A245**, 223 (1986).

[Zwe64] G. Zweig, "An SU(3) model for strong interaction symmetry and its breaking"; CERN preprints **TH-401**, **TH-412**, (1964).

Acknowledgments

Lebenslauf

Schulische Laufbahn:

- geboren am 14.06.1978 in Jülich

- 08/1984 bis 06/1988 Besuch der Gemeinschaftsgrundschule Nord, Jülich

- 08/1998 bis 05/1998 Besuch des stdtischen Gymnasiums Zitadelle, Jülich

- 07/1998 bis 07/1999 Zivildienst im "Haus zum Guten Hirten", Münster

- 10/1999 bis 01/2005 Physik-Studium an der RWTH

- 02/2005 bis 04/2005 Wissenschaftliche Hilfskraft am Physikalischen Institut IB an der RWTH Aachen

- seit 01. 05. 2005 Promotion am Institut fr Kernphysik, am Forschungszentrum Jülich GmbH, "Polarizing a Stored Proton Beam by Spin Flip?"

Eine Auswahl weiterer Tätigkeiten/Angagements:

- 1989 bis 1998 Mitglied der DPSG Jülich (Pfadfinder)

- 10/1999 bis 01/2005 diverse HiWi Stellen an der RWTH

- 04/2000 bis 03/2001 Vorstandsarbeit im ASV (akademischer Seglerverein der RWTH in Aachen)

- 10/2001 bis 09/2002 Vorstandsarbeit in der Arbeitsgemeinschaft "Internet AG" des Studendenwohnheims "KaWo1" des Studentenwerks Aachen AöR.

Erklärung

Ich versichere, daß die von mir vorgelegte Dissertation selbständig angefertigt, die benutzten Quellen und Hilfsmittel vollständig angegeben und die Arbeit - einschließlich Tabellen, Karten und Abbildungen -, die anderen Werken im Wortlaut oder dem Sinn nach entnommen sind, in jedem Einzelfall als Entlehnung kenntlich gemacht habe; daß diese Dissertation noch keiner anderen Fakultät oder Universität zur Prüfung vorgelegen hat; daß sie - abgesehen von unten angegebenen Teilpublikationen - noch nicht veröffentlicht worden ist sowie, daß ich eine selche Veröffentlichung vor Abschluß des Promotionsverfahrens nicht vornehmen werde.

Die Bestimmungen dieser Promotionsordnung sind mir bekannt. Die von mir vorgelegte Dissertation ist von Herrn Prof. Dr. H. Ströher betreut worden.

Veröffentlichungen

- D. Oellers et *al.*, Polarizing a stored proton beam by spin flip?, Phys. Lett. **B 674** (2009) 269-275.